

**TOPOLOGY OPTIMIZATION APPLIED TO DESIGN
OF SOLID OXIDE FUEL CELLS**

By

Xiankai Song

A DISSERTATION

Submitted to
Michigan State University
in partial fulfillment of the requirements
for the degree of

Mechanical Engineering--Doctor of Philosophy

2014

ABSTRACT

TOPOLOGY OPTIMIZATION APPLIED TO DESIGN OF SOLID OXIDE FUEL CELLS

By

Xiankai Song

A topology optimization method is used to identify optimal designs of the cathode microstructure and the anode support in a solid oxide fuel cell (SOFC). Two dimensional and three dimensional models are considered. A 2D topology optimization model is developed to minimize the cathode resistance. A simplified analysis model is used in computations. Results highlight the importance of the cathode geometry in the performance. Optimal geometric features are found to depend on the material properties and various geometric parameters.

To improve upon the accuracy available from a purely 2D model, a 3D finite element model is established to make an accurate prediction of the cathode resistance. A detailed 3D microstructure is reconstructed from images obtained using the 3D focused ion beam-scanning electron microscopy. A 3D topology optimization formulation is set up to minimize cathode resistance. The effect of the material properties on the geometric features is investigated. Improvements up to 35% are achieved by properly organizing the cathode microstructure.

The thermal stress problem of the anode support in the SOFC stacks is also of great interest. Fuel flow, heat transfer, thermo-mechanical and electrochemical processes are considered in a coupled model. A Weibull distribution evaluating the probability of failure is used as a measure of the strength of the anode. A new material model is developed aiming at the topology optimization of the anode strength. Optimal designs for two types of objective functions, including minimum thermal compliance and minimum probability of failure, are obtained. It is observed that the designs obtained using the two objective functions can improve the performance for 10%.

ACKNOWLEDGMENTS

I have been supported and encouraged by many colleagues and friends throughout my PhD time at Michigan State University. I would like to acknowledge those who granted their precious help to me.

Foremost, I would like to express my deepest gratitude to my academic advisor, Prof. Alejandro R. Diaz. He has taught me everything I need in research, and make me well prepared for my future work. He has provided me the best research environment I have ever had. He has taken me around the world to meet the professionals in the optimization groups. He has also been an exceptional friend and a great mentor.

During my three years' PhD work, I had the honor to work with Prof. Andre Benard, who has kept me ecstatic with his numerous insightful and creative suggestions. I am very appreciative of Prof. Jason Dale Nicholas for the shared knowledge of solid oxide fuel cells and enthusiasm towards our collaborative work. Extended thanks to my fellow students, Dr. Kazuko Fuchi, Mark Daniel Gaustad, Joonho Lee, Tingli Cai, Smruti Panigrahi and Chao Cheng for their continuous encouragement and invaluable friendship. Special thanks to Prof. Ronald Averill, who agreed to serve on my Ph.D. committee.

Finally, I am grateful to my mother, Prof. Naiwen Ye, for always standing by my side, understanding me and motivating me towards a meaningful life.

TABLE OF CONTENTS

LIST OF TABLES.....	vi
LIST OF FIGURES	vii
KEY TO SYMBOLS OR ABBREVIATIONS.....	ix
Chapter 1 Introduction.....	1
Chapter 2 A 2D model for shape optimization of solid oxide fuel cell cathodes.....	7
2.1 Simplified analysis model of infiltrated composite cathode.....	7
2.2 The simple model as a periodic single column reference design.....	9
2.3 Finite element model for 2D topology optimization problem	11
2.4 Objective function.....	15
2.5 Constraints	15
2.6 The optimization problem.....	16
2.7 Filters	17
2.8 Techniques to reject inadmissible designs	17
2.9 Sensitivity Analysis.....	20
2.10 Examples.....	21
2.10.1 Designs with different material properties.....	22
2.10.2 Design with varying footprint B and constant perimeter/footprint ratio	24
2.10.3 Design with varying perimeter P and amount of material W while keeping the footprint constant	25
2.10.4 Design with varying amount of material	25
2.11 Conclusions.....	26
Chapter 3 A 3D finite element model for cathode microstructure of solid oxide fuel cell cathodes.....	28
3.1 Analysis model of infiltrated composite cathode.....	28
3.2 Finite element formulation of 3D cathode microstructure.....	31
3.3 Generation of 3D microstructure mesh from experimental data	33
3.4 Examples of the simulation of the 3D cathode resistance	38
3.5 Experimental validation and comparison with a simple estimation model	40
3.6 Other examples	43
3.7 Conclusions.....	45
Chapter 4 Topology optimization for 3D cathode microstructure of solid oxide fuel cell cathodes.....	46
4.1 Problem Setup.....	46
4.2 Material model.....	48
4.3 Constraints	52
4.4 Optimization Problem.....	53
4.5 Sensitivity Analysis.....	53
4.6 Numerical Examples.....	55

4.6.1 Designs with varying the material properties by changing work temperature	57
4.6.2 Design with varying the arrangement of the cathode roots with constant footprint.....	63
4.7 Conclusions.....	66
Chapter 5 Thermal strength design for anode support structure of solid oxide fuel cell electrode	68
5.1 Analysis model.....	69
5.1.1 The fuel flow model.....	72
5.1.2 The electrochemical reaction boundary condition	73
5.1.3 The hydrogen/heat transport model	76
5.1.4 The thermal structural model	77
5.2 Material model.....	79
5.3 Finite element model.....	83
5.4 Objective functions	84
5.5 Constraints	84
5.6 Optimization problems.....	85
5.7 Sensitivity analysis.....	87
5.8 Examples.....	89
5.8.1 Minimum the thermal compliance	90
5.8.2 Minimum the probability of failure	91
5.9 Conclusions.....	93
Chapter 6 Conclusions.....	95
BIBLIOGRAPHY	98

LIST OF TABLES

Table 2.1 Performance of optimized designs for different materials, where R can be multiplied by l/σ_0 to recover units (Fig. 2.6)	23
Table 2.2 Performance of optimized designs for different footprints B and $P_B/B = 9$, where R can be multiplied by l/σ_0 to recover units (Fig. 2.7)	24
Table 2.3 Performance of optimized designs for different values of the perimeter bound P_R , where R can be multiplied by l/σ_0 to recover units (Fig. 2.9)	25
Table 2.4 Performance of optimized designs for different values of the amount of material bound W_R , where R can be multiplied by l/σ_0 to recover units (Fig. 2.9)	26
Table 3.1 Bulk conductivity of CGO ($G_{d0.1}C_{e0.9}O_2$)	39
Table 3.2 Scaled ASR values for 20 nm MIEC LSCF ($L_{a0.6}S_{r0.4}C_{o0.8}F_{e0.2}O_3$) particle diameter.....	39
Table 3.3 Diffusivity and concentration of oxygen gas in air at 1atm [57]	40
Table 4.1 Performance of optimized design at different temperatures (Fig. 4.7-4.8).....	58
Table 4.2 Tortuosity and surface areas of optimized design at different temperatures (Fig. 4.7)	62
Table 4.3 Performance of optimized design for different root arrangements (Fig. 4.9-4.10).....	66
Table 4.4 Improvement of optimized design for different root arrangements compared to experimental data (Fig. 4.9-4.10).....	66
Table 5.1 The performance of the anode support design for the thermal compliance design	91
Table 5.2 The performance of the anode support design for the probability of failure design	92

LIST OF FIGURES

Figure 1.1 Schematic arrangement of a SOFC	1
Figure 2.1 Geometry of the reference design used for comparison	10
Figure 2.2 A periodic computational domain is used in the cathode model as shown in a but it is extended as in b to allow the exploration of the entire space through topology optimization	12
Figure 2.3 Sketch of periodic cell	14
Figure 2.4 Detecting neck regions that may trap internal holes	18
Figure 2.5 Cathode model may predict that (b) is worse than either (a) or (c).....	19
Figure 2.6 Optimized designs for different values of h_0/σ_0 . As h_0/σ_0 increases, the perimeter becomes less important and the shape of the scaffold begins to dominate. Performances reported in Table 2.1	23
Figure 2.7 Optimized designs for different footprints B and $P_B/B = 9$. For a large footprint, the cathode shape becomes more convoluted and departs further from a columnar shape, not being confined by the design space. Performances reported in Table 2.2.....	24
Figure 2.8 Optimized designs for different values of the perimeter bound P_R . As expected, a large perimeter corresponds to a greater performance improvement. Performances reported in Table 2.3	25
Figure 2.9 Optimized designs for different values of the amount of material bound W_R . Performances reported in Table 2.4	26
Figure 3.1 The sketch of a 3D cathode microstructure	29
Figure 3.2 The manufacture process of a SOFC composite cathode sample [14]	33
Figure 3.3 The reconstruction process using 3D Focused Ion Beam-Scanning Electron Microscopy.....	35
Figure 3.4 An example of a black-white image of a 9 μ m thick scaffold.....	36
Figure 3.5 The 3D mesh of the 9 micron thick cathode microstructure	38
Figure 3.6 The comparison of R_P data for 20nm LSCF particles.....	41
Figure 3.7 The comparison of R_P data for 20nm LSCF particles with a small oxygen gas	

diffusivity.....	42
Figure 3.8 The comparison of R_p data for 20nm LSCF particles with a very large oxygen gas diffusivity.....	43
Figure 3.9 The comparison of R_p data obtained from different methods for 20nm LSCF particles.....	44
Figure 4.1 The design domain of the 3D microstructure problem.....	48
Figure 4.2 The arrangement of the element face number.....	50
Figure 4.3 Penalty in the surface resistance model may make design (b) performs worse than (a) and (c).....	50
Figure 4.4 The second derivative can determine the trend of the first derivative.....	52
Figure 4.5 The arrangements of the fixed roots.....	56
Figure 4.6 The comparison between the analysis domain in Chapter 3 and the design domain in Chapter 4 (in white rectangle).....	57
Figure 4.7 The optimized design at different work temperatures. Performance is reported in Table 5.1.....	59
Figure 4.8 The comparison of R_p data for 20nm LSCF particles with a small oxygen gas diffusivity.....	61
Figure 4.9 The optimized design for different root arrangements at 400 °C. Performance is reported in Table 4.3.....	64
Figure 4.10 The optimized design for different root arrangements at 700 °C. Performance is reported in Table 4.3.....	65
Figure 5.1 The cross section of the fuel supply channel and the electrode.....	70
Figure 5.2 The analysis domain (a) and design domain (b) for the anode support.....	71
Figure 5.3 The $i-pH_2$ curve and the $i-T$ curve.....	75
Figure 5.4 The material models for thermo-mechanical problem.....	82
Figure 5.5 The reference flat design with a constant thickness of 600 μ m, the black pixels represent the anode support; the white pixels represent the fuel flow path.....	90
Figure 5.6 The optimal cross section in example 5.8.1 for the minimum probability problem ...	90
Figure 5.7 The optimal cross section in example 5.8.2 for the minimum probability problem ...	92

KEY TO SYMBOLS OR ABBREVIATIONS

SOFC Solid Oxide Fuel Cell

FIB-SEM Focused Ion Beam-Scanning Electron Microscopy

MIEC Mixed Ionic Electronic Conducting

J_i atomic flux (A/cm^2)

ϕ electrical potential (V)

F Faraday's constant (C/mol)

σ_0 ionic conductivity (S/cm)

R_S cathode surface resistance (Ωcm^2)

h_0 interface reaction coefficient (S/cm^2)

Φ_∞ driving potential (V)

R_P cathode resistance (Ωcm^2)

f total current flow (A)

l non-dimensional element size

P non-dimensional perimeter

W non-dimensional amount of material

B non-dimensional unit cell footprint

σ_g diffusivity of oxygen gas (m^2/sec)

i interface current generation (A/cm^2)

Q interface oxygen gas consumption ($\text{mol}/(\text{sec}\cdot\text{cm}^2)$)

h_c oxygen exchange coefficient ($\text{S}\cdot\text{cm}/\text{mol}$)

z charge number of oxygen ion

n_0 Avogadro constant (mol^{-1})

μ viscosity of hydrogen gas (m^2/sec)

u Flow velocity (m/sec)

p pressure (Pa)

ρ_{Fuel} density of fuel (kg/m^3)

V^{cc} close circuit potential (V)

V^{oc} open circuit potential (V)

η^{act} activation potential (V)

R universal gas constant ($\text{J}/(\text{mol}\cdot\text{K})$)

T temperatrue (K, °C)

c_{H_2} concentration of hydrogen gas (mol/m^3)

σ_{H_2} diffusivity of hydrogen gas (m^2/sec)

c_{Heat} the specific heat ($\text{J}/(\text{kg}\cdot\text{K})$)

σ_{Heat} heat conductivity (m^2/sec)

h_{air} convection coefficient for air flow (m/sec)

P_f probability of failure

E_0 Young's modulus (Pa)

x displacement (m)

ε strain

σ stress (Pa)

α_t coefficient of thermal expansion (K^{-1})

σ_S Weibull's characteristic strength (Pa)

m Weibull's modulus

C_T thermal compliance (J)

C_S static compliance (J)

I total current generation (A)

Q_F total fuel flow rate (m^3/sec)

Chapter 1 Introduction

A solid oxide fuel cell (SOFC) is an electro-chemical device that converts chemical energy into electric energy and heat directly, without the process of combustion [1][2]. Like other electrochemical devices, SOFCs, illustrated schematically in Fig. 1.1, output electrical power by generating electricity as electrons flow through an external circuit and linking spatially-separated redox reactions. Compared to other types of fuel cells, a distinguishing feature of SOFCs is the use of a solid electrolyte that conducts the oxygen ions from cathode to anode for the completion of the reactions occurring at the electrodes, which permits more flexibility in fuel cell designs [2]. The efficiency of SOFC can be as high as 60%-90% [3]. These advantages make SOFC a focus in recent fuel cell research.

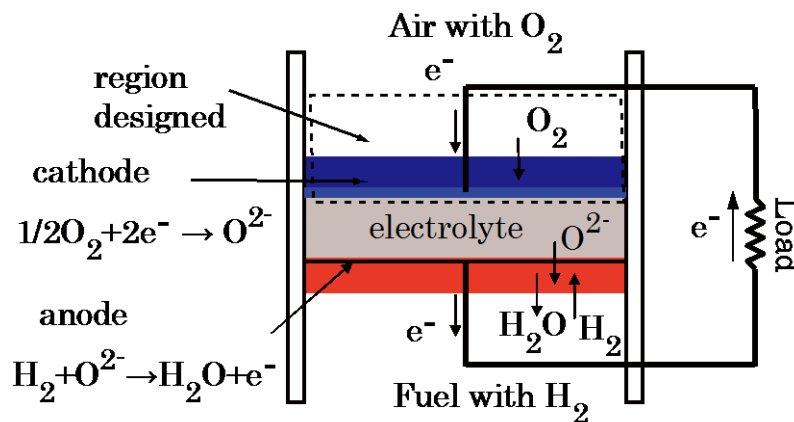


Figure 1.1 Schematic arrangement of a SOFC

For interpretation of the references to color in this and all other figures, the reader is referred to the electronic version of this dissertation.

In a SOFC, there are voltage losses associated with ohmic resistances in the electrodes and active

polarizations on the air-cathode interface and the fuel-anode interface. However, the voltage losses in a cathode usually dominate the entire stack so it is more efficient to focus on improving the cathode performance [3]. Often, this is accomplished by designing better composite cathodes. In one approach, conducting electrocatalyst nano-particles of a mixed ionic electronic conducting (MIEC) material are deposited into a porous ionic-conducting scaffold to form a composite cathode, and the composite cathode has received a lot of attention [4]-[8]. This is the arrangement for the cathode modeled in chapters 2-4, and the focus is on improving performance by optimizing the ionic conducting scaffold cathode microstructure.

Attempts in designing the cathode geometry from macro to micro scales have shown progress in reducing the cathode resistance. Chan et al.[9] performed a sensitivity analysis for a generic macro-homogeneous polarization model of a solid oxide fuel cell to study the effect of the thickness of the fuel cell components. The performance of composite cathodes as a function of various electrode microstructural parameters has also been the subject of investigation, as they typically show lower overpotential losses than single-phase electrodes [10]-[13]. Recently, detailed micromodeling of the performance of SOFCs was proposed and used to minimize the cathode total resistance [14][15]. In related work [16], the cathode-gas is modeled as a homogenized porous medium, and the author's goal is to optimize the shape of the interface between this medium and the electrolyte. Attempts were also made by Song et al. in [17]-[19] to improve the cathode performance by designing the micro and macro scale cathode structures.

As an electrochemical device that works at a high temperature (500~1000 °C), the thermo-mechanical behavior also plays a significant role in the performance of SOFC. The typical anode-supported electrode design is composed by a thick layer ($\approx 500\mu\text{m}$) of porous support on the anode side of the SOFC electrode and a thin active layer ($\approx 50\mu\text{m}$) of cathode,

electrolyte and anode are printed on the anode support [20]. The porous media used in SOFC electrodes exhibit a large spread of bulk failure strength due to the random nature of their inherent flaws from manufacturing [21]. The failure stress of these materials is not a well defined number, so the mechanical failure by the probability of failure [22], which was expressed by Weibull, is utilized to assess whether the material will fail at a given stress or not. The mechanical strength of the electrode is dominated by the performance of anode support, and it was investigated experimentally in [23]. Finite element analysis which considers both the electrochemical and thermo-mechanical processes in SOFC was also performed in [24]-[27]. Further works [28][29] evaluated the probability of failure using Weibull method, and concluded that the electrode has a high probability of failure when large tensile stress exists. The anode strength was also been optimized by imposing changes to production parameters, such as powder milling and sintering temperature [30].

Topology optimization is a design methodology that is able to find the optimal geometries of structures that achieve the design goals. It was first proposed by Bendsoe and Kikuchi in the context of structural design [31]. The geometries of structures are represented by an effective density of a material in each element in the finite element models, and the range of the effective density is extended from the binary values to a continuous domain. The material properties of each element are computed using a homogenization method and used in the constitutive equations. After progressing for more than two decades, the use of topology optimization has been extended to material design [32] with applications in different physics [33].

The formulation of the simulation model is of heat transfer type, and the application of topology optimization in heat transfer type problems is extremely interesting, especially when the problem involves design dependent boundaries. In such problems it is not possible to define material

boundaries a priori — they are the subject of the optimization — and therefore some boundary conditions cannot be set directly. Problems such as this have been discussed by various authors in the context of heat conduction. For instance, Yoon and Kim [34] proposed an “element connectivity parameterization” method to consider design-dependent effects for thermal boundary conditions. Bruns [35] investigated a 2D problem with convection both on the top and one the boundary of the structure. Iga et al.[36] introduced a smeared-out hat function to extract the side convection.

Due to the strong demand in industry, thermo-mechanical problems also attract many concerns. The earliest research in the area of topology optimization with thermal loads was by Rodrigues and Fernandes, who used a homogenization method to minimize the compliance of structures with combined temperature and mechanical loading [37]. Li et al. [38] applied the evolutionary structural optimization (ESO) method with element thicknesses as design variables. Using topology optimization method, Sigmund and Torquato generated structures with extreme thermal expansion properties [39], and Sigmund also developed thermal micro-actuators [40]. Cho and Choi [41] performed an adjoint design sensitivity analysis for topology optimization of weakly coupled thermo-elastic problem. In recent years, thermo-elastic topology optimization has been performed using to discuss the effect of the interpolation scheme in density-based methods for thermal loading [42]. For the thermo-strength design, Pedersen and Pedersen proposed an objective function based on uniform energy density instead of the structural compliance, and produced superior results focusing on strength design [43][44].

This dissertation focuses on two aspects of the performance of SOFC. Chapters 2-4 investigate the 2D and 3D finite element modeling and topology optimization method in micro-scale (nm~ μ m level) for the design of cathode microstructures. Chapters 5 establishes a structural-

fluid-thermal coupled finite element model for the macro-scale (mm level) geometry of SOFC fuel supply channel and anode supported electrode, and discusses the topology optimization of the thermo-mechanical performance. Short descriptions of the chapters are below.

In Chapter 2, the 2D finite element model with the consideration of the ohmic resistance in the ionic conducting scaffold and the activation polarization in the MIEC layer that surrounds the scaffold is established. The focus is on designing the shape of the scaffold and the MIEC layer to minimize the cathode resistance. Although the 2D designs are not able to be used as an example for the 3D scaffold microstructures, the 2D optimal results give a schematic direction to the cathode microstructure design by showing the effect of the material properties and geometric factors on characteristic scaffold feature sizes.

In Chapter 3, the 3D finite element model is set up in a similar manner to the 2D model in chapter 2, and the 3D model is validated by experimental data. A detailed 3D model of a cathode microstructure sample is reconstructed from a sequence of images recording the cross sections of the cathode microstructure. The cathode resistance is calculated by the 3D finite element model, and the results are compared with experimental measured cathode resistance. The good consistency between the simulation and experimental results at low temperature domain makes a solid basement for the following optimization work.

In Chapter 4, the topology optimization problem for the design of 3D cathode microstructures is discussed. A self-locked phenomenon caused by the use of penalized design dependent load is investigated, and this problem is solved by introducing a new material model that depends on both the first and second order spatial derivatives of the design variables. The cathode resistance of the optimal geometries is compared with the cathode resistances of the experimental sample to show the improvement. The 3D design is able to give direct and detailed guide to the cathode

microstructure design.

In Chapter 5, an integrated finite element model which simulates the fuel flow, hydrogen gas transport, conductive-convective heat transfer, electrochemical reactions and structural deformation of the macro-scale anode-supported SOFC electrode designs is set up, and a specific topology optimization model is set up for the improvement of thermo-mechanical strength. The SOFC performances such as the current generation, flow rate, static compliance, and thermo-mechanical deformation of the electrode are calculated. A failure model is set up based on the dependency of the thermo-mechanical performance on the porosity of the porous media, and the probability of mechanical failure is used to measure the structural strength. The probability of mechanical failure is minimized by altering the geometries of the fuel flow path, modifying the path of hydrogen gas transport and heat transfer in the electrode and adjusting the structure of the anode support. Although the 3D model can accommodate several design concepts, only the design for the cross section of the anode support structure is explored in this dissertation, focusing on the concepts that are easier to manufacture. The design that optimizes the probability of failure is compared with the thermo-mechanical compliance design.

Chapter 2 A 2D model for shape optimization of solid oxide fuel cell cathodes

An infiltrated composite cathode consists of an ionic conducting scaffold and a coating of MIEC applied on the surface of the scaffold. Finite element method has been used to analyze the performance of the cathodes. The use of finite element method also makes the efficiency compute of the sensitivity of the performance of the cathode with respect to the design, which is essential in topology optimization in chapter 2 and chapter 4.

A first attention at optimizing the cathode performance in this work seeks to improve the current generation/reduce the cathode resistance by designing the microstructure of the cathode scaffold using a 2D topology optimization model. A simplified finite element model and a 2D description of the cathode geometries are used to estimate the cathode performance. The goal is to identify the structure that maximizes the current generation/minimizes the cathode resistance. The model of the SOFC is reduced to a periodic, 2D conduction problem over a rectangular representative cell with design-dependent ionic transfer boundary conditions. Special techniques are introduced to avoid physically inadmissible designs that would otherwise be allowed by the 2D model. The designs with different material properties and resource restrictions are investigated.

2.1 Simplified analysis model of infiltrated composite cathode

The performance of the cathode considered here can be modeled in a manner similar to the models presented in Nicholas and Barnett [45], Shah et al. [8] and Tanner et al. [13]. The

approach is summarized below.

The modeling of the composite cathode begins by assuming that the oxygen ionic flux density across the ionic conductor is a dilute thermodynamics process that can be described by the Nernst–Planck equation [45]

$$\sum_i J_i = (\sum_i z_i \mu_i F c_i) \nabla \phi - \sum_i D_i \nabla c_i + c_i \mathbf{v} \quad (2.1)$$

In EQ. 2.1 the index i denotes the type of particle, J_i represents the atomic flux, z_i the charge per particle, μ_i the mobility, c_i the concentration, D_i the diffusivity, and \mathbf{v} the convective velocity. F is Faraday’s constant.

The first term in EQ. 2.1 corresponds to the electro-migration term which represents the flow driven by the electrical potential. The second and third terms are, respectively, diffusion and convection terms. In the case of low current densities and high porosities, all three terms can be considered independently [13].

The atomic flux in fuel cell can work in two functions: one is the fuel cell function, in which the current is driven by the diffusion of oxygen ions; the other is the electrolyer function, in which the current is driven by an applied driving potential. In the measurement of cathode resistance, the fuel cell works in the electrolyer function, and in this case, the diffusion and convection terms are zero or negligible. Thus, if one considers only one type of ionic charge carrier (such as oxygen vacancies), the effect of migration can be expressed simply as

$$\mathbf{J} = -\sigma_0 \nabla \phi \quad (2.2)$$

where $\sigma_0 = z\mu F_0 c$ is the ionic conductivity in the ionic conductor.

In EQ. 2.2, the current flow is proportional to the potential gradient, so the resistance of the ionic conductor is ohmic. For a steady state flow, by the continuity condition of the flow,

$$\nabla \cdot \mathbf{J} = 0 \quad (2.3)$$

and thus the potential distribution in the ionic conductor is governed by Laplace's equation

$$\nabla \cdot (\sigma_0 \nabla \phi) = 0 \quad (2.4)$$

The discrete electrocatalyst nano-particles deposited on the ion conducting scaffold are modeled as a continuous mixed conductor (MIEC) coating. In this coating, the resistance can be considered as a uniform surface resistance of magnitude R_S [13][45], so that the current flux density across the coating, Q , can be written in the form of Ohm's law

$$Q = \frac{\phi_\infty - \phi}{R_S} = h_0(\phi_\infty - \phi) \quad (2.5)$$

In EQ. 2.5 ϕ_∞ is the driving potential, ϕ is the electric potential in the mixed conductor, and the coefficient $h_0 \equiv 1/R_S$ is a property of the MIEC coating.

Due to the continuity of current density at the interface between the scaffold and the mixed conductor coating, the effect of the mixed conductor can be written as a convection-like (or Robin) boundary condition at the scaffold boundary by combining EQ. 2.2 and EQ. 2.5 into

$$\sigma_0 \nabla \phi \cdot \mathbf{n} = h_0(\phi_\infty - \phi) \quad (2.6)$$

In summary, in the simplified cathode model, the electric potential ϕ is the solution to

$$\nabla \cdot (\sigma_0 \nabla \phi) = 0 \quad \text{in } \omega \quad (2.7)$$

$$\sigma_0 \nabla \phi \cdot \mathbf{n} = h_0(\phi_\infty - \phi) \quad \text{on } \Gamma_\omega \quad (2.8)$$

where the ionic conductor occupies the domain ω , an ionic transfer boundary condition is applied on the boundary of the ionic conductor Γ_ω , and a constant potential $\phi = 0$ is applied at the bottom of the electrolyte base Γ_0 . The formulation of this problem is similar to heat transfer problem with a convection boundary condition.

2.2 The simple model as a periodic single column reference design

A reference design with a series of 1D periodic rectangular column has been used to provide a

good estimation of the cathode resistance (Fig. 2.1). The estimated cathode resistance is used as reference data for the comparison purpose in this chapter. The analytical solution of the cathode resistance of the reference design was proposed by Tanner, Fung and Virkar [13], and the solution was modified to handle nano-composite electrodes by Nicholas and Barnett [7].

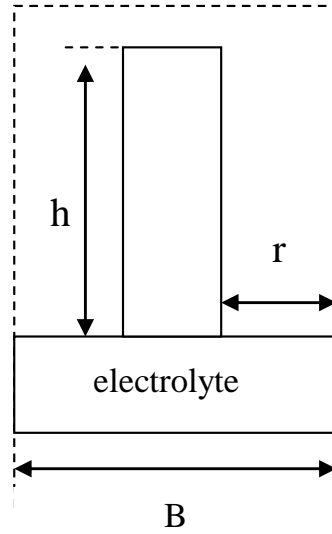


Figure 2.1 Geometry of the reference design used for comparison

The cathode resistance of the rectangular column design can be calculated by

$$R_P = \frac{rR_I}{c\left(\frac{1+\beta}{1+c^2\beta}\right)r\left(1-\frac{B}{2}\right) + (1+c)\left(\frac{1+\beta}{1+c^2\beta}\right)\alpha + \frac{B}{2}r} \quad (2.9)$$

where

$$c = \exp(-h/\alpha) \quad (2.10)$$

$$A = \sqrt{\sigma_0 r \left(1 - \frac{B}{2}\right) R_I} \quad (2.11)$$

$$\beta = \frac{\sigma_0 R_I - \alpha}{\sigma_0 R_I + \alpha} \quad (2.12)$$

σ_0 is the conductivity of the ionic conducting material and R_I is the surface resistance. For an

infiltrated cathode, Nicholas and Barnett [7] showed that R_I should be revised to be R_S , which is

$$R_S = R_I \frac{A_S}{A_I} \quad (2.13)$$

where A_S is the surface area of the ionic-conducting scaffold and A_I is the surface area of the infiltrated mixed conductor particles.

2.3 Finite element model for 2D topology optimization problem

For an arbitrary design with non-regular geometries, the finite element method can be used to calculate the cathode resistance. The weak form associated with the governing equation is

$$\int_{\omega} \nabla \bar{\phi} \cdot (\sigma_0 \nabla \phi) dA - \int_{\Gamma_{\omega}} \bar{\phi} h_0 (\phi_{\infty} - \phi) dl = 0 \quad \forall \bar{\phi} \in \mathcal{V}_{\omega}^0 \quad (2.14)$$

where $\phi \in \mathcal{V}_{\omega}$ and \mathcal{V}_{ω} and \mathcal{V}_{ω}^0 are suitable sets of admissible functions defined of ω .

To complete the model, the composite cathode is assumed to be periodic in the horizontal direction with a periodicity characterized by an (irreducible) unit cell, so periodic boundary conditions are applied on the left and right boundaries, denoted by Γ_P as illustrated in Fig. 2.2(a).

In the model, ω , the region occupied by the scaffold material, consists of two distinct components: the cathode and the electrolyte, and both are assumed to have the same conductivity σ_0 . However, only the scaffold is subjected to design.

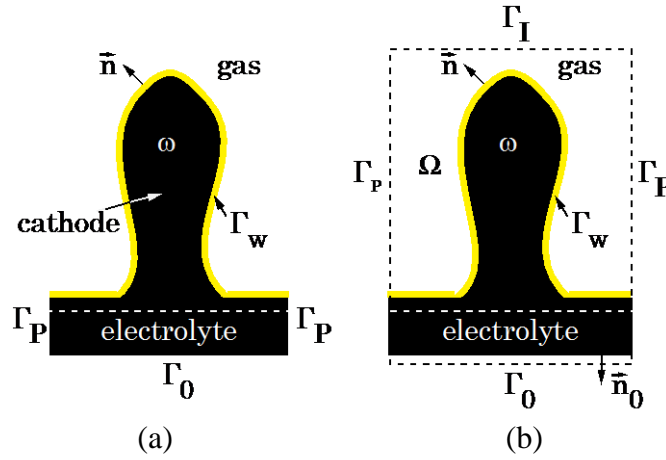


Figure 2.2 A periodic computational domain is used in the cathode model as shown in a but it is extended as in b to allow the exploration of the entire space through topology optimization

As the shape of the cathode is unknown, the topology optimization problem involves design dependent boundaries, at which the boundary conditions cannot be set directly. This type of problems has been discussed by various authors in the context of heat conduction. For instance, Yoon and Kim [34] proposed an “element connectivity parameterization” method to consider design-dependent effects for thermal boundary conditions. Bruns [35] investigated a 2D problem with convection both on the top and on the boundary of the structure. Iga et al. [36] introduced a smeared-out hat function to extract the side convection.

For the purpose of topology optimization, the shape of the cathode is characterized by the distribution of cathode (ionic conducting scaffold) material within the (rectangular) unit cell Ω , the computational domain (Fig. 2.2(b)). The area in Ω that is not occupied by scaffold material or electrolyte (i.e., the set $\Omega \setminus \omega$) is occupied by gas. In an analysis suitable for topology optimization, the weak form in EQ. 2.14 is extended to the whole computational domain Ω . Glowinski et al.[46] validate this extension by showing that there exist functions $\sigma(x)$, $\chi_\omega(x)$ and $F(x)$ defined on Ω such that

$$\int_{\omega} \nabla \bar{\phi} \cdot (\sigma_0 \nabla \phi) dA = \int_{\Omega} \nabla \bar{\phi}_{\Omega} \cdot (\sigma \nabla \phi_{\Omega}) dA \quad \forall \bar{\phi}_{\Omega} \in \mathcal{V}_{\Omega}^0 \quad (2.15)$$

and

$$\int_{\Gamma_{\omega}} \bar{\phi} h_0(\phi_{\infty} - \phi) dl = \int_{\Omega} \bar{\phi}_{\Omega} h_0(\phi_{\infty} - \phi_{\Omega}) \nabla \chi_{\omega} \cdot \frac{\nabla F}{|\nabla F|} dA \quad \forall \bar{\phi}_{\Omega} \in \mathcal{V}_{\Omega}^0 \quad (2.16)$$

Functions ϕ_{Ω} and $\bar{\phi}_{\Omega}$ are, respectively, Ω -periodic extensions of ϕ and $\bar{\phi}$ in suitable admissible spaces \mathcal{V}_{Ω} and \mathcal{V}_{Ω}^0 , $\chi_{\omega}(x)$ is the characteristic function of ω in Ω , and $F(x)$ is a function satisfying $F(x) = 0$ only on Γ_{ω} (see Wells and Zhou [47] for details). Material properties (conductivity) in Ω are characterized by $\sigma(x)$, which is assumed to have the form

$$\sigma_e(x) = \begin{cases} \sigma_0 & \text{if } x \in \omega \\ \sigma_{\epsilon} & \text{if } x \in \Omega \setminus \omega \end{cases} \quad (2.17)$$

Where $0 < \sigma_{\epsilon} \ll \sigma_0$. Note that no distinction is made between the conductivity of scaffold and electrolyte material. Typically, they have the same conductivity σ_0 .

Discretization of the domain Ω is by rectangular, four node elements. The conductivity $\sigma_e(x)$ is piece-wise constant in Ω with discontinuities only at element boundaries. Denoting the conductivity in the e -th element by σ_e and letting $h_{\partial e}$ represent the (inverse) surface resistance coefficient across the boundary ∂e of element e , and substituting EQ. 2.15 and EQ. 2.16 into EQ. 2.14, EQ. 2.14 can be rewritten as

$$\sum_e \int_{\Omega_e} \nabla \bar{\phi} \cdot (\sigma_e \nabla \phi) dA - \sum_e \int_{\partial e} \bar{\phi} h_{\partial e} (\phi_{\infty} - \phi) dl = 0 \quad \forall \bar{\phi} \in \mathcal{V}_{\Omega}^0 \quad (2.18)$$

Noting that the second term in EQ. 2.18 can be converted to an integral in the whole analysis domain

$$\int_{\Omega} \bar{\phi}_{\Omega} h_0(\phi_{\infty} - \phi_{\Omega}) \nabla \chi_{\omega} \cdot \frac{\nabla F}{|\nabla F|} dA = \sum_e \int_{\partial e \cup \Gamma_{\omega}} \bar{\phi} h_0(\phi_{\infty} - \phi) dl \quad (2.19)$$

That is because $\nabla F / |\nabla F|$ coincides with the unit boundary normal vector \mathbf{n} of ω on Γ_{ω} , and $\nabla \chi_{\omega} \cdot \mathbf{n}$ has nonzero values only in a small neighborhood of Γ_{ω} , in writing EQ. 2.18 we have

assumed that Γ_ω coincides with element boundaries. In the same manner as the single column model in section 2.2, Ω is assumed to be a rectangular periodic cell. (Fig. 2.3)

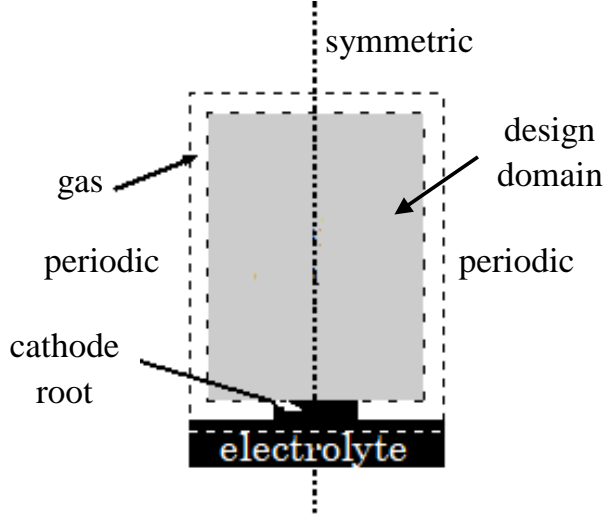


Figure 2.3 Sketch of periodic cell.

One can introduce a design variable ρ to control the material distribution in Ω . We use a SIMP like approach [31], let $\rho: \Omega \rightarrow [0, 1]$ be also piece-wise constant in Ω with values ρ_e within element e , and express material properties σ_e and $h_{\partial e}$ as

$$\sigma_e = \sigma_0 \rho_e^p + \sigma_\epsilon (1 - \rho_e^p) \quad (2.20)$$

and

$$h_{\partial e}^j = \frac{h_0}{2} \left(\sqrt{(\rho_e - \rho_e^j)^2 + \epsilon^2} - \epsilon \right) / \left(\sqrt{1 + \epsilon^2} - \epsilon \right) \quad (2.21)$$

In EQ. 2.20 and EQ. 2.21 ρ_e^j and $h_{\partial e}^j$ represent, respectively, the density and the (inverse) surface resistance coefficient across the j -th side of element e ($j = 1, 2, 3$ or 4) and p is the penalty factor in the SIMP model [31]. Note from (14) that $h_{\partial e}^j = 0$ if there is no change in material properties across the j -th side of element e and that $h_{\partial e}^j$ is differentiable at $\rho_e - \rho_e^j = 0$ if $0 < \epsilon \ll 1$, e.g., $\epsilon = 0.001$.

2.4 Objective function

The goal of the optimization problem is to find cathode shapes that minimize resistance at the base of the cell boundary Γ_0 . The cathode resistance is calculated by Nicholas and Barnett [45] as

$$R_P = \frac{\phi_\infty}{\frac{1}{B} \int_{\Gamma_0} (\sigma_0 \nabla \phi) \cdot \mathbf{n}_0 dl} - \frac{d}{\sigma_0} \quad (2.22)$$

where ϕ_∞ is the driving potential, B is the footprint (length of Γ_0), \mathbf{n}_0 is the outward normal on Γ_0 (Fig. 2.2), d is the thickness of the electrolyte base, and σ_0 is the conductivity of the conducting material. ϕ_∞ , B , \mathbf{n}_0 and d are all design independent, so minimizing R_P is equivalent to maximizing the denominator of the first term in EQ. 2.22,

$$f = \int_{\Gamma_0} (\sigma_0 \nabla \phi) \cdot \mathbf{n}_0 dl \quad (2.23)$$

which is the total current density flow through Γ_0 . This is the objective function in this chapter.

2.5 Constraints

Regardless of the shape of the cathode, the model in Section 2.2 predicts a smaller resistance for larger perimeter and larger amount of scaffold material. Larger perimeter is better simply because the current comes from the ionic transfer boundary condition. More material is better because a more massive scaffold offers less resistance to current. In order to extract the effect of shape alone, isoperimetric constraints are imposed on the perimeter and amount of material.

The perimeter of the cathode can be expressed as

$$P = \frac{1}{h_0} \sum_e \sum_{j=1}^4 h_{\partial e}^j L_e^j \quad (2.24)$$

where L_e^j is the length of the j -th side of element e .

The total amount of scaffold material can be measured using the element densities as

$$W = \sum_e \rho_e A_e \quad (2.25)$$

where A_e is the element area.

The perimeter and material constraints are used to control the size of the features allowed in the solution, a limitation associated with the manufacturing process and our modeling assumptions.

The smallest feature is limited by the size of the particles of ionic conducting material used to build the scaffold. In addition, the assumption that the MIEC is uniformly spread over the scaffold also imposes a constraint on the smallest feature size. We use the upper bounds on the perimeter and amount of material (respectively, P_R and W_R) to parameterize solutions with different feature sizes: smaller bounds P_R (larger bounds W_R) lead — on average — to larger features. Using these bounds to control feature size is an arbitrary choice that works well in this case. A filter has a similar effect, but it typically leads to solutions with more “gray” areas.

2.6 The optimization problem

Based on the objective function in Section 2.4 and the constraints in Section 2.5, the optimization problem is:

Find $\rho \in \Theta$ that

Maximize

$$f(\phi, \rho) = \int_{\Gamma_0} (\sigma_0 \nabla \phi) \cdot \mathbf{n}_0 dl \quad (2.26)$$

Subject to

$$W \leq W_R$$

$$P \leq P_R$$

$$0 \leq \rho_e \leq 1, \quad e=1, 2, 3, \dots, N$$

and (discretized) state equations, discussed in Section 2.9 below. In this problem W_R and P_R are

prescribed upper bounds on the total amount of material and perimeter, respectively. The set Θ is used simply to define regions Ω_0 and Ω_1 where the conducting material is prescribed.

Specifically,

$$\Theta := \{\rho \in [0, 1]^N : \rho_e = 0 \text{ if } e \in \Omega_0, \rho_e = 1 \text{ if } e \in \Omega_1\} \quad (2.27)$$

In EQ. 2.27 Ω_0 and Ω_1 are subsets of Ω where ρ is prescribed to have value 0 (gas) or 1 (scaffold or electrolyte), respectively.

To break the symmetry of the periodic cell and to assign the spatial frequency of the cathode column, an electrolyte root is prescribed in the design domain (Fig 2.3). Also, to prevent the columns to connect together and form physically inadmissible design, a gas region is assigned around the design domain.

2.7 Filters

A density filter with a linear weight [48] is used to prevent the appearance of checkerboard patterns and to control feature size. A smoothed Heaviside projection function [49] is used to facilitate convergence to binary solutions. The variable used in the computation of material properties in EQ. 2.24-25 are then

$$\hat{\rho}_e^H = 0.5 + 0.5 \tanh\left(\beta(\hat{\rho}_e - 0.5)\right) / \tanh(0.5\beta) \quad (2.28)$$

where $\hat{\rho}_e$ is the filtered density and β is a scaling factor that determines the sharpness of the projection.

2.8 Techniques to reject inadmissible designs

Because of simplifications introduced by the cathode model, the optimization problem may result in physically inadmissible SOFC designs, as explained below. As is the case with

checkerboard suppression schemes, special steps are required to penalize the formation of such designs.

The first type of inadmissible design is a hole inside the body of the cathode without access to gas, and it is simply because it cannot be supplied with ambient gas needed for the surface electrochemical reaction. However, the cathode model may identify an internal hole as a desirable feature since the ionic transfer boundary condition in the inner hole would produce current, even when the hole is not in contact with ambient gas. Large internal holes cannot be removed by standard filters and thus a special technique is needed to prevent their formation.

There are two mechanisms of forming a hole: One is by closing a “neck” region, trapping gas inside an area occupied by a scaffold, a situation illustrated in Fig. 2.4(a); the other is by reducing density in areas surrounded by the cathode material. Both of them can be identified by morphological techniques (Fig. 2.4(b)), and the internal holes can be eliminated by preventing the cathode branches from trapping a gas region and adding a negative current source to the reducing density areas surrounded by cathode material.

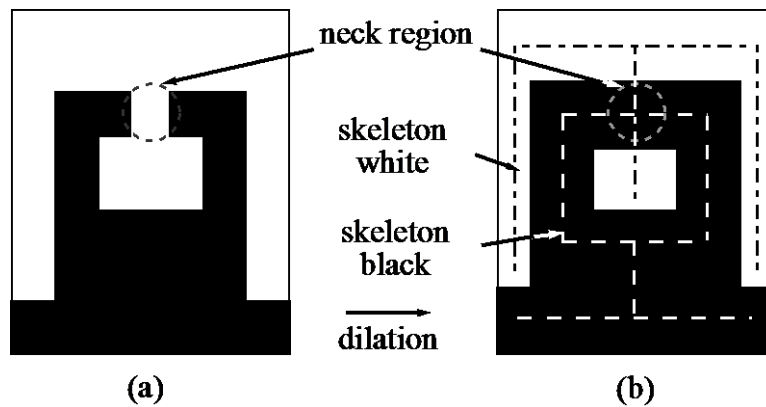


Figure 2.4 Detecting neck regions that may trap internal holes

The strength of the negative heat source is

$$q_A^e = q(1 - \hat{p}_e^H) \quad (2.29)$$

where q is a prescribed constant, (typically set to $q = 50h_0\Phi_\infty$). Once an area reaches an effective density $\hat{\rho}_e^H \approx 1$, elements in its interior are fixed to $\hat{\rho}_e^H = 1$ and removed from the design space by including e in Ω_1 .

The artificial negative current source used in EQ. 2.29 penalizes the presence of gas (white) that is fully trapped by scaffold material (black). A negative source absorbs current and thus it reduces the flow of ions to the electrolyte base. Since less ion flow at the base means that performance is degraded, designs with negative current are less desirable. By EQ. 2.29, the negative current can only be removed by turning trapped gas into scaffold material.

The second type of inadmissible design is the disjoint cathode material. To conduct current the cathode material must be singly connected and connected to gas and electrolyte. However, the cathode model may accept local optima which are not connected. To illustrate, consider the three designs in Fig. 2.5.

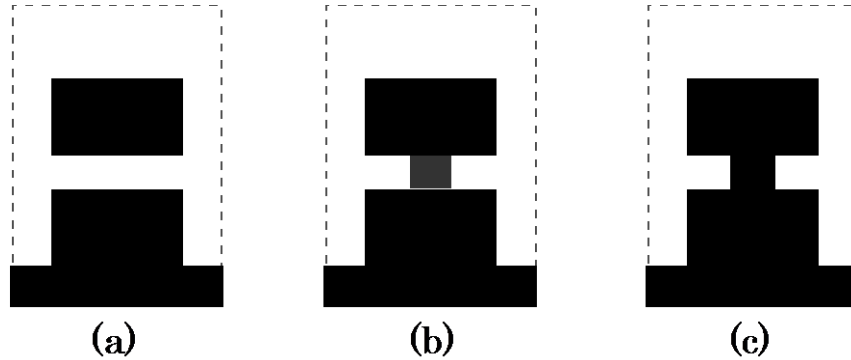


Figure 2.5 Cathode model may predict that (b) is worse than either (a) or (c)

Design (c) forms a better conduction path to the electrolyte than design (a) and should be the preferred solution. A change from (a) to (c) requires that the conductivity in the gap be increased, e.g., by increasing ρ_{GAP} slightly, as shown in design (b). However, if the conductivity within the gap is increased only slightly, design (b) may actually generate less current than either (a) or

(c). This is because the increased current caused by higher conductivity may be canceled by a simultaneous reduction in ionic transfer through boundaries near the gap. If this were to happen, the gradient of the objective function with respect to ρ_{GAP} will be positive and the gap will not close. To avoid this, a small amount of artificial surface ionic transfer with coefficient

$$h_A^e = h_0^A \left(\sqrt{(\hat{\rho}_e^H)^2 + \epsilon^2} \right) - \epsilon \quad (2.30)$$

of the order $h_0^A \approx h_0/l$ is allowed in all elements e in the design domain. l is the element length. This term will increase ionic transfer through the gap and make design (b) better than (a). Since surface ionic transfer may influence the cathode shape, it is gradually removed as iterations progress, i.e., the magnitude of h_0^A is decreased to zero gradually with iterations.

This method is not the best way to resolve the single connection problem, and an improved method will be discussed in Chapter 4.

2.9 Sensitivity Analysis

Upon assembly of element matrices, EQ. 2.18 becomes

$$(K_\sigma + H_h + K_A) \Phi = q_h + q_A \quad (2.31)$$

where Φ is the vector of values of the potential ϕ at the nodes. Matrices K_σ , H_h and vector q_h are assembled from element-level quantities

$$K_\sigma^e = \int_e \sigma_e \nabla N_e \nabla N_e^T dA \quad (2.32)$$

$$H_h^e = \int_{\partial e} h_e N_e N_e^T dl \quad (2.33)$$

$$q_h^e = \phi_\infty \int_{\partial e} h_{\partial e} N_e dl \quad (2.34)$$

where N_e represents the vector of shape functions of element e . Quantities K_A and q_A , added to the equilibrium equations, are needed when the special techniques introduced in Section 2.8

are applied to the model. They represent an artificial source of heat and are assembled from element-level quantities

$$\mathbf{K}_A^e = h_A^e \int_e N_e N_e^T dA \quad (2.35)$$

$$\mathbf{q}_A^e = (h_A^e \phi_\infty - q_A^e) \int_e N_e dl \quad (2.36)$$

Material properties σ_e and $h_{\partial e}$ associated with element e are related to the design variables $\rho = \{\rho_1, \rho_2, \dots, \rho_N\}$ through EQ. 2.24-25, respectively. Properties q_A^e and h_A^e associated with the artificial heat source are related to ρ through EQ. 2.29 and EQ. 2.30, respectively.

Upon discretization, the objective function EQ. 2.26 becomes

$$f = \mathbf{p}_f^T \Phi \quad (2.37)$$

where \mathbf{p}_f is assembled from

$$\mathbf{p}_f^T = -\sigma_0 \int_{\partial e \cap \Gamma_0} \nabla N_e \cdot \mathbf{n}_0 dl \quad (2.38)$$

The sensitivity of f is obtained from

$$\frac{\partial f}{\partial \rho_e} = \widehat{\Phi}^T \left(-\frac{\partial(K_\sigma + H_h + K_A)}{\partial \rho_e} \Phi + \frac{\partial(q_h + q_a)}{\partial \rho_e} \right) \quad (2.39)$$

where $\widehat{\Phi}$ is the solution of the adjoint problem

$$(K_\sigma + H_h + K_A) \widehat{\Phi} = \mathbf{p}_f \quad (2.40)$$

2.10 Examples

In the following examples we investigate the influence of changes in material properties, allowable perimeter, and the amount of cathode material used. Since infiltration typically produces MIEC nano-particles 50–70 nm in diameter, the smallest feature size that can modeled before the assumption that the MIEC is uniformly spread over the scaffold is violated may be of the order of 300 nm, so the element size is selected in the same order of the smallest feature size. In the examples all length dimensions are expressed as multiples of element length. Except as noted, square elements with $l=1$ are used. Material properties and dimensions can be scaled by

the ratio h_0/σ_0 . Except as noted, we set $h_0/\sigma_0 = 2.5 \times 10^{-4}$. This results in material properties consistent with values reported in Nicholas and Barnett [7] and Shah et al. [8]. Except as noted, in all examples the height of the electrolyte base is $d = 6$ and the fixed gas layer above the electrolyte and on the cell sides (see Fig. 2.3) is 2. The cathode root (i.e., the area of fixed density that connects the scaffold material to the electrolyte) is $B/3 \times 2$. Note that in scaling the problem one needs to be mindful of the limitations of the analysis model. Since infiltration typically produces MIEC nano-particles 50–70 nm in diameter, the smallest feature size that can modeled before the assumption that the MIEC is uniformly spread over the scaffold is violated may be of the order of 300 nm.

Finally, all designs are forced to be left-right symmetric. All optimization problems are solved using the method of moving asymptotes of Svanberg [50]. Results reported are after post-processing, applying a threshold at $\rho = 0.5$ to remove a very small number of intermediate density elements left in the optimal solutions.

2.10.1 Designs with different material properties

In this example the unit cell is $60 \times 40(l)$. The constraint bounds are $P_R = 360$ and $W_R = 0.25W_\Omega$ where W_Ω is the area of Ω .

Figure 2.6 and Table 2.1 illustrate the effect of varying the ratio h_0/σ_0 on the optimal solution. Larger ratios are associated with higher performance electrocatalyst material. In the solutions shown in Fig. 2.6a, b and c, h_0/σ_0 is smaller, surface resistance dominates scaffold resistance and therefore the optimized designs tend to exhibit larger perimeter and more and longer branches. The ratio (b) used in the solution shown in Fig. 2.6d is larger, the electrocatalyst material is more effective, and focus shifts from the perimeter to the body of the scaffold.

Performance is improved in this range by emphasizing the path of the ions through the scaffold rather than by increasing the perimeter. The increased flux through the boundary that results from the improved coating material calls for a well-designed path to the electrolyte at the bottom to improve performance.

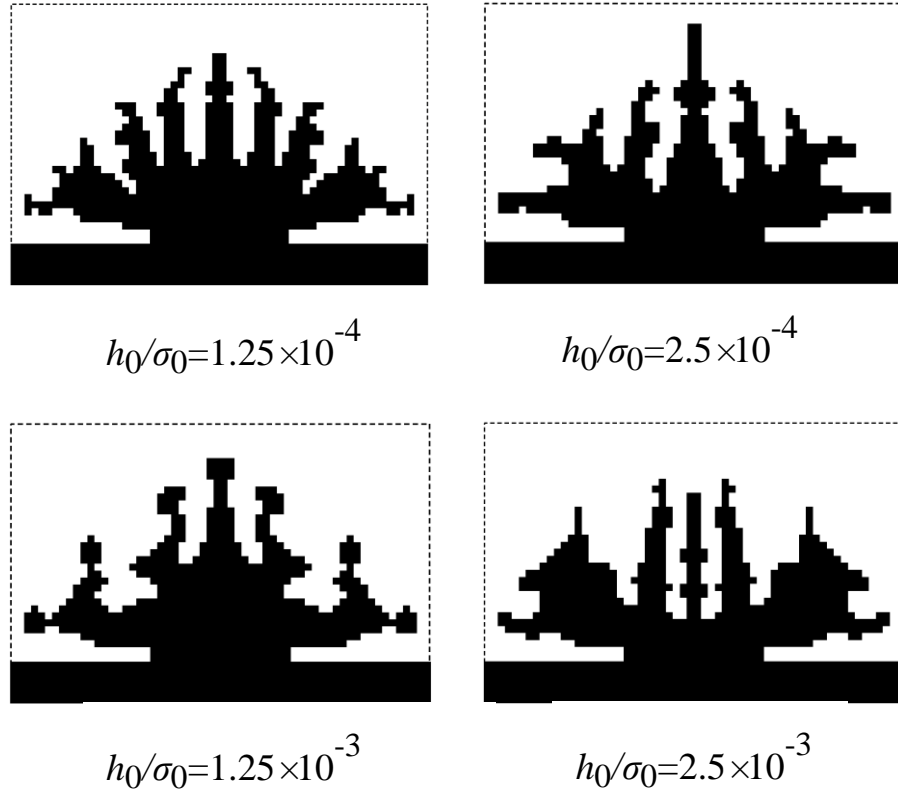


Figure 2.6 Optimized designs for different values of h_0/σ_0 . As h_0/σ_0 increases, the perimeter becomes less important and the shape of the scaffold begins to dominate. Performances reported in Table 2.1

Table 2.1 Performance of optimized designs for different materials, where R can be multiplied by l/σ_0 to recover units (Fig. 2.6)

Design	$h_0/\sigma_0 \times 10^4$	$R_P \times 10^{-3}$	$R_{REF} \times 10^{-3}$	Improvement (%)
(a)	$1.25/l$	1.33	1.80	26
(b)	$2.5/l$	0.72	1.07	33
(c)	$12.5/l$	0.17	0.35	51
(d)	$25/l$	0.097	0.21	54

2.10.2 Design with varying footprint B and constant perimeter/footprint ratio

In this example the unit cell has a height of $60(l)$ and varying footprint B . The bound on the amount of material is $W_R = 0.25W_\Omega$. Fig. 2.7 and Table 2.2 illustrate the effect of varying B while keeping the ratio $P_B/B = 9$ on the optimal solution.

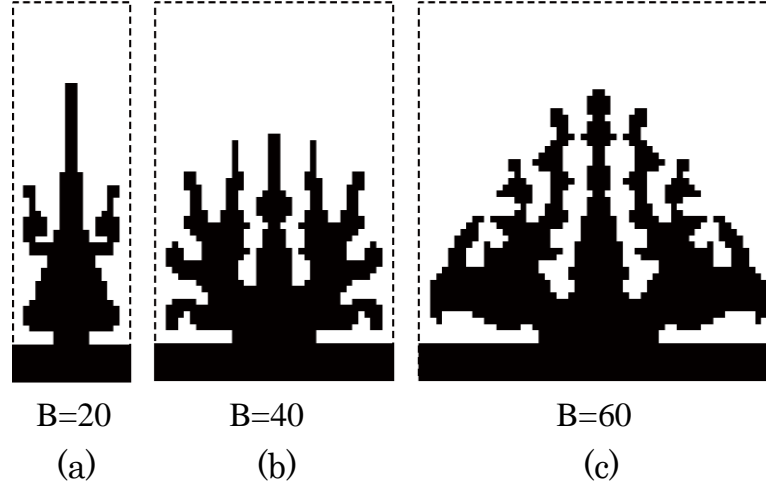


Figure 2.7 Optimized designs for different footprints B and $P_B/B = 9$. For a large footprint, the cathode shape becomes more convoluted and departs further from a columnar shape, not being confined by the design space. Performances reported in Table 2.2

Table 2.2 Performance of optimized designs for different footprints B and $P_B/B = 9$, where R can be multiplied by l/σ_0 to recover units (Fig. 2.7)

Design	B/l	$R_P \times 10^{-3}$	$R_{\text{REF}} \times 10^{-3}$	Improvement (%)
(a)	20	0.46	0.56	18
(b)	40	0.49	0.80	39
(c)	60	0.54	1.05	49

As shown in Table 2.2, R_P remains nearly constant in all optimized designs obtained while varying B while keeping the ratio P_B/B constant. However, the optimized design performs better than a reference design of the same perimeter and footprint. This improvement relative to the reference design is more pronounced as the footprint increases, indicating that cathode shape is

more important for larger footprints.

2.10.3 Design with varying perimeter P and amount of material W while keeping the footprint constant

In this example the unit cell is $60 \times 40(l)$. Figure 2.8 and Table 2.3 illustrate the effect of varying P_R , with $W_R = cW_\Omega$ where $c=0.167, 0.25, 0.33$, for P_R/l equal to 260, 360, and 460, respectively.

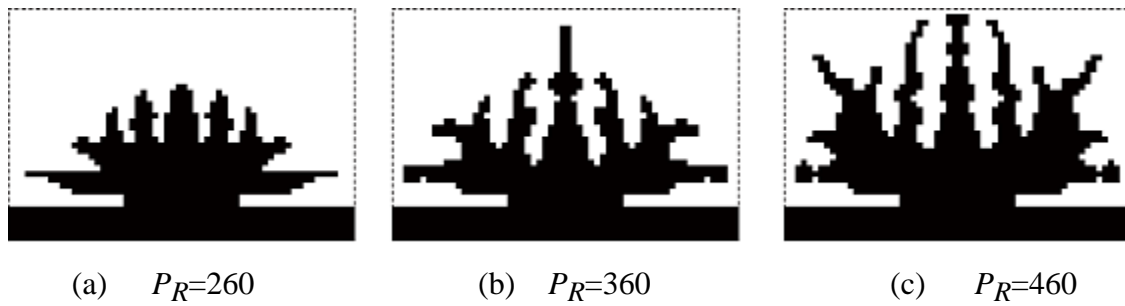


Figure 2.8 Optimized designs for different values of the perimeter bound P_R . As expected, a large perimeter corresponds to a greater performance improvement. Performances reported in Table 2.3

Table 2.3 Performance of optimized designs for different values of the perimeter bound P_R , where R can be multiplied by l/σ_0 to recover units (Fig. 2.9)

Design	P_R/l	$R_P \times 10^{-3}$	$R_{REF} \times 10^{-3}$	Improvement (%)
(a)	260	0.94	1.19	21
(b)	360	0.72	1.07	33
(c)	460	0.57	1.04	45

As shown in Table 2.3, R_P decreases with increasing perimeter. The percentage of improvement compared with the reference design also increases with perimeter.

2.10.4 Design with varying amount of material

In this example the unit cell is $40 \times 60(l)$. The cathode root has a width of 14. The upper bound

on the perimeter is $P_R = 360$. Fig. 2.9 and Table 2.4 illustrate the effect of varying the bound on the amount of material, W_R . Results show that for the material used, $h_0/\sigma_0 = 2.5 \times 10^{-4}$, this is a perimeter-dominated problem. Since the perimeter is the same in all solutions, the resistance is also the same. Increasing the amount of material does not affect the answer.

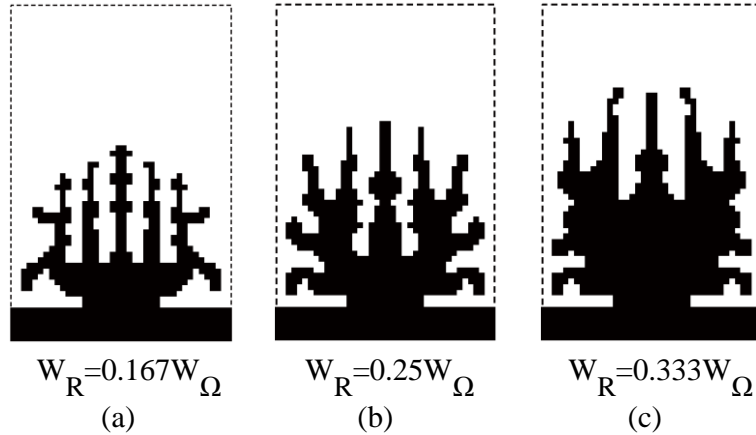


Figure 2.9 Optimized designs for different values of the amount of material bound W_R . Performances reported in Table 2.4

Table 2.4 Performance of optimized designs for different values of the amount of material bound W_R , where R can be multiplied by l/σ_0 to recover units (Fig. 2.9)

Design	W_R/W_Ω	$R_P \times 10^{-3}$	$R_{REF} \times 10^{-3}$	Improvement (%)
(a)	0.167	0.49	0.91	46
(b)	0.25	0.49	0.80	39
(c)	0.333	0.49	0.73	33

2.11 Conclusions

The designs found in this chapter were very intricate and obviously difficult to realize. However, the results are useful in that they provide insights on the characteristics of optimal microstructures and guidance on what features to emphasize in cathode design. Improvements of nearly 50 % were found, compared to a simple column design. The perimeter was found to be of the utmost importance in optimizing the microstructure. However, as the ionic transfer efficacy

of the MIEC particle coating improves, the shape of the scaffold also becomes important. The studies point to the importance of the microstructure in the performance of SOFCs and suggest that significant improvements are possible by proper organization of the microstructure.

In addition, the 2D optimization model was set up based on the methodology that uses 2D geometries to evaluate the performance of 3D microstructures. However, the complicated connections between different parts of the 3D scaffold microstructure cannot be simulated by the 2D model, and the 2D designs are also not able to improve these connections. A 3D simulation model and a 3D topology optimization model are proposed in Chapters 3-4 to resolve these problems.

Chapter 3 A 3D finite element model for cathode microstructure of solid oxide fuel cell cathodes

In this chapter, a 3D finite element formulation is developed to overcome the limitations in the 2D simple model introduced in section 2.2. The evaluation of the cathode resistance of a porous cathode microstructure is discussed, with an emphasis on the effect of the surface resistance of the MIEC coating, the bulk resistance of the ionic conducting scaffold and the gas diffusion in the pores. To validate the 3D finite element model, a detailed mesh is reconstructed from the experimental data from 3D Focused Ion Beam-Scanning Electron Microscopy, and the simulation results with different sets of material properties are compared with experimentally measured results.

3.1 Analysis model of infiltrated composite cathode

In the cathode microstructure, the oxygen gas is supplied on the top of the cathode, and it flows through the holes inside the porous cathode to the mixed conductor at the surface of the cathode scaffold. Electrochemical reactions, which consume oxygen gas and generate current, happen in the mixed conductor. The current flows through the cathode scaffold to the electrolyte at the bottom of the cathode (Fig. 3.1).

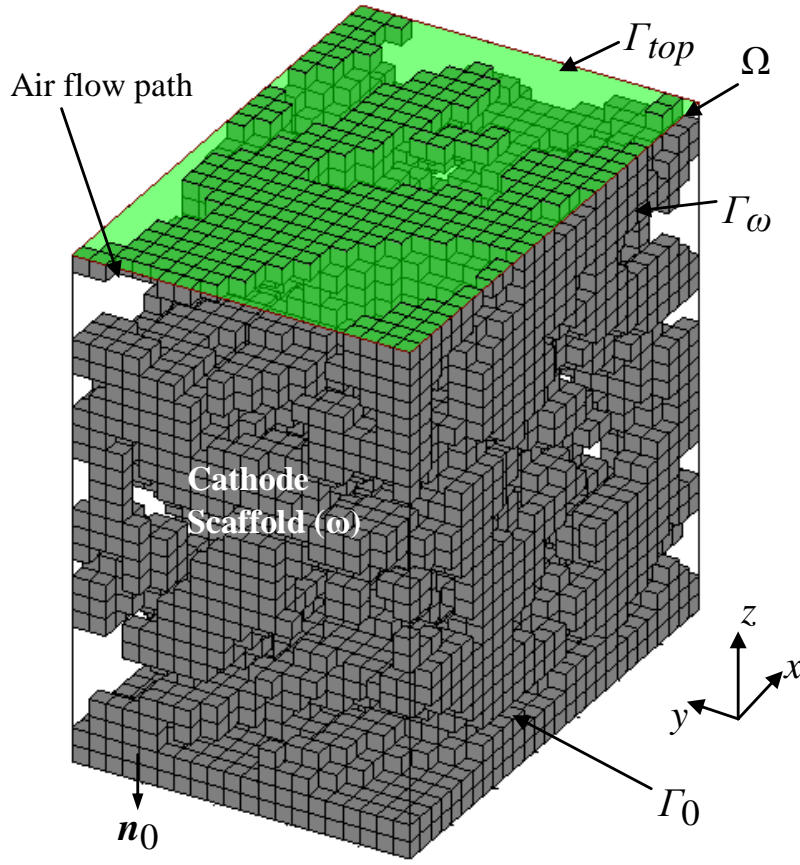


Figure 3.1 The sketch of a 3D cathode microstructure

An analysis model is performed below to simulate the current generation in the MIEC layer and the current flow through the ionic conducting scaffold to the bottom. This simulation model is to be used as a preparation of the 3D optimization model in the next chapter. The analysis domain Ω is selected to be the region occupied by the solid cathode microstructure and the gas pores. The solid cathode region ω is a sub-domain of Ω , and $\Omega \setminus \omega$ corresponds to the fluid region. The current flow in ω is modeled in a similar manner with the 2D case, in which the current is described by the electrical potential distribution, and it is governed by Laplace's equation, as in chapter 2

$$\nabla \cdot (\sigma_0 \nabla \phi) = 0 \quad \text{in } \omega \quad (3.1)$$

In EQ. 3.1 ϕ is the ionic potential and σ_0 is the conductivity of the ionic conducting material.

The oxygen gas flow is diffusion dominated, so the concentration distribution also satisfies Laplace's equation

$$\nabla \cdot (\sigma_g \nabla c_{O_2}) = 0 \quad \text{in } \Omega \setminus \omega \quad (3.2)$$

where c_{O_2} is the oxygen gas concentration and σ_g is the diffusivity of the oxygen gas.

At the gas-cathode interface Γ_ω , the electrochemical reaction absorbs oxygen gas from the air and releases oxygen ion to the solid cathode, so the current generated by the electrochemical reaction is modeled using a convection-like oxygen exchange boundary condition. The dependency of the ionic potential distribution and the current generation density obeys Ohm's law at low current density [13],

$$i = \frac{\phi_\infty - \phi}{R_S} \quad \text{on } \Gamma_\omega \quad (3.3)$$

where i is the current generation per unit area of $\partial\omega$, ϕ_∞ is the driving potential which comes from the Nernst voltage, and R_S is the interface resistance.

The previous 2D model assumes that the oxygen gas supply is abundant, so the interface model is treated independent of the oxygen gas concentration. With the introduction of oxygen gas consumption, the interface resistance also depends on the concentration of oxygen gas by the Butler-Volmer equation [51]

$$R_S = \frac{\Phi_\infty - \Phi}{i_0} \quad (3.4)$$

$$i_0 = \gamma_c \left(\frac{c_{O_2}}{c^{ref}} \right)^{0.25} \exp \left(\frac{-E_{act,c}}{RT} \right) \quad (3.5)$$

where γ_c is the cathodic pre-exponential coefficients, c_{O_2} is the concentration of oxygen gas, c^{ref} is the reference concentration, $E_{act,c}$ is the cathodic activation energy, R is the universal gas constant and T is the temperature. All of these quantities are assumed to be constants that are

independent of the designs.

EQ. 3.5 can be linearized for the convenience of calculations, and EQ. 3.3-3.5 can be simplified as

$$i = h_c (\phi_\infty - \phi) c_{O_2} \quad \text{on } \Gamma_\omega \quad (3.6)$$

where $h_c = \gamma_c \left(\frac{c_{O_2}^{max}}{c^{ref}} \right)^{0.25} \exp\left(\frac{-E_{act,c}}{RT} \right) / c_{O_2}^{max}$ is an approximation of the oxygen exchange coefficient.

The corresponding oxygen gas loss is

$$Q = - \frac{h_0}{zqen_0} (\phi_\infty - \phi) c_{O_2} \quad \text{on } \Gamma_\omega \quad (3.7)$$

where z is the particle charge of oxygen ion, q_e is the electron charge and n_0 is the Avogadro constant.

3.2 Finite element formulation of 3D cathode microstructure

For a specified cathode microstructure, a finite element method can be used to calculate the cathode resistance. Weak forms associated with the governing equations are

$$\int_\omega \nabla \bar{\phi} \cdot (\sigma_0 \nabla \phi) dV - \int_{\Gamma_\omega} \bar{\phi} h_0 (\phi_\infty - \phi) c_{O_2} dA = 0 \quad \forall \bar{\phi} \in V_\omega^0 \quad (3.8)$$

and

$$\int_{\Omega \setminus \omega} \nabla \overline{c_{O_2}} \cdot (\sigma_g \nabla c_{O_2}) dV - \int_{\Gamma_\omega} \overline{c_{O_2}} \left(- \frac{h_0}{zqen_0} (\phi_\infty - \phi) c_{O_2} \right) dA = 0$$

$$\forall c_{O_2} \in V_{\Omega \setminus \omega}^0 \quad (3.9)$$

where $\phi \in V_\omega$ and V_ω and V_ω^0 are suitable sets of admissible functions defined of ω , and $c_{O_2} \in V_{\Omega \setminus \omega}$ and $V_{\Omega \setminus \omega}$ and $V_{\Omega \setminus \omega}^0$ are suitable sets of admissible functions defined of $\Omega \setminus \omega$.

A constant potential $\phi = 0$ is applied at the bottom Γ_0 of the analysis domain Ω , and the concentration of oxygen gas c_{O_2} is assigned to be the same as that in the standard atmosphere at the top Γ_{top} of the analysis domain Ω , as illustrated in Fig. 3.1.

In preparation for the optimization work in chapter 4, both of the sub domains for current flow and gas diffusion are extended to the whole analysis domain Ω , in the same way as in chapter 2. Also, the analysis domain is discretized uniformly by identically shaped rectangular elements, and only the element boundaries ∂e can be considered as the boundary of the cathode Γ_ω

$$\sum_e \int_{\Omega_e} \nabla \bar{\phi} \cdot (\sigma_e \nabla \phi) dV - \sum_e \int_{\Gamma_\omega} \bar{\phi} h_0 (\phi_\infty - \phi) c_{O_2} dA = 0 \quad \forall \bar{\phi} \in V_\Omega^0 \quad (3.10)$$

$$\sum_e \int_{\Omega_e} \nabla \bar{c}_{O_2} \cdot (\sigma_g \nabla c_{O_2}) dV - \sum_e \int_{\Gamma_\omega} \bar{c}_{O_2} \left(-\frac{h_0}{zq_e n_0} (\phi_\infty - \phi) c_{O_2} \right) dA = 0$$

$$\forall \bar{c}_{O_2} \in V_{\Omega,g}^0 \quad (3.11)$$

Functions ϕ_Ω , $\bar{\phi}_\Omega$, $c_{O_2}^\Omega$, $\bar{c}_{O_2}^\Omega$ are, respectively, extensions of ϕ , $\bar{\phi}$, c_{O_2} and \bar{c}_{O_2} in suitable admissible spaces V_Ω , V_Ω^0 , $V_{\Omega,g}$ and $V_{\Omega,g}^0$. Noting that

$$\sigma_e(x) = \begin{cases} \sigma_0 & \text{if } x \in \omega \\ \sigma_\epsilon & \text{if } x \in \Omega \setminus \omega \end{cases} \quad (3.12)$$

$$\sigma_g(x) = \begin{cases} \sigma_g^\epsilon & \text{if } x \in \omega \\ \sigma_g & \text{if } x \in \Omega \setminus \omega \end{cases} \quad (3.13)$$

where $0 < \sigma_\epsilon \ll \sigma_0$ and $0 < \sigma_g^\epsilon \ll \sigma_g$.

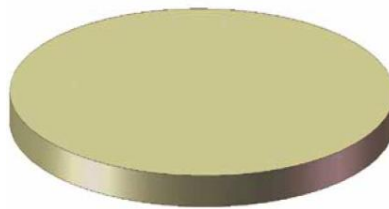
The cathode resistance is calculated by measuring the current flow through the bottom boundary Γ_0 of the cathode

$$R_P = \frac{\phi_\infty}{\frac{1}{A} \int_{\Gamma_0} (\sigma_e \nabla \phi) \cdot \mathbf{n}_0 dl} \quad (3.14)$$

where ϕ_∞ is the driving potential, A is the footprint (area of Γ_0), \mathbf{n}_0 is the outward normal on Γ_0 (Fig. 3.1).

3.3 Generation of 3D microstructure mesh from experimental data

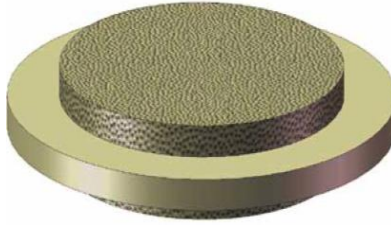
The micro-scale finite element model of the infiltrated composite cathode has been set up in section 3.2. Before applying the finite element model to the optimization work in chapter 4, the simulation result of the 3D finite element model should be validated by the experimental results. The most convenient way for the validation is to construct a 3D mesh of the 3D microstructure used in the experiment and compare the simulation results with the experimental results, and these require the reconstruction of the 3D microstructure of the cathode. First, the manufacturing process of the composite cathode is reviewed [14]. The cathode scaffold is made by (a) compressing and firing the particles of the ionic conducting material (CGO, etc.) into a pellet electrolyte base and (b) screen printing the ionic conducting particles onto the pellet and firing to make the particles merge into a porous scaffold. After that, (c) the electro-catalytic nano-particles (LSCF) are infiltrated into the scaffold, and they are fired to form a coating on the surface of the scaffold. The final step (d) is to print a current collector layer on the top, and oxygen gas can go through this layer to the cathode. In the experimental environment, one of the most common methods of reducing the surface resistance of the MIEC layer is to use smaller electro-catalytic nano-particles. The figures used below are from the work of Nicholas et al.[14] .



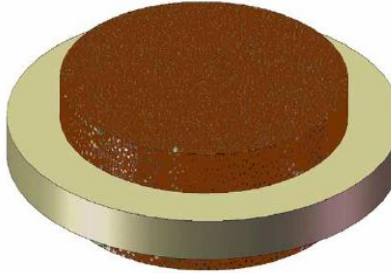
(a) Produce 98%+ Dense Ce_{0.9}Gd_{0.1}O_{1.95} (CGO) Pellets by Firing at 1450 °C for 6 hrs

Figure 3.2 The manufacture process of a SOFC composite cathode sample [14]

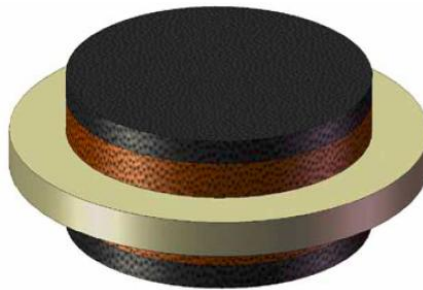
Figure 3.2(cont'd)



(b) Screen Print ~15mm Thick CGO Scaffold Layers, Fire at 1100 °C for 1 hr



(c) Infiltrate Nitrate Solutions into CGO Cathode, Gel Solutions at 80 °C, Fire at 800 °C for 1 hr



(d) Screen Print The Current Collector Layer, Fire at 800 °C for 1hr.

The randomness of the particle arrangement in (b) makes it difficult to give a good and detailed prediction to the resulting structure. Fortunately, the 3D microstructure can be reconstructed based on the experimental photos of the micro-scale scaffold cross sections.

2-D images of the electrode microstructures have been obtained from Dr. Scott Barnett's research group at Northwestern University [52][53]. The experimental photos can be made by (a) taking an image of the present surface of a pellet by 3D Focused Ion Beam-Scanning Electron Microscopy; (b) milling a slice of the pellet off from the side, and taking the image of the newly created surface; (c) stacking the surfaces together and interpolating the solid region between the

surfaces. The whole process is shown schematically in Fig. 3.3. The figure and data used in the reconstruction courtesy of Prof. Nicholas's group in Michigan State University [54].

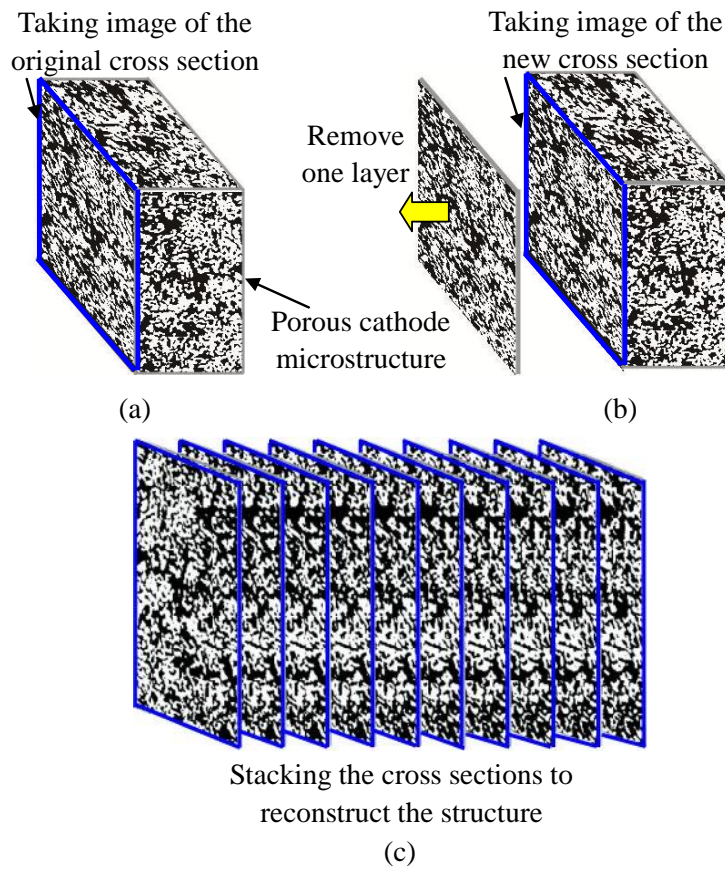


Figure 3.3 The reconstruction process using 3D Focused Ion Beam-Scanning Electron Microscopy.

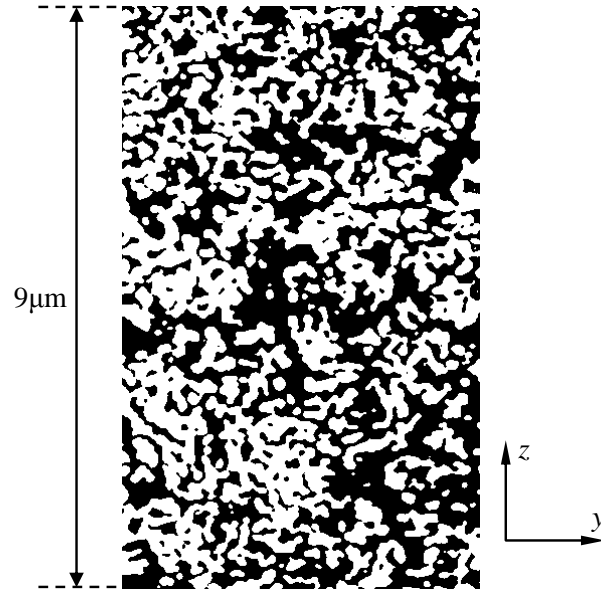


Figure 3.4 An example of a black-white image of a $9\mu\text{m}$ thick scaffold. Image courtesy of Prof. Nicholas's group in Michigan State University [54]

Fig. 3.4 shows an example of a black-white image of a 9 microns thick scaffold. The thickness of each slice is 24.8nm (x direction). Each pixel in the photo has a size of $15.63\text{nm} \times 15.63\text{nm}$ (y and z directions). The black pixels represent the ionic conducting particles, and the white pixels represent the void domain. Because the sizes of the particles are around $200\text{-}300\text{nm}$, which are much larger than the resolution level and the slice thickness, the images provide an accurate description of the microstructure.

The image pixels can be mapped into a 3D finite element mesh to reconstruct the microstructure. For the ease of the mapping, and also to make preparations for the following optimization in chapter 4, a uniform rectangular meshing is selected. Two types of elements are used: one is for the ionic conducting material; the other is for the void domain, which corresponding to black and white pixels in the photos as shown in Fig. 3.4, respectively.

Possibly easiest way of the mapping the black-white pixels into the two types of elements is a one to one mapping, in which each element corresponds to be one pixel in the photos, and the size of the element is determined by the size of the pixel and the thickness of each slice.

However, a one to one mapping will result in a very fine mesh, and the cost of the simulation can be prohibitive. To reduce the cost of the simulation, noting that the size of each pixel is much smaller than the size of the ionic conducting particle, pixels can be grouped, and each group is mapped into one element. In the following simulation, the sizes of the elements are selected to be $49.6\text{nm} \times 46.9\text{nm} \times 46.9\text{nm}$, which corresponds to a pixel group of $2 \times 3 \times 3$ (in x , y , z directions, respectively). In each pixel group, the black pixels have a grey scale 0, and the white pixels have a grey scale 255. If the average grey scale in one group is smaller than half of 255, the corresponding element is considered to be black, and otherwise it is assigned to be white.

The resulting 3D mesh of the 9 microns' thick cathode microstructure is shown in Fig. 3.5. The 'black' elements show the geometry of the scaffold, and the interfaces between the 'black' and the 'white' elements are the surfaces of the scaffold.

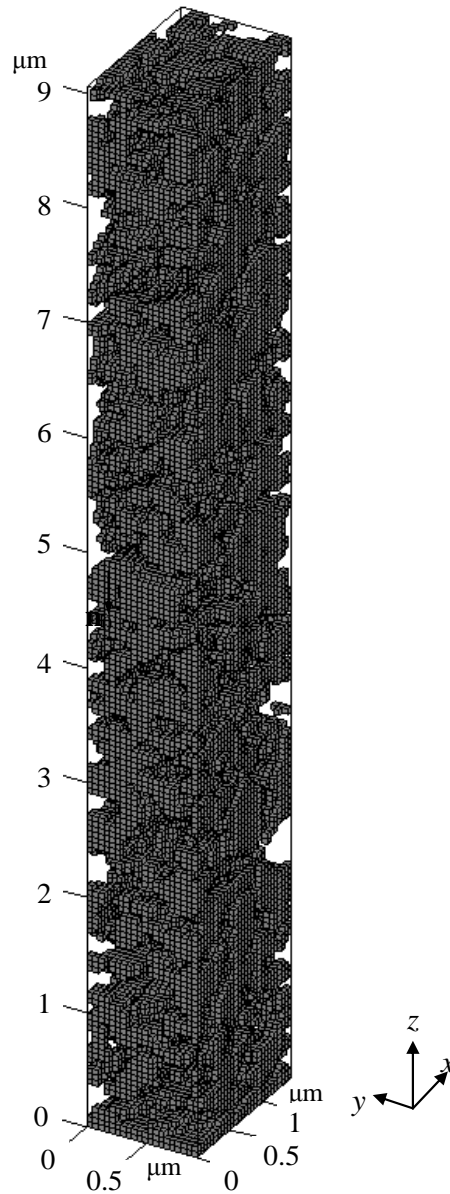


Figure 3.5 The 3D mesh of the 9 micron thick cathode microstructure

3.4 Examples of the simulation of the 3D cathode resistance

In the following example, the cathode resistance of the scaffold is estimated by using the finite element method introduced in section 3.2 and the 3D reconstructed microstructure shown in Fig. 3.5. The ionic conducting material is selected to be CGO, and the material for MIEC is selected to be LSCF.

The use of smaller LSCF particles can reduce the cathode resistance. Two particle sizes are

selected for the simulation. The surface resistance of the mixed conductor (LSCF) and the conductivity of the ionic conducting material (CGO) are shown in Tables 3.1-3.2 [54]-[56].

Table 3.1 Bulk conductivity of CGO ($G_{d0.1}C_{e0.9}O_2$)

Temperature (°C)	Temperature (1000/T(K))	Conductivity (S/cm)
400	1.485552997	1.76×10^{-3}
450	1.382838968	3.69×10^{-3}
500	1.293410076	6.90×10^{-3}
550	1.214845411	1.14×10^{-2}
600	1.145278589	1.77×10^{-2}
650	1.083247576	2.67×10^{-2}
700	1.027590813	3.86×10^{-2}

Table 3.2 Scaled ASR values for 20 nm MIEC LSCF ($L_{a0.6}S_{r0.4}C_{o0.8}F_{e0.2}O_3$) particle diameter

Temperature (°C)	Temperature (1000/T(K))	ASR ($\Omega \times \text{cm}^2$)
400	1.485552997	229.651
450	1.382838968	70.044
500	1.293410076	25.262
550	1.214845411	8.727
600	1.145278589	4.134
650	1.083247576	1.837
700	1.027590813	0.919

Table 3.3 Diffusivity and concentration of oxygen gas in air at 1atm [57]

Temperature (°C)	Temperature (1000/T(K))	σ_g (m ² /sec)	c_{max} (mol/m ³)
400	1.485552997	7.65×10^{-5}	3.58
450	1.382838968	8.52×10^{-5}	3.33
500	1.293410076	9.42×10^{-5}	3.11
550	1.214845411	1.03×10^{-4}	2.92
600	1.145278589	1.13×10^{-4}	2.75
650	1.083247576	1.23×10^{-4}	2.60
700	1.027590813	1.33×10^{-4}	2.47

The 9 μ m cathode sample reconstructed in section 3.3 is used. The 3D mesh has 28 \times 20 \times 193=108080 elements. The porosity denoted by *vol%* of the sample is 49.15%. The oxygen gas concentration is prescribed to be c_{max} at the top of the analysis domain Γ_{top} . Because the maximum values of σ_g and c_{max} shown in Table 3.3 are at most twice of the minimum values, and the change is much smaller than those of the conductivity and ASR shown in Tables 3.1-3.2 which can be as much as 20~200 times, the change of σ_g and c_{max} versus temperature is neglected. The values of σ_g and c_{max} at 600 °C are selected for all the temperatures in the following section except as noted.

3.5 Experimental validation and comparison with a simple estimation model

From a plot of the cathode resistance versus operating temperature, one can observe a significant increase of the cathode resistance as the temperature decreases. This reflects the main difficulty in the development of low temperature SOFC. The results are compared to the experimental results measured by the group of Prof. Nicholas [54], and the comparison is shown in Fig. 3.6. At

the low temperatures, a difference of less than 5% between the experimental data and the results of 3D model is observed. The calculated cathode resistance becomes significantly lower than the experimental result near the high temperature end, where the difference can be up to 50%.

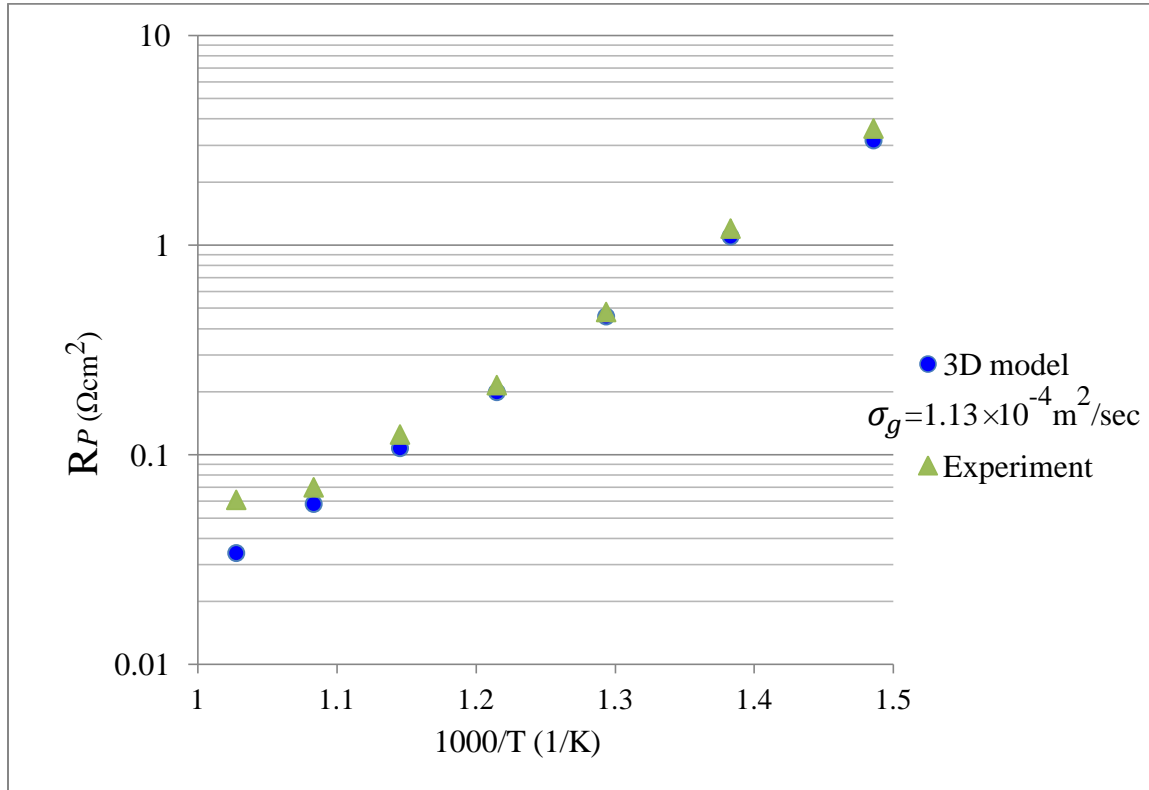


Figure 3.6 The comparison of R_P data for 20nm LSCF particles. Experimental data courtesy of Prof. Nicholas's group in Michigan State University [54]

The difference in the high temperature region shows that there can be some physical effect ignored in the model that cannot be neglected at high temperature. As the large difference only happens at high temperature (high oxygen gas consumption), one possible reason is that the supply of oxygen gas is not abundant for the electrochemical reactions to take place, and the diffusion of oxygen gas in experiment is weaker than it is assumed by the 3D model.

To investigate the effect of the oxygen gas diffusion, we calculate the cathode resistance using a low diffusivity $\sigma_g = 5 \times 10^{-6} \text{ m}^2/\text{sec}$, which is about 5% of the data $\sigma_g = 1.13 \times 10^{-4} \text{ m}^2/\text{sec}$ used in

Fig. 3.6. As shown in Fig. 3.7, using the reduced diffusivity value, the maximum difference between the simulated cathode resistance and the experimental data is less than 12%, which is much smaller compared to the 50% maximum in Fig. 3.6. This suggests that the diffusivity used in the 3D model should be smaller than the values shown in Table 3.3. That is because the gas diffusion in nano-scale pores works differently from the diffusion in a large room. The diffusivity shown in Table 3.3 only works in the case that the size of the pores is much larger than the mean free path of the motion of the gas molecules. However, in the cathode microstructure, the size of the pores is comparable to the mean free path, which normally has a dimension of 100nm, so the pores block the gas diffusion and make the effective diffusivity smaller.

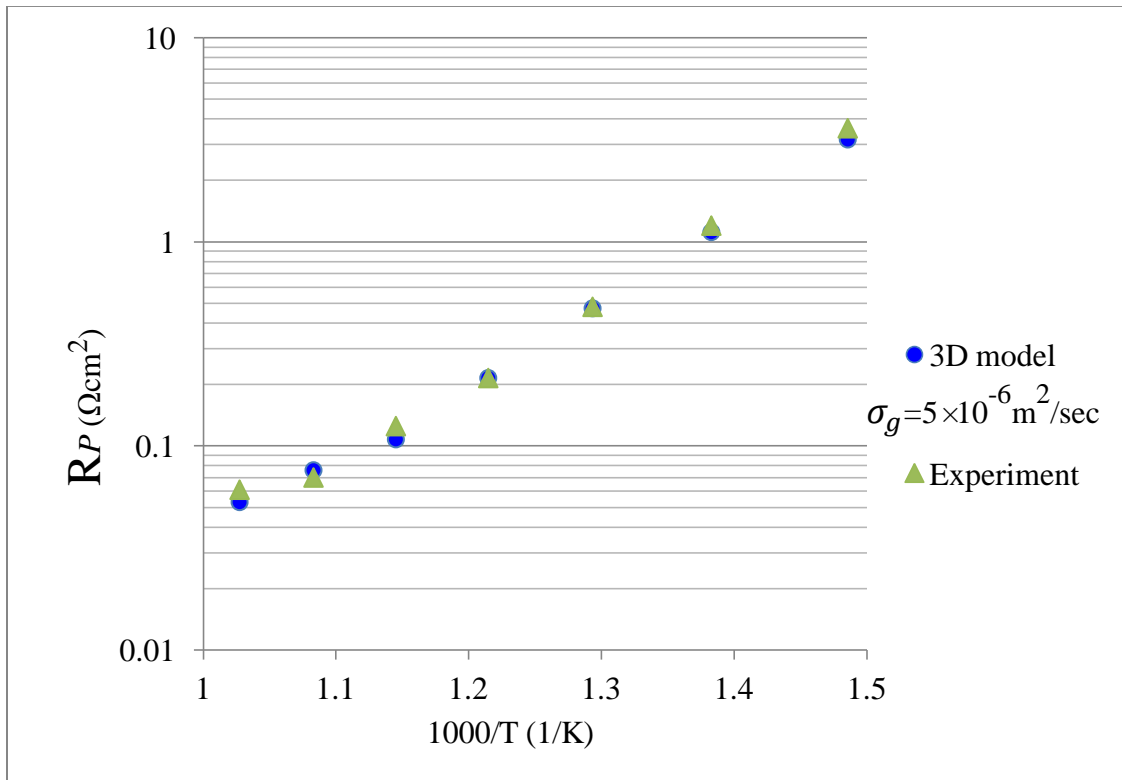


Figure 3.7 The comparison of R_P data for 20nm LSCF particles with a small oxygen gas diffusivity. Experimental data courtesy of Prof. Nicholas's group in Michigan State University [54]

3.6 Other examples

Here a simulation is performed using a very high oxygen gas diffusivity $\sigma_g = 1 \text{ m}^2/\text{sec}$, about 10000 times larger than the data $\sigma_g = 1.13 \times 10^{-4} \text{ m}^2/\text{sec}$ used in Fig. 3.6. By using a very high diffusivity, the gas supply becomes abundant, and the effect of oxygen gas diffusion is removed. Results are shown in Fig. 3.8. The cathode resistances with high diffusivity ($\sigma_g = 1 \text{ m}^2/\text{sec}$) are smaller than the cathode resistances for $\sigma_g = 1.13 \times 10^{-4} \text{ m}^2/\text{sec}$. However, the small gap between the two series in Fig. 3.8 shows the effect of oxygen gas diffusion is not strong for diffusivity values in the range shown in Table 3.3.

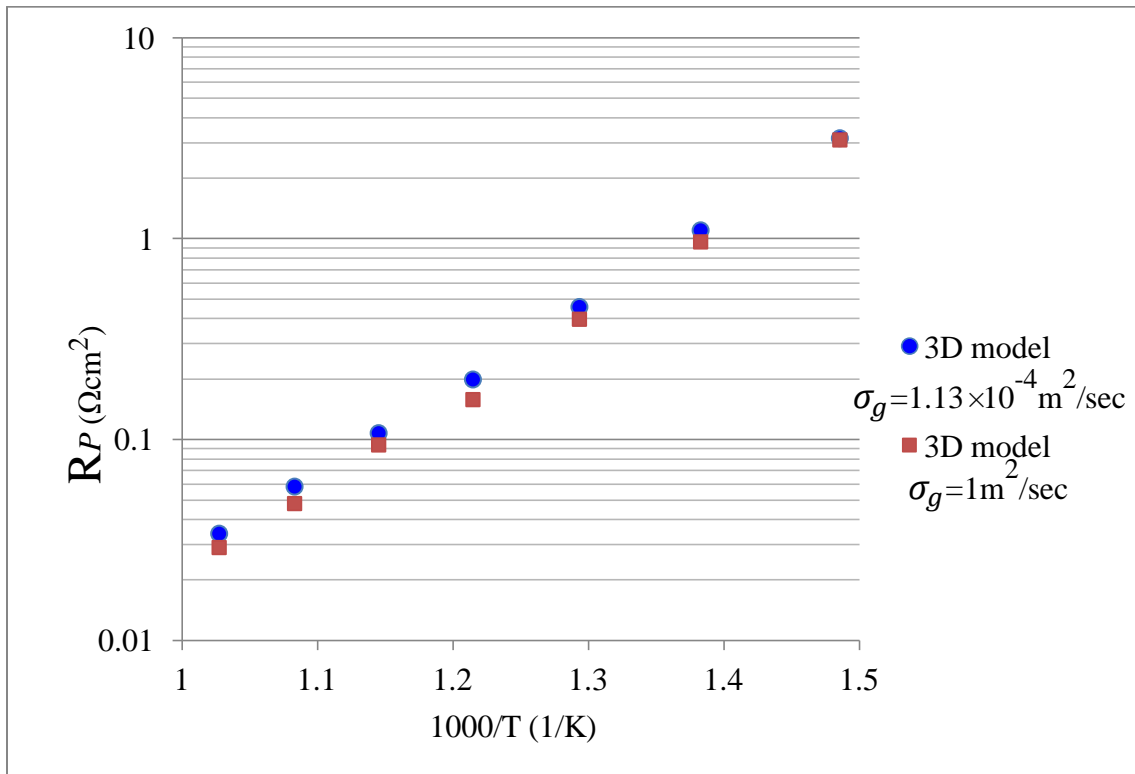


Figure 3.8 The comparison of R_P data for 20nm LSCF particles with a very large oxygen gas diffusivity

The last example in this section compares the simulation results of the 3D model to the 2D

simple reference model in chapter 2. The comparison is shown in Fig. 3.9. The cathode resistances are calculated using the diffusivity $\sigma_g=1.13\times 10^{-4} \text{ m}^2/\text{sec}$. The two series of cathode resistance are close to each other, and at most temperatures the resistance of the 3D model is larger than the resistance predicted by the 2D reference model. The small differences between the two series of results happen because the scaffold material we use has a large conductivity and the effect of scaffold resistance is not very remarkable. For other scaffold materials with lower conductivity, the difference between the cathode resistance calculated by the 3D model and the cathode resistance from the 2D model will be larger, and one can expect that the cathode resistance calculated by the 3D model will be much higher than the cathode resistance from the 2D reference model.

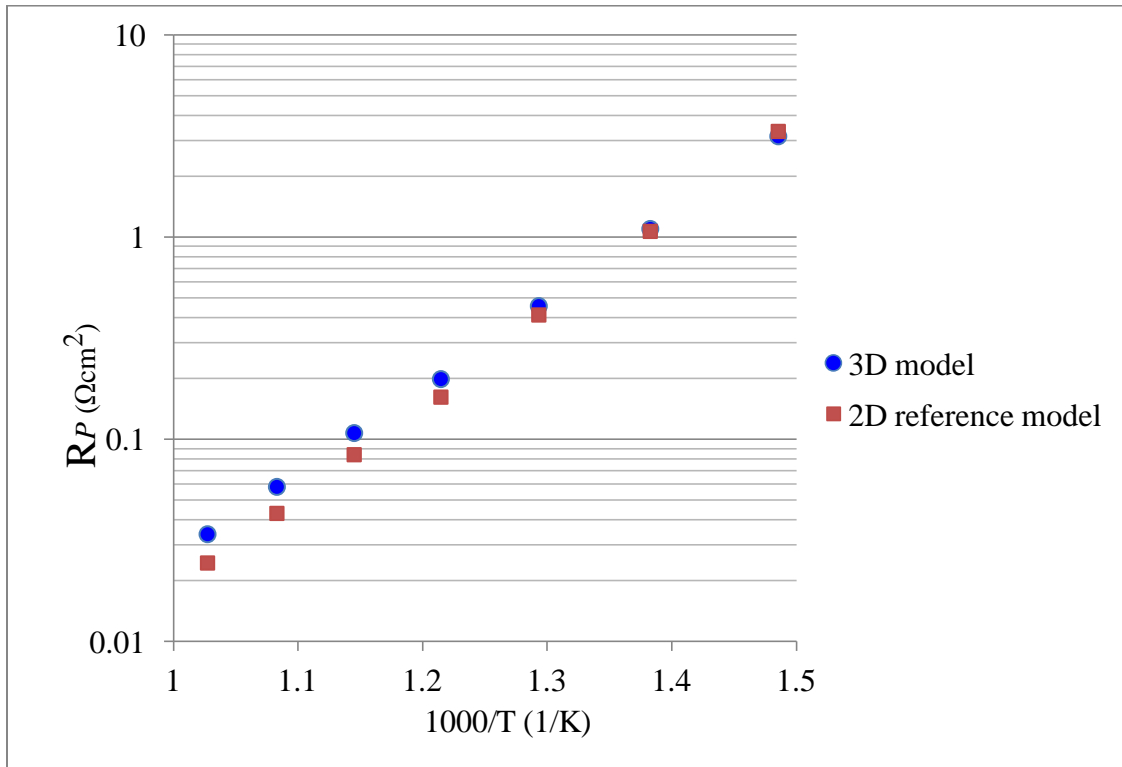


Figure 3.9 The comparison of R_P data obtained from different methods for 20nm LSCF particles

3.7 Conclusions

The cathode resistance calculated by the 3D finite element model decreases rapidly as the temperature increases, but higher temperatures are difficult to accommodate in industrial applications. The comparison between the simulation results and the experimentally measured results shows a small difference (<5%) at low temperature region, but the difference becomes large (50%) at high temperatures. The large difference comes from the reduction of oxygen gas diffusivity flowing through nano-scale pores. The difference can be reduced using smaller oxygen gas diffusivity in the 3D finite element model. The accuracy of the 3D finite element model at low temperature is higher than the simple model used in chapter 2, so the 3D finite element model provides a better foundation for the topology optimization model of the microstructure in the next chapter.

Chapter 4 Topology optimization for 3D cathode microstructure of solid oxide fuel cell cathodes

The optimal designs of 2D cathode microstructures obtained in chapter 2 qualitatively show the effect of the material properties and the geometric factors on the optimal feature and the performance. However, the 3D microstructure can have more complicated 3D connections than between different cathode scaffold parts than the 2D model and this can change the bulk resistance of the scaffold, and also the effect of oxygen gas consumption is not considered.

In this chapter, a 3D topology optimization model is set up to design the 3D microstructure of the SOFC cathode. The simulation is performed based on the finite element model introduced in chapter 3. The optimization problem is setup in a similar manner as the design problem of 2D cathode microstructure in chapter 2. The ionic conducting material is distributed in a 3D design domain to form a 3D cathode scaffold, and the MIEC is treated as a design-dependent boundary condition of the scaffold. The topology of the scaffold is optimized to minimize the cathode resistance/maximize the current generation.

4.1 Problem Setup

The 3D finite element model of the SOFC cathode has been established and validated in chapter 3. In preparation for topology optimization, the analysis sub domains for both the current in cathode and the gas diffusion in the pores were extended to the whole analysis domain Ω , and Ω

was discretized by uniform rectangular elements. The boundary of the scaffold Γ_ω was assigned to be along the element boundaries.

By assigning a design variable ρ to each element within the analysis domain Ω , the distribution of ionic conducting material can be represented by ρ , and the design can be changed by modifying ρ .

The 3D design domain is selected to be a sub domain of the analysis domain Ω , as shown in Fig. 4.1. The analysis domain Ω is a representative cell in a SOFC cathode microstructure. The height of the representative cell is the same as the cathode thickness (z - direction), and the cathode is composed by a series of periodic cells in x - and y - directions. As in the 2D case in section 2.6, a fixed region is assigned at the bottom of the analysis domain, and in this region the geometry cathode and gas sub-domains are pre-assigned, i.e. the geometry is fixed artificially to show the effect of the cathode root patterns from which the cathode microstructure grows. In contrast with the 2D case, the cathode scaffold is permitted to touch the side boundaries of the analysis domain, because the 3D structure and the gas pores can have off-plane connections.

The optimization problem is setup as follows. The objective of the problem is to find a 3D distribution of the ionic conducting material described by the design variable ρ of the elements with the design domain shown in Fig. 4.1, to minimize the cathode resistance (maximize current generation). The current flow is measured at the bottom boundary of the design domain. The detailed finite element formulation is described in chapter 3.

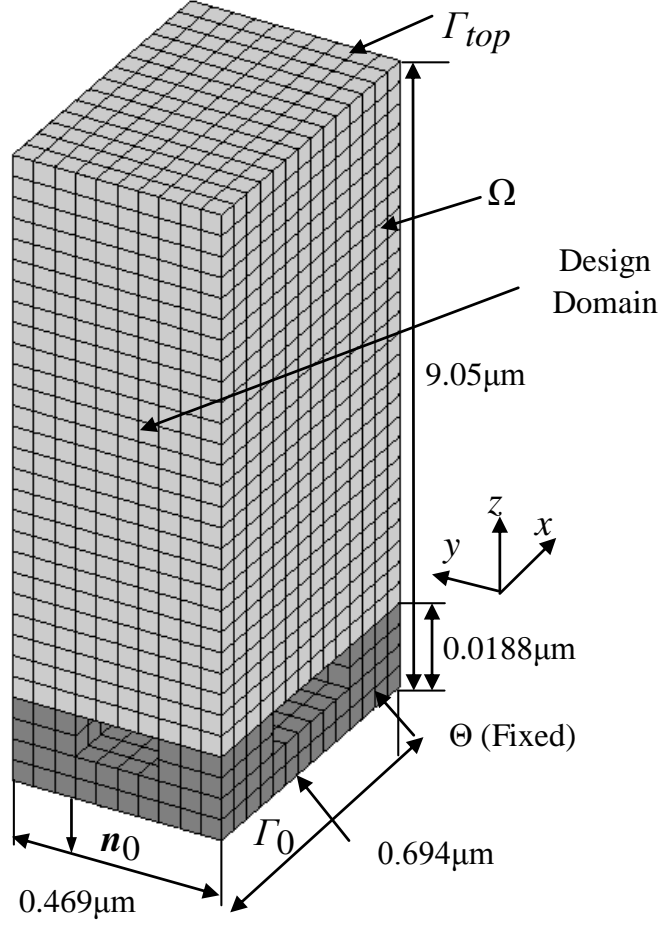


Figure 4.1 The design domain of the 3D microstructure problem

4.2 Material model

As introduced in chapter 3, the discretized forms of the governing equations are

$$\sum_e \int_{\Omega_e} \nabla \bar{\phi} \cdot (\sigma_e \nabla \phi) dV - \sum_e \int_{\Gamma_\omega} \bar{\phi} h_0 (\phi_\infty - \phi) c_{O_2} dA = 0$$

$$\forall \bar{\phi} \in V_\Omega^0 \quad (4.1)$$

$$\sum_e \int_{\Omega_e} \nabla \bar{c}_{O_2} \cdot (\sigma_g \nabla c_{O_2}) dV - \sum_e \int_{\Gamma_\omega} \bar{c}_{O_2} \left(-\frac{h_0}{z q_e n_0} (\phi_\infty - \phi) c_{O_2} \right) dA = 0$$

$$\forall \bar{c}_{O_2} \in V_{\Omega,g}^0 \quad (4.2)$$

where Γ_ω is assigned to be along the element boundaries.

In the same manner as in chapter 2, a SIMP like approach is used to extend the binary material properties to a continuous function of the design variable, let $\rho: \Omega \rightarrow [0, 1]$ be also piece-wise constant in Ω with values ρ_e within element e , and express the conductivity σ_e as

$$\sigma_e = \sigma_0 \rho_e^p + \sigma_\epsilon (1 - \rho_e^p) \quad (4.3)$$

$$\sigma_e^g = \sigma_0^g (1 - \rho_e^p) + \sigma_e^g \rho_e^p \quad (4.4)$$

where p is the penalty factor in the SIMP model.

In addition, a design dependent (inverse) surface resistance coefficient $h_{\partial e}$ is introduced to replace h_0 to show the change in design.

$$\sum_e \int_{\Omega_e} \nabla \bar{\phi} \cdot (\sigma_e \nabla \phi) dV - \sum_e \int_{\partial e \cup \Gamma_\omega} \bar{\phi} h_{\partial e} (\phi_\infty - \phi) c_{O_2} dA = 0$$

$$\forall \bar{\phi} \in V_\Omega^0 \quad (4.5)$$

$$\sum_e \int_{\Omega_e} \nabla \bar{c}_{O_2} \cdot (\sigma_g \nabla c_{O_2}) dV - \sum_e \int_{\partial e \cup \Gamma_\omega} \bar{c}_{O_2} \left(-\frac{h_{\partial e}}{zq_e n_0} (\phi_\infty - \phi) c_{O_2} \right) dA = 0$$

$$\forall \bar{c}_{O_2} \in V_\Omega^0 \quad (4.6)$$

In the method introduced in chapter 2, a penalized model can be used to describe the (inverse) surface resistance coefficient $h_{\partial e}$

$$h_{\partial e}^j = \frac{h_0}{2} \left(\sqrt{(\rho_e - \rho_e^j)^2 + \epsilon^2} - \epsilon \right) / (\sqrt{1 + \epsilon^2} - \epsilon) \quad (4.7)$$

where ρ_e^j and $h_{\partial e}^j$ represent, respectively, the density and the (inverse) surface resistance coefficient across the j -th face of element e ($j = 1, 2, 3, 4, 5, 6$), as illustrated in Fig. 4.2.

$h_{\partial e}^j = 0$ if there is no change in material properties across the j -th side of element e .

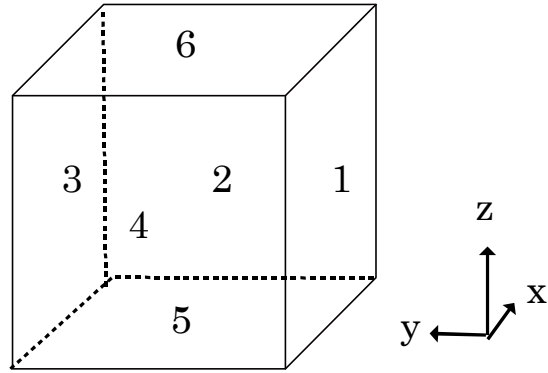


Figure 4.2 The arrangement of the element face number

Note from EQ. 4.7, the penalty is used to resolve the non-differentiability problem of $|\rho_e - \rho_e^j|$ at $\rho_e - \rho_e^j = 0$. By using the penalty, $h_{\partial e}^j$ becomes differentiable and $\partial h_{\partial e}^j / \partial \rho_e = 0$ at $\rho_e - \rho_e^j = 0$ if $0 < \epsilon \ll 1$, e.g., $\epsilon = 0.001$.

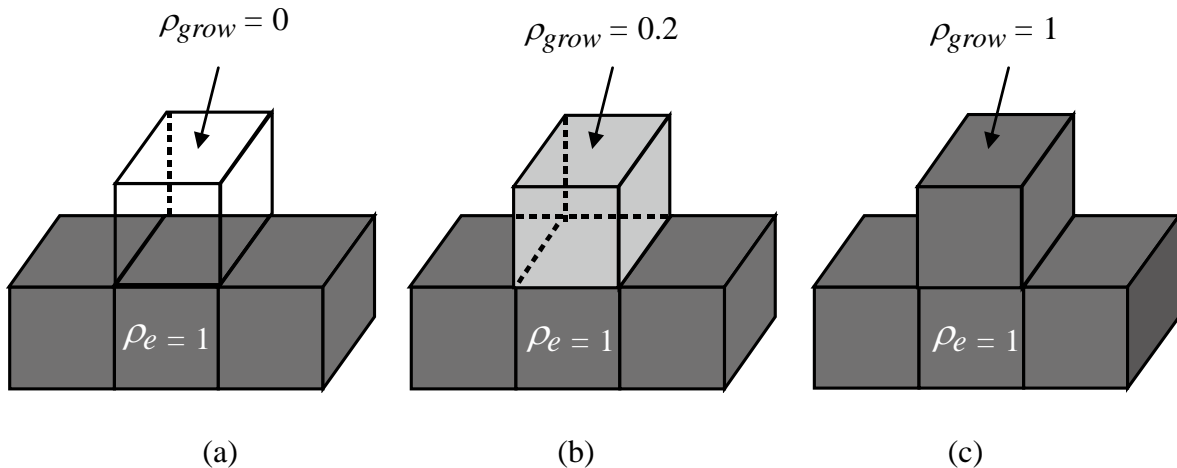


Figure 4.3 Penalty in the surface resistance model may make design (b) performs worse than (a) and (c)

Further investigation shows that the use of EQ. 4.7 may accept local optima and prevent the design from improving, which is similar with the local minimum problem discussed in section 2.8. To illustrate, consider the three designs in Fig. 4.3. Design (c) has a larger surface area than design (a) and should be the preferred solution. A change from (a) to (c) requires increasing

ρ_{grow} slightly, as shown in design (b). However, if ρ_{grow} within the gap is increased only slightly, design (b) may actually generate less current than either (a) or (c). This is because the increase in the surface area of the scaffold may be canceled by a simultaneous reduction the (inverse) surface resistance coefficient. If this were to happen, the gradient of the objective function with respect to ρ_{grow} will be positive and the design will never grow. To avoid this, a modification of the material model base on both of the first and the second order derivative of $\rho_e - \rho_e^j$ is employed.

The idea is to use the value of the second order derivative to determine the trend of the change in the first order derivative. The second derivative of $\rho_e - \rho_e^j$ is defined as

$$\frac{d^2(\rho_e - \rho_e^j)}{dx^2} = (\rho_e - \rho_e^{j=2}) - (\rho_e - \rho_e^{j=4}) \quad (4.8)$$

$$\frac{d^2(\rho_e - \rho_e^j)}{dy^2} = (\rho_e - \rho_e^{j=3}) - (\rho_e - \rho_e^{j=1}) \quad (4.9)$$

$$\frac{d^2(\rho_e - \rho_e^j)}{dz^2} = (\rho_e - \rho_e^{j=6}) - (\rho_e - \rho_e^{j=5}) \quad (4.10)$$

Even if $\rho_e - \rho_e^j = 0$, when the corresponding second derivatives are not zero, as shown in Fig. 4.4, if the second derivative has a non-zero value, the trend of change of $|\rho_e - \rho_e^j|$ can be determined. In this case, the penalty can be removed and design (b) can perform better than (a). To avoid the influence of small perturbation of the second derivative, the penalty in EQ. 4.7 is only removed when the absolute value of the corresponding second derivative is greater that 0.1.

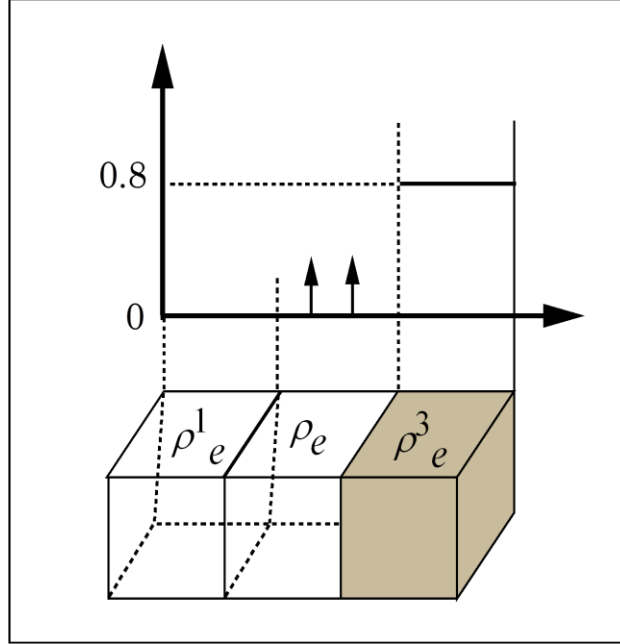


Figure 4.4 The second derivative can determine the trend of the first derivative

4.3 Constraints

In the SOFC experimental work, porosity is one of the most common parameter that helps to describe the properties of the porous cathode microstructure. A smaller porosity means more ionic conducting material in the microstructure, and that usually leads to a decrease in scaffold resistance. To make a fair comparison that shows that the improvement only comes from the design of the geometry pattern, a minimum porosity is assigned to the design.

The porosity $vol\%$ can be computed by the density distribution.

$$vol\% = \left(1 - \frac{W}{W_{\Omega}}\right) \times 100\% \quad (4.11)$$

where

$$W = \sum e \rho_e V_e \quad (4.12)$$

$$W_{\Omega} = \sum e V_e \quad (4.13)$$

The minimum porosity is selected to be 49.15%, which is the same as the porosity of the 9 microns thick cathode example.

4.4 Optimization Problem

Using the cathode resistance calculated by EQ. 3.14 as the objective function and the constraints in EQ. 4.11, the optimization problem is:

Find $\rho \in \Theta$ that

Minimize

$$R_p = \frac{\Phi_\infty}{\frac{1}{A} \int_{\Gamma_0} (\sigma_e \nabla \phi) \cdot \mathbf{n}_0 dA} \quad (4.14)$$

Subject to

$$\begin{aligned} \text{porosity} &\geq \text{porosity}_{min} \\ 0 \leq \rho_e &\leq 1, \quad e = 1, 2, 3, \dots, N \end{aligned} \quad (4.15)$$

and (discretized) state equations, discussed in section 4.5 below. In this problem Porosity_{min} is prescribed lower bounds on the porosity. The set Θ is used simply to define regions Ω_0 and Ω_1 where the conducting material is prescribed.

Specifically,

$$\Theta := \{\rho \in [0, 1]^N : \rho_e = 0 \text{ if } e \in \Omega_0, \rho_e = 1 \text{ if } e \in \Omega_1\} \quad (4.16)$$

In EQ. 4.16 Ω_0 and Ω_1 are subsets of Ω where ρ is prescribed to have value 0 (gas) or 1 (scaffold or electrolyte), respectively.

In the manner of section 2.7, a density filter with a linear weight is used to prevent the appearance of checkerboard patterns and to control feature size. A smoothed Heaviside projection function is used to facilitate convergence to binary solutions.

4.5 Sensitivity Analysis

Upon assembly of element matrices, EQ. 4.5 and EQ. 4.6 becomes

$$(\mathbf{K}_\sigma + \mathbf{H}_h)\Phi = \mathbf{q}_h \quad (4.17)$$

$$\mathbf{K}_g \mathbf{c}_{O_2} + \mathbf{H}_g \Phi = \mathbf{q}_g \quad (4.18)$$

where Φ is the vector of values of the potential ϕ , and \mathbf{c}_{O_2} is the vector of values of the oxygen gas concentration at the nodes. Matrices \mathbf{K}_σ , \mathbf{H}_h , \mathbf{K}_g , \mathbf{H}_h^g and vector \mathbf{q}_h , \mathbf{q}_h^g are assembled from element-level quantities

$$\mathbf{K}_\sigma^e = \int_e \sigma_e \nabla N_e \nabla N_e^T dA \quad (4.19)$$

$$\mathbf{H}_h^e = \int_{\partial e} h_{\partial e} c_{O_2} N_e N_e^T dl \quad (4.20)$$

$$\mathbf{K}_g^e = \int_e \sigma_g \nabla N_e \nabla N_e^T dA \quad (4.21)$$

$$\mathbf{H}_g^e = \int_{\partial e} \frac{h_{\partial e}}{z q_e n_0} c_{O_2} N_e N_e^T dl \quad (4.22)$$

$$\mathbf{q}_h^e = \phi_\infty \int_{\partial e} h_{\partial e} N_e dl \quad (4.23)$$

$$\mathbf{q}_g^e = \phi_\infty \int_{\partial e} \frac{h_{\partial e}}{z q_e n_0} c_{O_2} N_e dl \quad (4.24)$$

where N_e represents the vector of shape functions of element e .

Upon discretization, the objective function EQ. 4.14 becomes

$$R_P = \frac{\phi_\infty}{\mathbf{p}_f^T \Phi} \quad (4.25)$$

where \mathbf{p}_f is assembled from

$$\mathbf{p}_f^T = -\sigma_0 \int_{\partial e \cap \Gamma_0} \nabla N_e \cdot \mathbf{n}_0 dl \quad (4.26)$$

The sensitivity of R_P is obtained from

$$\frac{\partial R_P}{\partial \rho_e} = -\frac{R_P}{\mathbf{p}_f^T \Phi} \left(\hat{\Phi} \right)^T \left(-\frac{\partial \begin{pmatrix} \mathbf{K}_\sigma + \mathbf{H}_h & 0 \\ \mathbf{H}_g & \mathbf{K}_g \end{pmatrix}}{\partial \rho_e} \begin{pmatrix} \Phi \\ c_{O_2} \end{pmatrix} + \frac{\partial \begin{pmatrix} \mathbf{q}_h \\ \mathbf{q}_g \end{pmatrix}}{\partial \rho_e} \right) \quad (4.27)$$

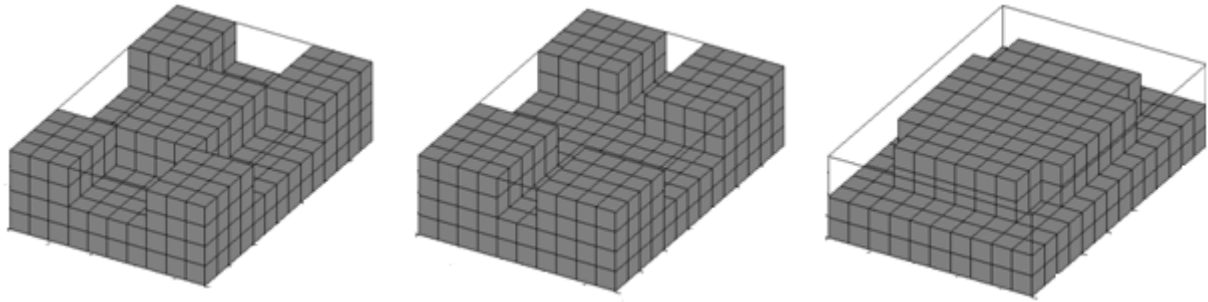
where $\begin{pmatrix} \hat{\Phi} \\ \hat{c}_{O_2} \end{pmatrix}$ is the solution of the adjoint problem

$$\begin{pmatrix} \mathbf{K}_{\sigma} + \mathbf{H}_h & \frac{\partial(\mathbf{H}_h \Phi)}{\partial c_{O_2}} + \frac{\partial \mathbf{q}_h}{\partial c_{O_2}} \\ \mathbf{H}_g & \mathbf{K}_g + \frac{\partial(\mathbf{H}_g \Phi)}{\partial c_{O_2}} + \frac{\partial \mathbf{q}_g}{\partial c_{O_2}} \end{pmatrix} \begin{pmatrix} \hat{\Phi} \\ \hat{c}_{O_2} \end{pmatrix} = \begin{pmatrix} \mathbf{p}_f \\ \mathbf{0} \end{pmatrix} \quad (4.28)$$

4.6 Numerical Examples

In the following examples we investigate the influence of changes in material properties and the arrangement of cathode roots. In the examples, the element size in the finite element mesh is the same as the element size extracted from experimental data in section 3.3, and the height of the whole mesh is also the same as the example corresponding to 20nm diameter LSCF particles in section 3.3. To reduce the computational cost, the length and width of the analysis domain are both half of the analysis domain used in chapter 3, as shown in Fig. 4.1. Since infiltration typically produces MIEC nanoparticles 20–50 nm in diameter, the smallest feature size that can be modeled before the assumption that the MIEC is uniformly spread over the scaffold is violated may be of the order of 200 nm.

As introduced in section 4.1, the design domain is set up upon some fixed root. Three arrangements of the roots are selected as shown in Fig. 4.5. The arrangements have five, four and one roots, respectively, but the total footprints (area) are the same. The foot prints of the arrangements all are 50% of the bottom boundary Γ_0 , and the ratio is consistent with the 3D reconstructed microstructure in chapter 3.



(a) Five roots

(b) Four roots

(c) Single root

Figure 4.5 The arrangements of the fixed roots

All optimization problems are solved using the method of moving asymptotes of Svanberg [50]. Different from the 2D designs in Chapter 2, the 3D design is not forced to be symmetric to permit more complicated designs to be generated. Results reported are after post-processing, applying a threshold at $\rho = 0.5$ to remove the intermediate density elements left in the optimal solutions.

To save time and resources, the width and length of the design domain are selected to be half of the size of the analysis domain used in Chapter 3. To make sure the design domain is large enough to be used as a periodic cell in the cathode microstructure, the cathode resistance at 400°C are calculated using the whole reconstructed microstructure in Sec. 3.3 and a quarter of the microstructure with half the width and length (shown in Fig. 4.6). The cathode resistances are $3.17\Omega\times\text{cm}^2$ and $3.23\Omega\times\text{cm}^2$, which are very close. The good consistency validates the selection of the size of the design domain.

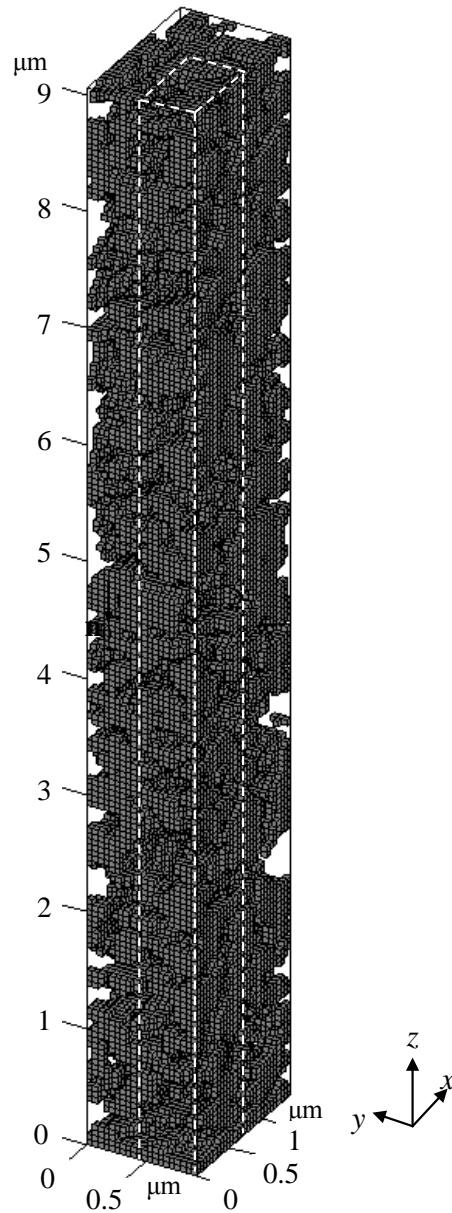


Figure 4.6 The comparison between the analysis domain in Chapter 3 and the design domain in Chapter 4 (in white rectangle)

4.6.1 Designs with varying the material properties by changing work temperature

In this example the porosity constraint bounds is set to $voP\%_{min}=49.15\%$. The root arrangement in Fig. 4.5(a) is used in this example. Fig. 4.7 and Table 4.1 illustrate the effect of varying work temperature on the optimal solution. The material properties σ_0 and R_S are

determined by the work temperature, and higher temperature is associated with higher performance ionic conducting and electrocatalyst materials. The oxygen gas diffusivity $\sigma_0=1.13 \times 10^{-4} \text{ m}^2/\text{sec}$ at 600°C is used for all the design examples.

Table 4.1 Performance of optimized design at different temperatures (Fig. 4.7-4.8)

Temp ($^\circ\text{C}$)	Bulk Conductivity σ_e (S/cm)	$R_S(\Omega \times \text{cm}^2)$	$1/$ $(R_S \times \sigma_e)$	Optimized R_P $(\Omega \times \text{cm}^2)$	Reference R_P $(\Omega \times \text{cm}^2)$	Improvement (%)
400	1.76×10^{-3}	229.651	0.99	2.51	3.16	21
450	3.69×10^{-3}	70.044	1.55	0.836	1.10	24
500	6.90×10^{-3}	25.262	2.30	0.336	0.457	27
550	1.14×10^{-2}	8.727	4.02	0.14	0.199	30
600	1.77×10^{-2}	4.134	5.47	0.0733	0.1076	32
650	2.67×10^{-2}	1.837	8.16	0.0385	0.0583	34
700	3.86×10^{-2}	0.919	11.3	0.0222	0.034	35

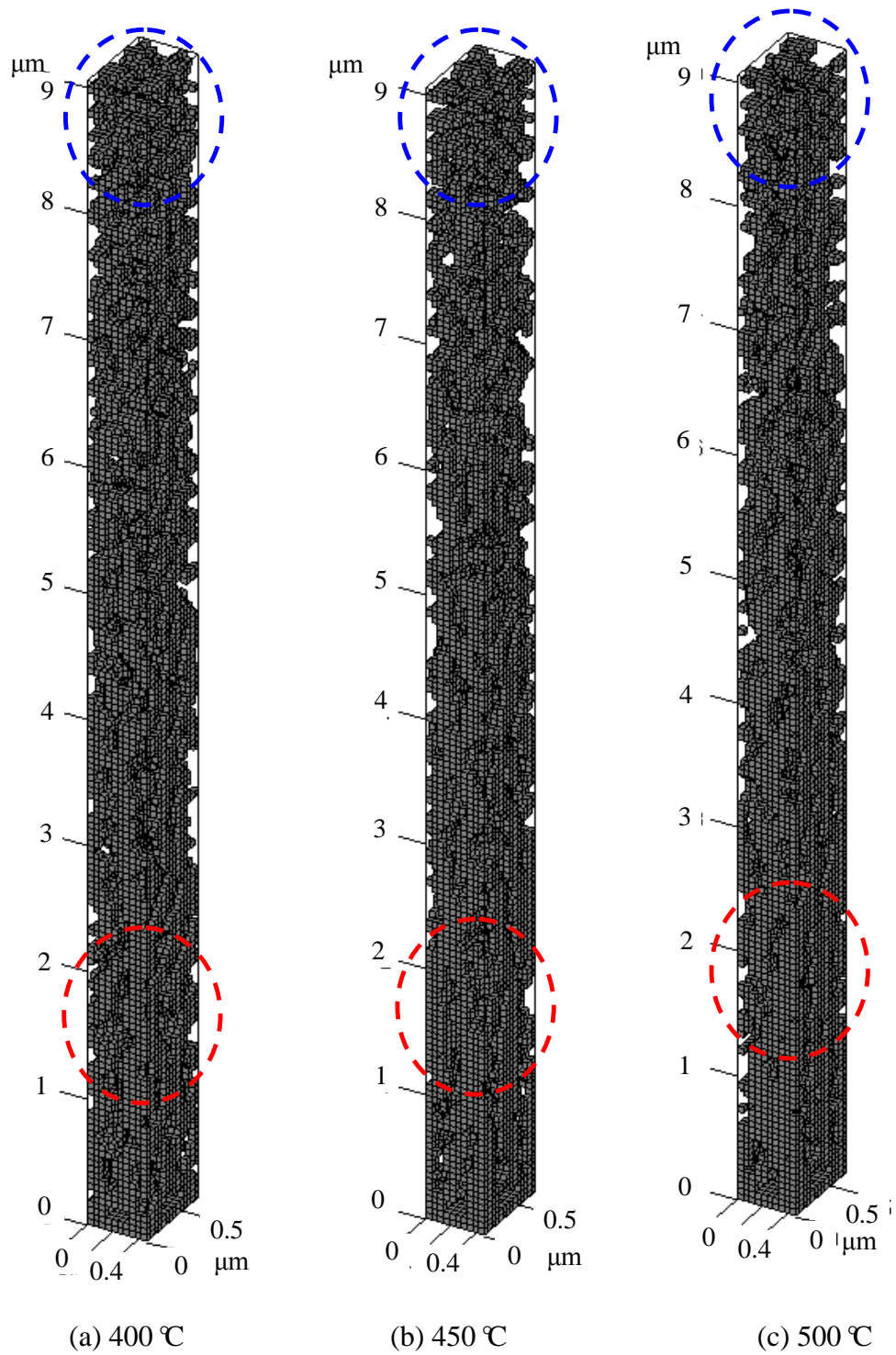
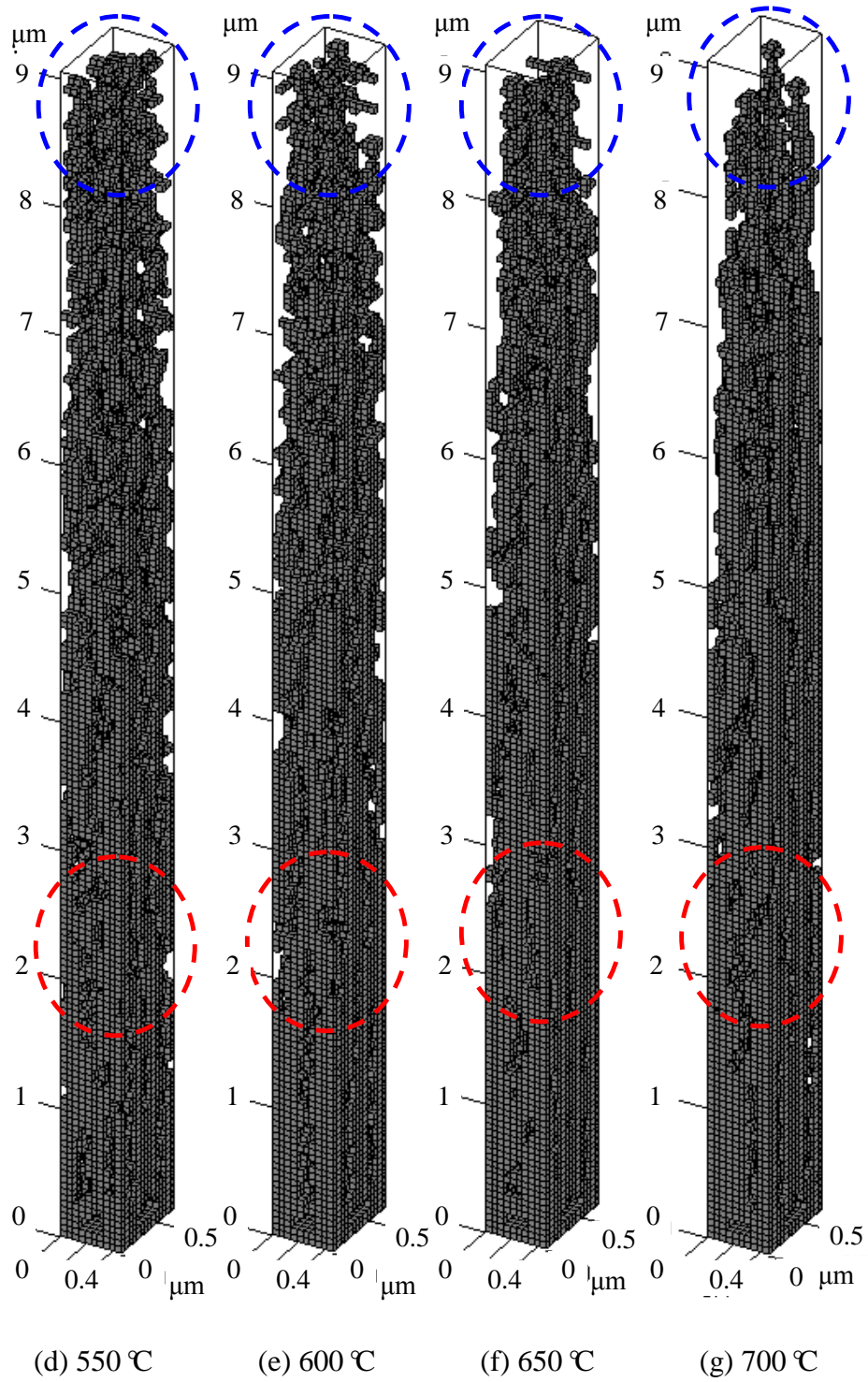


Figure 4.7 The optimized design at different work temperatures. Performance is reported in Table 5.1

Figure 4.7 (cont'd)



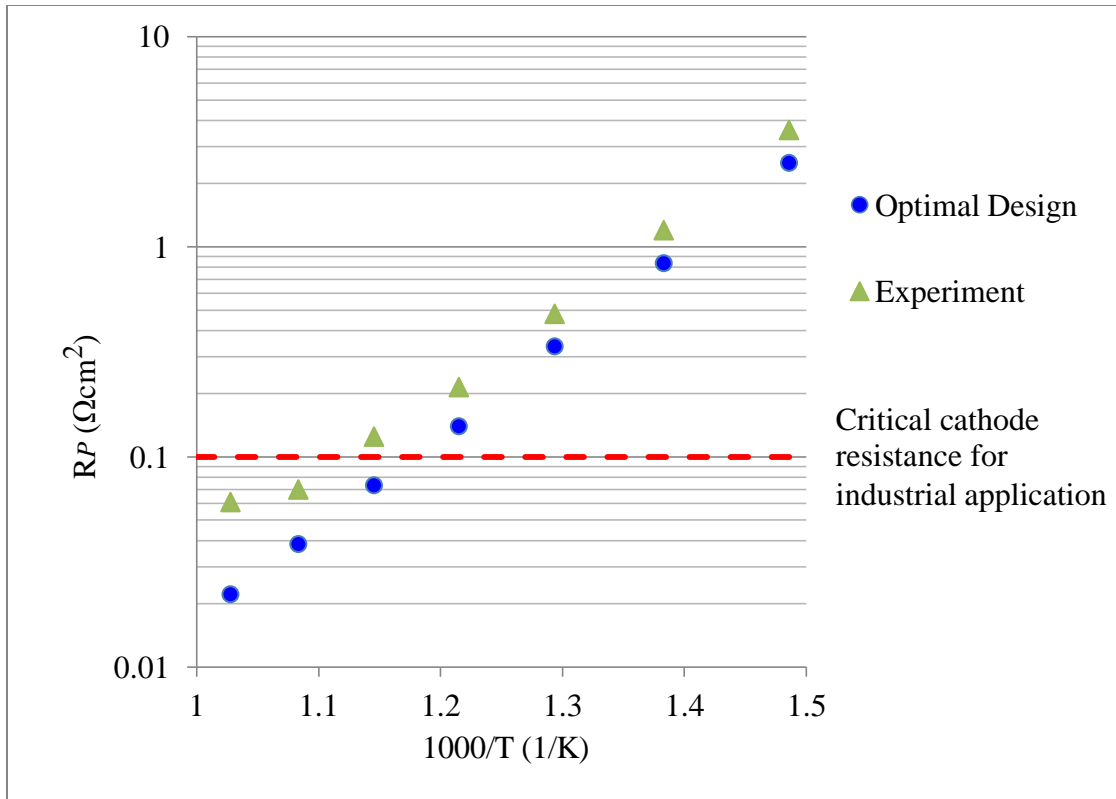


Figure 4.8 The comparison of R_P data for 20nm LSCF particles with a small oxygen gas diffusivity. Experimental data courtesy of Prof. Nicholas's group in Michigan State University [54]

As shown in Fig. 4.8 and Table 4.1, the optimal results have remarkable improvement compared with experimental data. Because the large difference between the simulation model and experimental data (shown in Chapter 3) at high temperature region, the optimal designs in high temperature range is not reliable, but the designs make also improvement in low temperature range. The lower optimal cathode resistances are closer to the critical value $0.1\Omega\text{cm}^2$ for industrial application.

The ratio $1/(R_S\sigma_e)$ [55] shown in Table 4.1 has a similar effect with the ration h_0/σ_0 used in chapter 2, and the increase of $1/(R_S\sigma_e)$ with the increase of the work temperature shows the

improvement of the MIEC performance outweighs the improvement of the bulk conductivity.

In the solutions shown in Fig. 4.7, (a)-(c), the ratio $1/(R_S\sigma_e)$ is smaller, surface resistance dominates scaffold resistance and therefore the optimized designs tend to have thinner current paths through the scaffold (shown in red circles in Fig. 4.7 (a)-(c)) and span the whole design domain to form smaller features and larger surface areas (shown in blue circles in Fig. 4.6 (a)-(c)). As the ratio $1/(R_S\sigma_e)$ increasing from 0.99 to 11.3, the electrocatalyst material is more effective, and the focus of the solutions shown in Fig. 4.7 (d)-(g) gradually shifts from the surface area to the body of the scaffold. The path of the current through the scaffold rather becomes more significant than the surface reactions, and the scaffold features become thicker to form a better current path (shown in red circles in Fig. 4.7 (d)-(g)). The increased flux through the boundary that results from the better material performances at high temperature calls for a well-designed path to the electrolyte at the bottom, and to achieve this the heights of the column in the design shown in Fig. 4.7 (d)-(g) become shorter than the height of the design domain to make thick columns from the same amount of material (shown in blue circles in Fig. 4.7 (d)-(g)).

Table 4.2 Tortuosity and surface areas of optimized design at different temperatures (Fig. 4.7)

Temp (°C)	Surface Area (cm ²)	Tortuosity
400	3.68×10^{-7}	1.48
450	3.61×10^{-7}	1.43
500	3.51×10^{-7}	1.41
550	3.30×10^{-7}	1.38
600	3.24×10^{-7}	1.35
650	3.06×10^{-7}	1.32
700	2.97×10^{-7}	1.28

Another parameter that can show the geometric feature of the cathode microstructure is the tortuosity, which measures twist of the cathode surface. In this chapter tortuosity is evaluated by

$$\tau = \frac{\sum_e A_{\Gamma\omega}^e}{\sum_e A_{\Gamma\omega}^{ez}} \quad (4.29)$$

where τ is tortuosity, $A_{\Gamma\omega}^e$ is the surface area of the cathode microstructure at the boundary of element e , and $A_{\Gamma\omega}^{ez}$ is the projection of the elemental surface area to the vertical z -direction (not including the part that parallel to x - y plane). The numerator of EQ. 4.29 measures the real paths from the top of the cathode to the bottom, and the denominator measures the ideal shortest paths (directly along z -direction) from the top to the bottom.

The reference tortuosity value of the reconstructed microstructure is 1.34, and the values of the tortuosity of the optimal microstructures are shown in Table 4.2. As the temperature decreases, the surface area of the tortuosity of the optimal design increases to make good use of the surface area and reduce the surface resistance of the cathode. However, at high temperatures, the tortuosity becomes smaller than the reference value, and the design focuses more on generating a thicker path to reduce the scaffold resistance.

4.6.2 Design with varying the arrangement of the cathode roots with constant footprint

In this example the designs with different root arrangements are discussed. All the three arrangements shown in Fig. 4.5 are used. Fig. 4.9-4.10 and Table 4.2 illustrate the effect of varying the arrangement while keeping the footprint as 50% $\text{Area}(\Gamma_0)$ on the optimal solution.

As shown in Table 4.3, R_p remains nearly constant for all the three arrangements. At a high work temperature (higher $1/(R_S\sigma_e)$), the optimized design for the five roots' arrangement begins

to perform slightly better than the single roots' arrangement. However, the arrangements of the roots show no significant influence to the cathode performance, and the improvements made by designing the cathode geometry remains the same (Table 4.4).

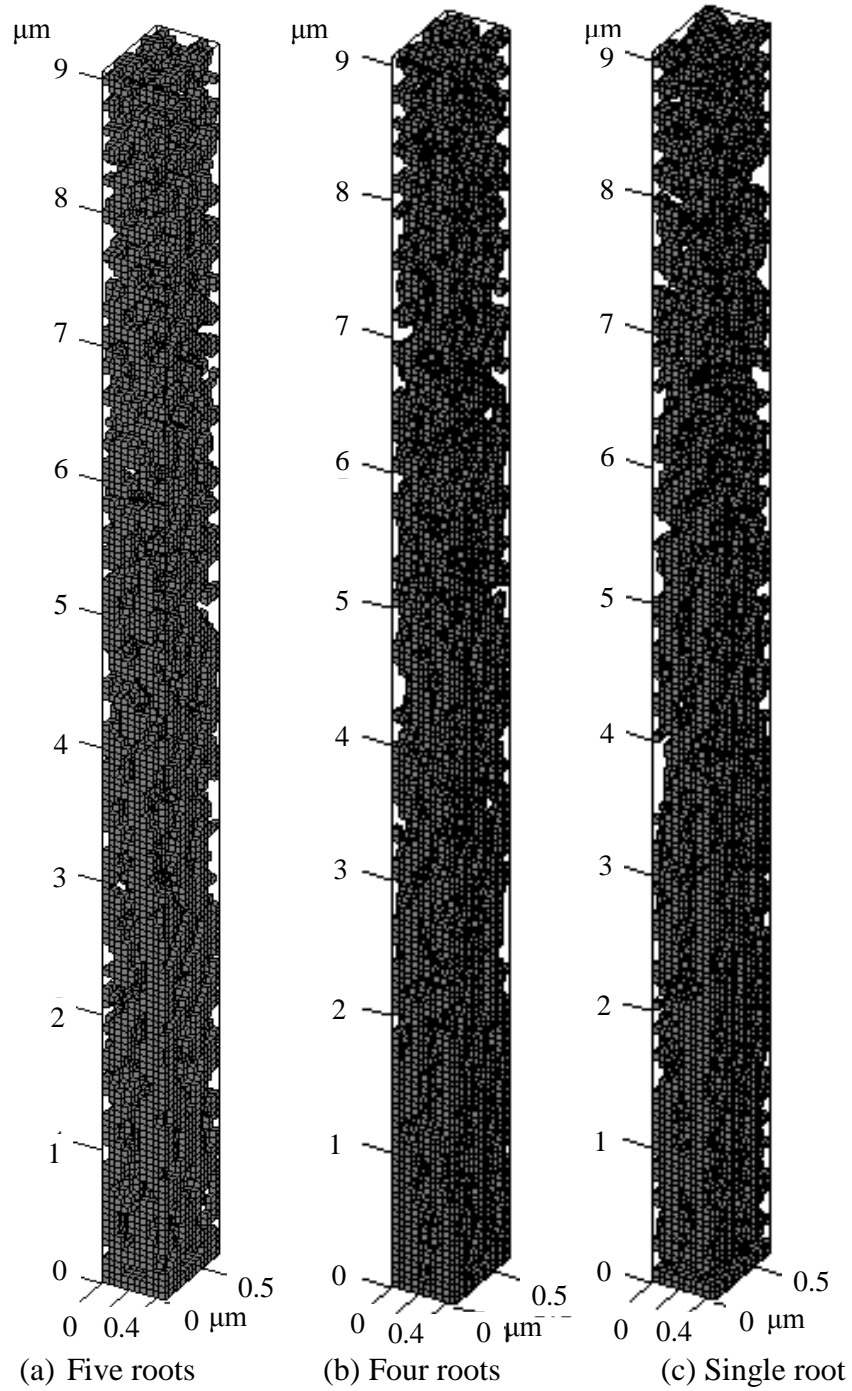
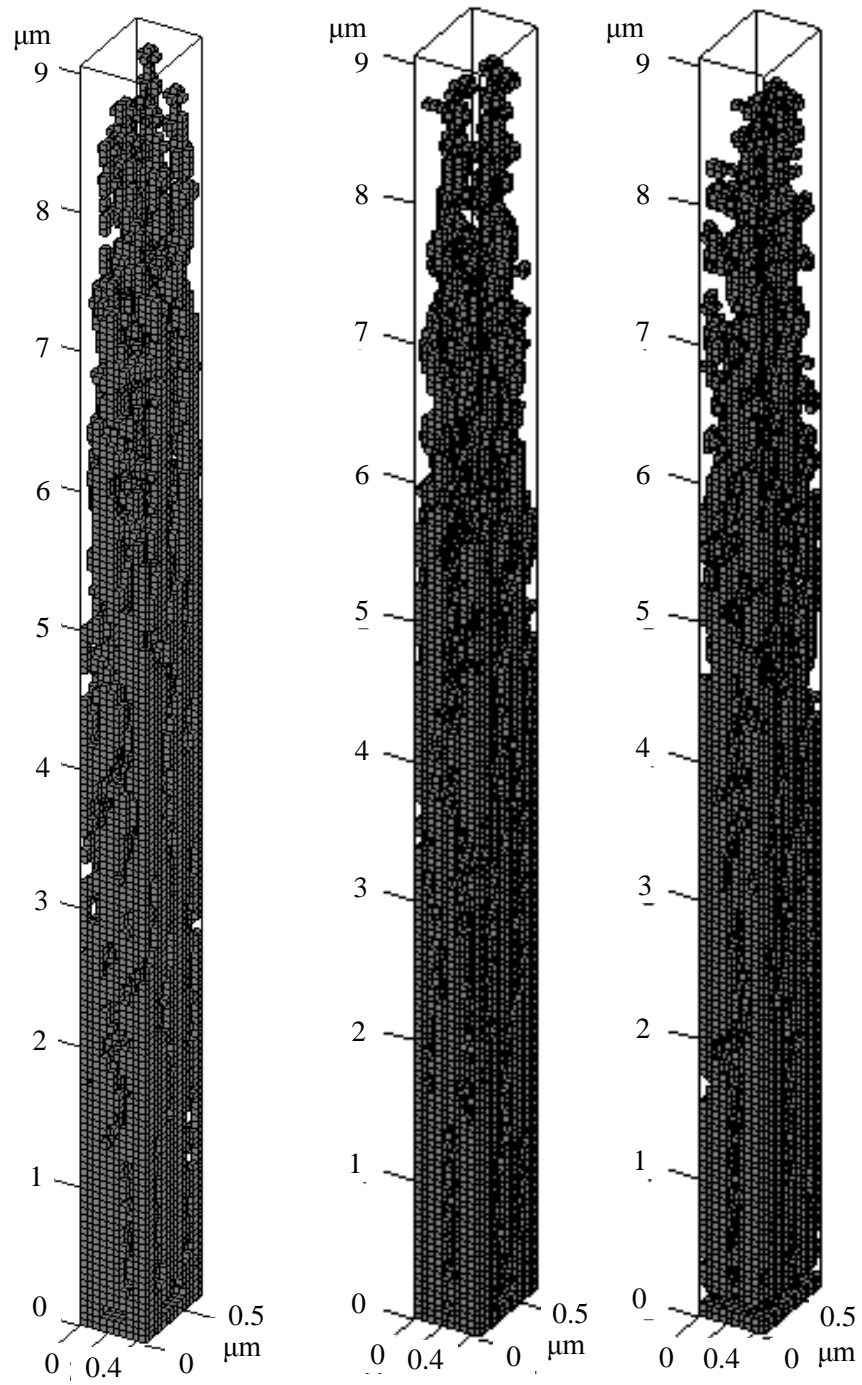


Figure 4.9 The optimized design for different root arrangements at 400 °C. Performance is reported in Table 4.3



(a) Five roots

(b) Four roots

(c) Single root

Figure 4.10 The optimized design for different root arrangements at 700 °C. Performance is reported in Table 4.3

Table 4.3 Performance of optimized design for different root arrangements (Fig. 4.9-4.10)

Temp (°C)	Rp for Five Roots ($\Omega \times \text{cm}^2$)	Rp for Four Roots ($\Omega \times \text{cm}^2$)	Rp for Single Root ($\Omega \times \text{cm}^2$)
400	2.50	2.51	2.49
700	0.0222	0.0223	0.0228

Table 4.4 Improvement of optimized design for different root arrangements compared to experimental data (Fig. 4.9-4.10)

Temp (°C)	Improvement for Five Roots	Improvement for Four Roots	Improvement for Single Root
400	20%	20%	20%
700	35%	35%	33%

4.7 Conclusions

While the 2D designs can only give schematic guidance on the characteristics of 3D optimal microstructures, the 3D design emphasizes in direct design of the intricate cathode microstructure, and from the 3D design examples one can extract the optimal feature for different work temperature. Improvements of 21-35 % were found, compared to the experimentally measured data of the current cathode sample. Because the scaffold components in the 3D designs are permitted to grow in all the directions, the branches of the 3D designs are able to form complicated connections between them and form porous microstructures different from the 2D tree-like design. For the designs at low operating temperatures, the surface resistance of LSCF coating outweighs the bulk resistance of CGO scaffold, so the optimal designs have larger surface areas and tortuosities to make the geometric features thinner and span the whole height of the design domain to generate a larger surface within a minimum porosity. As the temperature increases, the bulk resistance of CGO scaffold begins to perform a more significant role than the surface resistance of LSCF coating. Therefore, the optimal geometries has smaller surface areas

and tortuosities and prefers to distribute at a lower height to form a thicker ionic conducting path to the bottom, and the resulting cathode height can be smaller than the height of the design domain. The cathode root arrangement only has very little influence on the cathode performance.

Chapter 5 Thermal strength design for anode support structure of solid oxide fuel cell electrode

In this chapter, a finite element model for an anode-supported SOFC electrode is established in consideration of a coupled process of fuel supply, electrochemical reactions, heat transfer and structural deformation. The fuel flow in the channel with design-dependent geometry is modeled using a mixed formulation of steady-state Navier-Stokes equation and Darcy equation. The resulting velocity field is used as a known parameter in the calculation of the fuel transport. The fuel transport is described by the convection-diffusion equation. The current generation of the electrochemical reactions is calculated by the Butler-Volmer equation, and it is coupled with the fuel transport by a fuel consumption boundary condition. The heat is generated from the electrochemical reactions, and the heat exchange between the electrode and the flows results in a temperature gradient in the electrode. The temperature change results in a thermo-mechanical deformation of the electrode.

The porous media used in SOFC electrodes are brittle ceramic materials, and the porous microstructure is composed by randomly arranged ceramic particles. The random nature in the microstructures results in the randomness of their inherent flaws from manufacturing, so the ceramics exhibit a large spread of bulk failure strength. Therefore, the failure stress of these materials is not a well defined number, and a probabilistic metric, which is called the probability

of failure, is utilized to assess whether the material will fail at a given stress or not.

As the electrode is usually sintered at a higher temperature, tensile thermal stresses will be generated inside the electrode at the relatively lower work temperature. Experimental tests [57][58] show that thermal stress has a strong effect on the mechanical failure of the fuel cells. In the cases discussed in this chapter, the thermal stress is much higher than the stress caused by pressure load, and it is the dominate cause of mechanical failure.

The failure probability of a structure is the probability of a fast fracture of structure in the instant after a load is applied. The weakest link theory can be used to calculate the probability of failure of a structure. When the weakest link fails, the whole structure will fail, so the structural strength depends on the weakest link. Weibull [22] gave an expression of the probability of failure, and this expression has been validated in the prediction of the structural failure of the SOFC electrode [28][29]. In this chapter, this expression is adopted as the measure of the structural strength.

A topology optimization model is setup to design the macro-scale shape of the electrode and the fuel supply channel to optimize the thermal compliance and minimize the probability of failure.

Although the 3D model can accommodate several design concepts, only the cross section design is considered, focusing on the concepts that are easier to manufacture. In addition, the thermal compliance is also a commonly used objective function for thermo-mechanical design. Further, as the probability failure increases with the amount of material, the minimum amount of material problem is also solved. The optimal design under these three objective functions are compared and discussed.

5.1 Analysis model

This chapter focuses on the electrode design on the anode side, and the details of the oxygen gas

flow on the cathode side are not considered. A typical anode supported electrode design contains an active layer where the electrochemical reactions take place, and an anode support. The active layer is a thin layer (~50nm) printed on the top of the anode support, and it is composed by three layers: a cathode, an electrolyte and an anode layer. The active layer is printed upon the relatively thick (~600nm) anode support, as shown in Fig. 5.1.

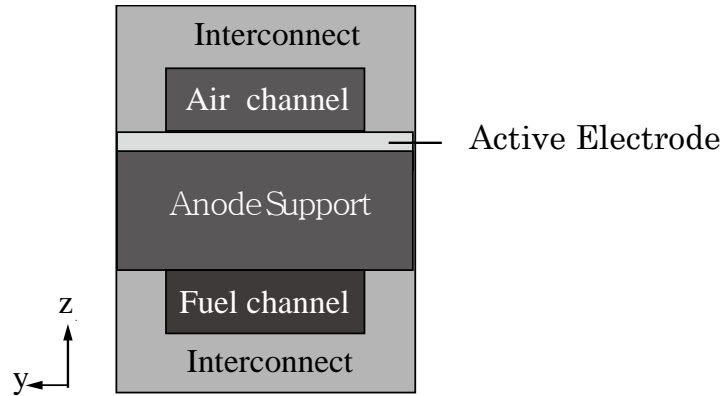


Figure 5.1 The cross section of the fuel supply channel and the electrode

As the active layer in the electrode is much thinner compared to the anode support, the effect of the active layer is simplified to be a boundary condition on the anode support layer, and the analysis only concerns the region occupied by the anode support and the fuel flow. Since it is difficult to make a curved active layer, the active layer is assumed to be a plane, and only the shape of the anode support is designed.

The analysis model is composed by four parts: fuel flow, electrochemical reactions, fuel/heat transport and structural deformation. The analysis domain Ω is selected to be a portion of the rectangular fuel supply channel (shown in Fig 5.2(a)). The porous electrode region ω is an unknown sub-domain of Ω , and $\Omega \setminus \omega$ corresponds to the fuel flow region. The active layer of the electrode is assigned to be a plane on the top of the analysis domain, and the effect of the electrochemical reactions can be simulated as a boundary condition of the electrode.

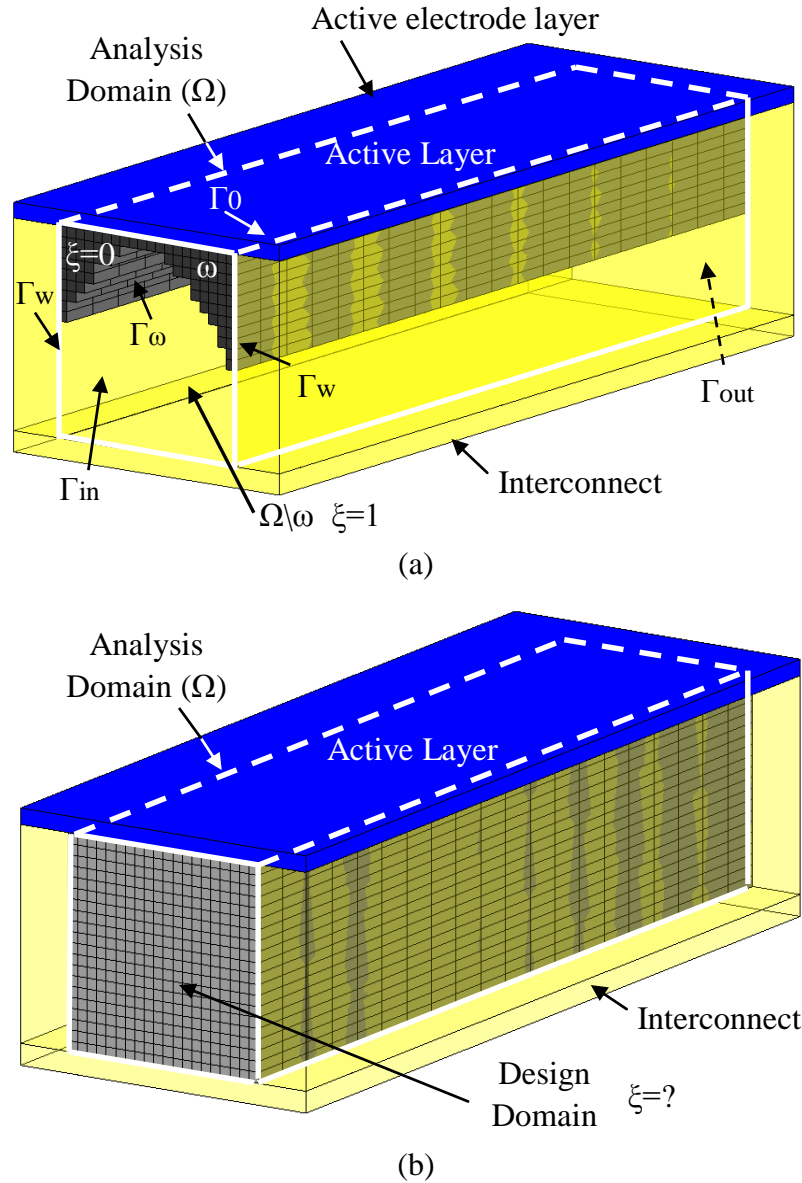


Figure 5.2 The analysis domain (a) and design domain (b) for the anode support

Since the change in the concentration of oxygen gas is not significant, the air flow channel that locates above the active layer is not included in the analysis domain, and the cooling effect of the air flow is simulated as a convection boundary condition on the top boundary of the analysis domain.

Aiming at the establishment of a topology optimization model, the analysis sub domain for both of the fuel flow and the anode support deformation are extended to the whole analysis domain.

The geometry of the electrode is described by a design variable field ξ which has a value 0 in the electrode domain and 1 in the fluid domain.

5.1.1 The fuel flow model

The fuel pumped into the fuel channel is a mixture of hydrogen and water steam. The flow is driven by a prescribed pressure drop $\Delta p \leq 0$. The flow is normally with a medium Reynolds number ($1 < Re < 100$). The density change caused by the fuel consumption is low and the air flow is laminar with low pressure drop, so the fuel flow is assumed to be incompressible and independent with the hydrogen transport.

To show the influence of the porous electrode to the flow field, porous media are distributed in the analysis domain. The porous anode support regions are of low permeability, and the regions with very high permeability permit the flow to pass as in pure fluid.

The flow field is governed by a Brinkman model [59] of steady-state Navier-Stokes equation with a Darcy flow term (in porous media) $\alpha(\xi)$, where ξ is the design variable distribution. $\xi = 0$ in ω (porous), and $\xi = 1$ in $\Omega \setminus \omega$ (fluid), as shown in Fig. 5.2(a)

$$-\nabla \cdot (\mu(\nabla \mathbf{u} + (\nabla \mathbf{u})^T) - \mathbf{I}p) + \mathbf{u} \rho_{Fuel} \nabla \mathbf{u} + \alpha(\xi) \mathbf{u} = 0 \quad \text{in } \Omega \quad (5.1)$$

where \mathbf{u} is the velocity field, p is the pressure. The viscosity μ and the mass density ρ_{Fuel} are constants in the analysis domain.

For incompressible flow, the continuity equation becomes

$$\nabla \cdot \mathbf{u} = 0 \quad (5.2)$$

A wall boundary condition (no slip) is applied on $\Gamma_w \cup \Gamma_0$

$$\mathbf{u} = 0 \quad \text{on } \Gamma_w \cup \Gamma_0 \quad (5.3)$$

and a pressure drop is applied on Γ_{in} and Γ_{out}

$$\mathbf{n}_{in} \cdot \boldsymbol{\sigma} = p_0 \quad \text{on } \Gamma_{in} \quad (5.4)$$

and

$$\mathbf{n}_{out} \cdot \boldsymbol{\sigma} = p_0 + \Delta p \quad \text{on } \Gamma_{out} \quad (5.5)$$

where \mathbf{n}_{in} and \mathbf{n}_{out} are the outward normal of the entrance and exit of the analysis domain, and $\boldsymbol{\sigma}$ is the stress tensor given as

$$\boldsymbol{\sigma} = -p\mathbf{I} + 2\mu\boldsymbol{\varepsilon}(\mathbf{u}) \quad (5.6)$$

$$\boldsymbol{\varepsilon}(\mathbf{u}) = \frac{1}{2} (\nabla\mathbf{u} + (\nabla\mathbf{u})') \quad (5.7)$$

5.1.2 The electrochemical reaction boundary condition

In the active layer of the electrode, the redox reactions consume oxygen gas from the air supply channel and the hydrogen gas from the fuel supply channel to drive the current in the close circuit and generate heat. The current generation depends on the output potential (close circuit potential), concentrations of oxygen and hydrogen gases and the work temperature. The modeling of the electrochemical reactions has been investigated in many works [21][25][60]-[64]. The details of the model are introduced below.

The output potential of SOFC is evaluated by subtracting the polarization overpotential from the open-circuit potential

$$V^{CC} = V^{OC} - \eta^{pol} \quad (5.8)$$

where V^{CC} is the close circuit output potential, V^{OC} is the open circuit potential, and η^{pol} is the polarization overpotential includes ohmic, activation, and concentration effects.

The activation polarization usually dominates the polarization effect $\eta^{pol} \approx \eta^{act}$, and the anodic and cathodic activation polarizations are described by the Butler-Volmer equation

$$i = i_0^a \left[\exp\left(\alpha_a^a \frac{F}{RT} \eta_{act}^a\right) - \exp\left(-\alpha_c^a \frac{F}{RT} \eta_{act}^a\right) \right] \quad (5.9)$$

$$i = i_0^c \left[\exp\left(\alpha_a^c \frac{F}{RT} \eta_{act}^c\right) - \exp\left(-\alpha_c^c \frac{F}{RT} \eta_{act}^c\right) \right] \quad (5.10)$$

where i is the output current density; α_a^a , α_c^a , α_a^c and α_c^c are the anodic-anodic, anodic-cathodic, cathodic-anodic and cathodic-cathodic charge transfer coefficient, respectively; η_{act}^a and η_{act}^c are the activation potential of anode and cathode, and $\eta^{act} = \eta_{act}^a + \eta_{act}^c$; F is the Faraday's constant; R is the universal gas constant. i_0^a and i_0^c are the anodic and cathodic current densities which can be calculated by

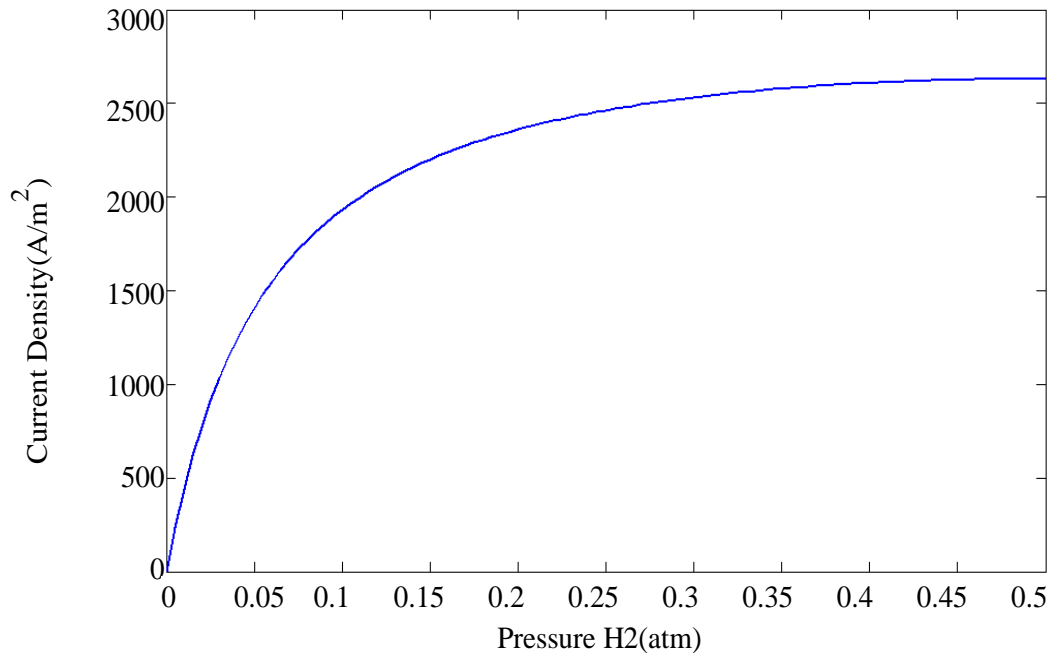
$$i_0^a = \gamma_a \left(\frac{p_{H_2}}{p_{ref}} \right) \left(\frac{p_{H_2O}}{p_{ref}} \right) \exp\left(-\frac{E_{act}^a}{RT}\right) \quad (5.11)$$

$$i_0^c = \gamma_c \left(\frac{p_{O_2}}{p_{ref}} \right)^{0.25} \exp\left(-\frac{E_{act}^c}{RT}\right) \quad (5.12)$$

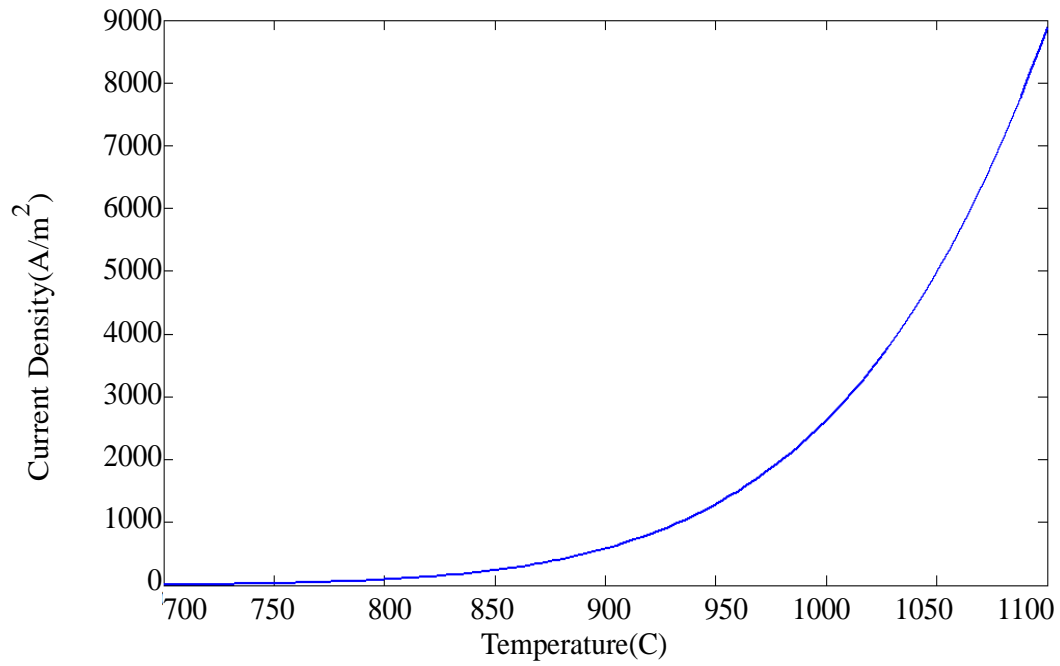
For the simplification of the analysis model, EQ. 5.9 and EQ.5.10 are linearized, and the output current density is expressed as

$$i = \frac{\eta_{act}}{\frac{RT}{(\alpha_a^a + \alpha_c^a) F i_0^a} + \frac{RT}{(\alpha_a^c + \alpha_c^c) F i_0^c}} \quad (5.13)$$

If the output potential V^{cc} is fixed, the current generation i becomes a function of p_{H_2} , p_{H_2O} , p_{O_2} and T . The examples of the i - p_{H_2} curve and the i - T curve are shown in Fig. 5.3, where i is more sensitive with temperature than hydrogen pressure.



(a) $i-p_{H_2}$ curve



(b) $i-T$ curve

Figure 5.3 The $i-p_{H_2}$ curve and the $i-T$ curve

The corresponding hydrogen gas consumption rate is

$$h_i = -\frac{i}{zq_e n_0} \quad (5.14)$$

where z is the particle charge of oxygen ion, q_e is the electron charge and n_0 is the Avogadro constant.

Besides the current generation and hydrogen gas consumption, the electrochemical reactions also introduce the following boundary heat sources:

$$q_{rev} = T\Delta S \left(\frac{i}{2F}\right) \quad (5.15)$$

$$q_{irev} = \eta_{act} i \quad (5.16)$$

where ΔS is the entropy change in the reactions, and EQ. 5.15 and EQ. 5.16 represent the reversible and an irreversible heat generation, respectively.

5.1.3 The hydrogen/heat transport model

The model of a convection diffusion equation with a design dependent hydrogen gas diffusivity distribution is used to express the hydrogen gas transport route around the porous electrode [65]

$$\mathbf{u} \cdot \nabla c_{H_2} - \sigma_{H_2}(\xi) \nabla^2 c_{H_2} = 0 \quad \text{in } \Omega \quad (5.17)$$

where c_{H_2} is the concentration of hydrogen gas, and $\sigma_{H_2}(\xi)$ is the design dependent hydrogen gas diffusivity which equals to $\sigma_{H_2}^{flow}$ when $\xi = 1$ and $\sigma_{H_2}^{porous}$ when $\xi = 0$.

The temperature change is not significant, so the ideal gas equation $p_{H_2} = c_{H_2}RT$ shows the

c_{H_2} can be replaced by p_{H_2} in equation and result it

$$\mathbf{u} \cdot \nabla p_{H_2} - \sigma_{H_2}(\xi) \nabla^2 p_{H_2} = 0 \quad \text{in } \Omega \quad (5.18)$$

At the entrance of the fuel flow channel, the pressure of the hydrogen gas is prescribed as

$$p_{H_2} = p_{H_2}^0 \quad \text{on } \Gamma_{in} \quad (5.19)$$

The conductive-convective heat transfer process is also described by convection diffusion equation

$$\mathbf{u} \cdot \nabla (c_{Heat} \rho_{Fuel} T) - \sigma_{Heat}(\xi) \nabla^2 T = 0 \quad \text{in } \Omega \quad (5.20)$$

where c_{Heat} is the specific heat of the fuel, and $\sigma_{Heat}(\xi)$ is the design dependent heat conduction coefficient which equals to σ_{Heat}^{flow} when $\xi = 1$ and σ_{Heat}^{porous} when $\xi = 0$.

Similar to the hydrogen gas transport, the temperature at the entrance is prescribed as

$$T = T_0 \quad \text{on } \Gamma_{in} \quad (5.21)$$

Since the air supply channel is not included in the analysis domain, the cooling effect of the air flow is simulated as a convection boundary condition on the top boundary of the analysis domain.

$$q_c = h_{air} (T - T_0) \quad \text{on } \Gamma_{top} \quad (5.22)$$

Combining the governing equations of the hydrogen gas transport and heat transfer with the electrochemical reaction boundary condition and the convective cooling boundary condition forms the hydrogen/heat transport model.

5.1.4 The thermal structural model

The structural deformation is assumed to be in static case, and the force balance equation is

$$\nabla \cdot \boldsymbol{\sigma} = 0 \quad \text{in } \Omega \quad (5.23)$$

According to the theory of elasticity, the relationship between the nodal displacement and element strain can be expressed as

$$\boldsymbol{\sigma} = \mathbf{D}(\boldsymbol{\varepsilon}_e + \boldsymbol{\varepsilon}_t) \quad (5.24)$$

where

$$\mathbf{D} = \frac{E(\xi)}{(1+\nu)(1-2\nu)} \begin{bmatrix} 1-\nu & \nu & \nu & 0 & 0 & 0 \\ \nu & 1-\nu & \nu & 0 & 0 & 0 \\ \nu & \nu & 1-\nu & 0 & 0 & 0 \\ 0 & 0 & 0 & \frac{1-2\nu}{2} & 0 & 0 \\ 0 & 0 & 0 & 0 & \frac{1-2\nu}{2} & 0 \\ 0 & 0 & 0 & 0 & 0 & \frac{1-2\nu}{2} \end{bmatrix}$$

$$\boldsymbol{\varepsilon}_e = \mathbf{B}\mathbf{x}$$

$$\mathbf{B} = \begin{bmatrix} \frac{\partial}{\partial x} & & & & & \\ & \frac{\partial}{\partial y} & & & & \\ & & \frac{\partial}{\partial z} & & & \\ \frac{\partial}{\partial y} & \frac{\partial}{\partial x} & & & & \\ & \frac{\partial}{\partial z} & \frac{\partial}{\partial y} & & & \\ \frac{\partial}{\partial z} & & \frac{\partial}{\partial x} & & & \end{bmatrix} \mathbf{x}$$

$$\boldsymbol{\varepsilon}_t = \alpha_t(\xi) (T - T_{ref}) [1 \ 1 \ 1 \ 0 \ 0 \ 0]^T \quad (5.25)$$

In EQ. 5.24 and EQ. 5.25, $\boldsymbol{\varepsilon}_e$ and $\boldsymbol{\varepsilon}_t$ are the elastic and thermal strain, respectively; \mathbf{D} is the elasticity matrix; \mathbf{B} is the strain-displacement operator; \mathbf{x} is the displacement vector; T_{ref} is a reference temperature which is usually selected as the temperature of sintering in SOFC problems; $\alpha_t(\xi)$ and $E(\xi)$ are the design-dependent coefficient of thermal expansion and Young's modulus, respectively; ν is the Poisson's ratio. When $\xi = 0$, $\alpha_t(\xi)$ and $E(\xi)$ equal to α_t^a and E_a which are the material properties of the porous anode material, and when $\xi = 1$, $\alpha_t(\xi)$ and $E(\xi)$ are very small values α_t^{min} and E_{min} . As the temperature change in the

analysis domain is small, the Young's modulus, coefficient of thermal expansion and the Poisson's ratio are assumed to be independent with temperature. The anode support is fixed at Γ_W which is the left and right boundary of the design domain.

5.2 Material model

The material properties have been expressed as a mapping from the binary values $\{0, 1\}$ of the design variable ξ to the material properties in the anode support or flow region. They can also be extended to the intermediate design variable to avoid the problem of integer optimization.

To complete the topology optimization model, the interpolated function $\alpha(\xi)$ first proposed by Borrvall and Petersson [59] is used in the flow equations, and a SIMP-like approach for the hydrogen/heat transport is used in a similar manner as in [17]-[19] for the cathode design

$$\alpha^e(\xi^e) = \bar{\alpha} + (\underline{\alpha} - \bar{\alpha})\xi^e \frac{1+q}{\xi^{e+q}} \quad (5.26)$$

$$\sigma_{H_2}^e(\xi^e) = \sigma_{H_2}^{flow}\xi^{e^r} + \sigma_{H_2}^{porous}(1 - \xi^{e^r}) \quad (5.27)$$

$$\sigma_{Heat}^e(\xi^e) = \sigma_{Heat}^{flow}\xi^{e^r} + \sigma_{Heat}^{porous}(1 - \xi^{e^r}) \quad (5.28)$$

where r and q are the penalty factors which are selected as 3 and 1, respectively.

Besides SIMP method, some other interpolation functions, such as RAMP and NLPI has been discussed in [20] and [66], and they have been proved better for thermal strength design. The effect of interpolation functions was discussed by Pederson in [44]. It concluded that the performance of thermal strength design process is sensitive to the interpolation function, and the interpolation function better have a physical background than pure numerical penalty functions.

As the complication in the damage principle for porous ceramic material, the strength design for the anode support is different from the strength for normal materials. The ceramics exhibit a

large range of bulk failure strength due to the random nature in the arrangement of the microstructures. The failure stress of these materials is not a well defined number, so Weibull method is used to give a measure of the strength. The probability of mechanical failure can be calculated as expressed in [28] [29]

$$P_f = 1 - \prod_{i=1}^3 \exp\left(- \int_{\Omega} \left(\frac{\sigma_i}{\sigma_0}\right)^m dV\right) \quad (5.29)$$

where σ_i is the i th principal stress; σ_0 is the characteristic strength; m is the Weibull modulus which is usually 5~7. The ratio between σ_i and σ_0 determines the strength of the anode support, and they both depend on the porosity of the ceramic material. The elasticity of the porous anode material has been shown to have the relationship with the porosity vol% such as [67]

$$E(\text{vol}\%) = \frac{(1 - \text{vol}\%)^2}{1 + SE \times \text{vol}\%} E_0 \quad (5.30)$$

where E_0 is the elasticity of the fully solid material, and SE is a factor determined by experimental data.

Innovated by such a model, using the design variable to replace the porosity, the design-dependent elasticity becomes

$$E(\xi^e) = \frac{(1 - \xi^e)^2}{1 + S_E \xi^e} E_0 \quad (5.31)$$

The thermal expansion term in EQ. 5.25 is proportional to the product of the coefficient of thermal expansion and the Young's modulus, here one can define

$$\beta(\xi^e) = \alpha_t(\xi^e)E(\xi^e) = \frac{(1 - \xi^e)^2}{1 + S_{\beta} \xi^e} \alpha_0 E_0 \quad (5.32)$$

where β is a design dependent factor that represents the strength of the thermal load; α_0 is the

coefficient of thermal expansion of the fully solid material; S_{β} is a penalty factor that should be smaller than S_E .

In a thermal stress dominated problem, the penalized thermal expansion term make the deformation larger for an intermediate ξ^e and may help the design to converge to binary. This technique is similar to the method used for RAMP method [42].

The characteristic strength can also be expressed as a function of the porosity

$$\sigma_0(\text{vol}\%) = \sigma_S \exp(-b \text{vol}\%) \quad (5.33)$$

where σ_S is the characteristic of the fully solid material, and b is a factor determined by experimental data.

Using the design variable to replace the porosity, the design-dependent characteristic strength becomes

$$\sigma_0(\xi^e) = \sigma_S \exp(-b \xi^e) \quad (5.34)$$

Note that the usual selection of $b=3\sim 3.5$ makes $\sigma_0(\xi^e)$ decrease faster than $E(\xi^e)$ and $\beta(\xi^e)$ near the $\xi^e=0$ end and slower near the $\xi^e=1$ end. The ratio between $\beta(\xi^e)$ and $\sigma_0(\xi^e)$ is shown in Fig. 5.4, and the convex shape of the curve means that the material with an intermediate ξ^e is more vulnerable than $\xi^e=0$ and $\xi^e=1$, which can help the design to converge. A density filter with a linear weight is also used to prevent the appearance of checkerboard patterns and to control feature size.

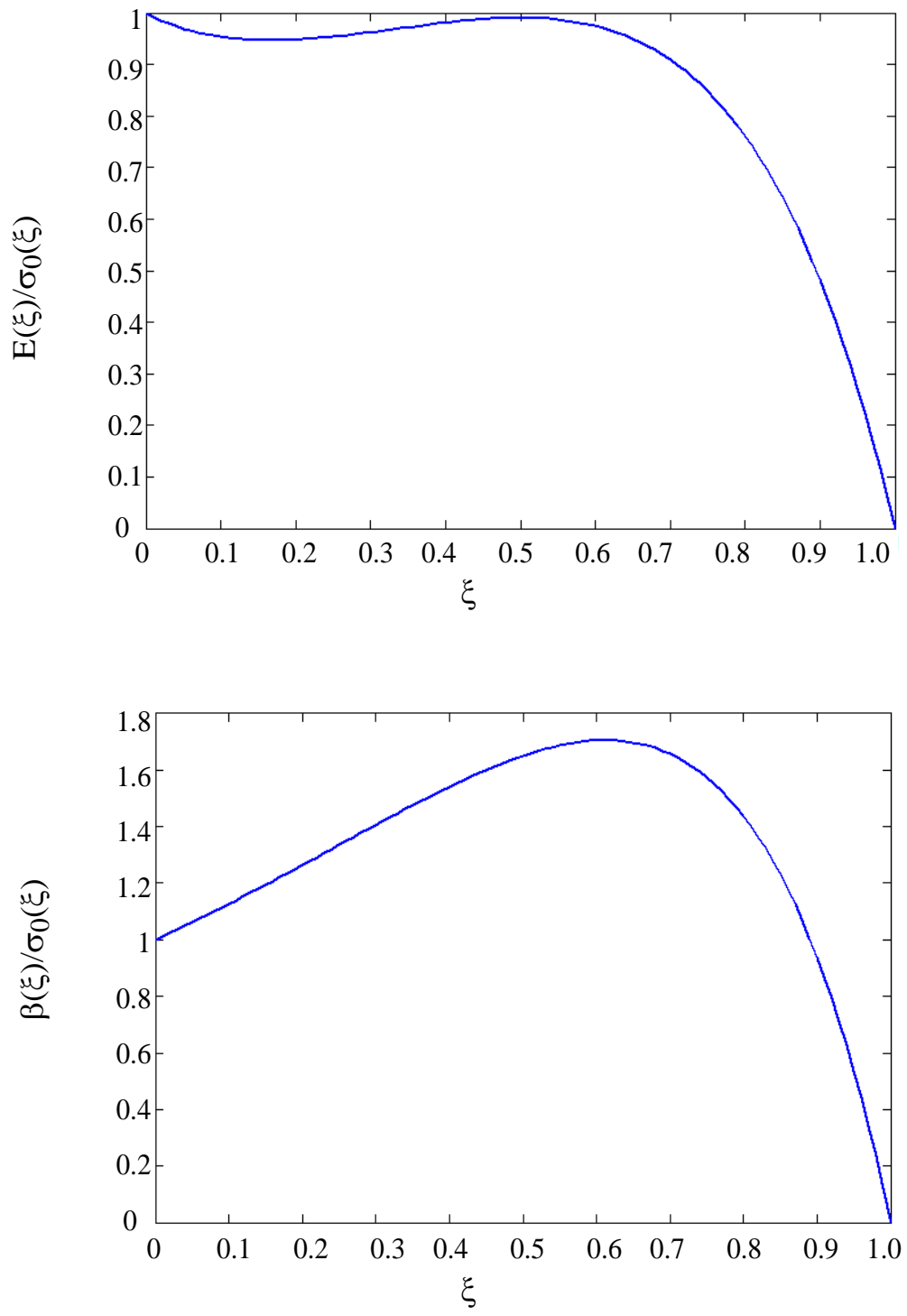


Figure 5.4 The material models for thermo-mechanical problem

5.3 Finite element model

The analysis domain Ω is discretized by 8 node rectangular elements, and the fuel flow, the hydrogen gas transport, and the heat transfer share the same mesh. However, the equal order interpolation of the velocity and pressure fields does not satisfy the Ladyzhenskaya-Babuška-Brezzi (LBB) condition for the flow problem, and this result in numerical oscillations in pressure [59]. A SUPG stabilizer which penalizes large pressure gradients was introduced [68], and this results in the stabilized matrices form of the flow equations (EQ. 5.1 and EQ. 5.2) is given as

$$\sum_e \begin{bmatrix} K_{NS}^e(\mathbf{u}) + K_D^e(\mathbf{u}, \alpha^e(\xi^e)) & G_{NS}^e(\mathbf{u}) \\ L_{NS}^e(\mathbf{u}) & M_{NS}^e(\mathbf{u}) \end{bmatrix} \begin{pmatrix} \mathbf{u}^h \\ p^h \end{pmatrix} = - \sum_e \begin{bmatrix} G_{NS}^e(\mathbf{u}) \\ M_{NS}^e(\mathbf{u}) \end{bmatrix} \Delta p \quad \text{in } \Omega \quad (5.35)$$

where \mathbf{u}^h and p^h belong to suitable admissible spaces V_u^h and V_p^h , respectively. Δp is the pressure drop vector which equals to Δp only on nodes located at Γ_{out} . K_{NS}^e , G_{NS}^e , L_{NS}^e and M_{NS}^e are the element stiffness matrices with the SUPG stabilizer for the Navier-Stokes flow, and K_D^e corresponds to the Darcy flow term in EQ. 5.1.

Both of the hydrogen gas transport and the heat transfer are convection dominated and they also need to be stabilized. In matrix form, equation for the couple problem (EQ. 5.18 and EQ. 5.20) including SUPG stabilization [69] are

$$\sum_e \begin{bmatrix} K_{conv}^e(\mathbf{u}) + K_{diff}^e(\xi^e) + K_{stab}^e(\mathbf{u}, \xi^e) & 0 \\ 0 & K_{conv,T}^e(\mathbf{u}) + K_T^e(\xi^e) + K_{stab,T}^e(\mathbf{u}, \xi^e) \end{bmatrix} \begin{pmatrix} c^h \\ \mathbf{T}^h \end{pmatrix} = \sum_{\partial e} \begin{bmatrix} H^e(c^h, \mathbf{T}^h, \Delta \xi_j^e) \\ Q^e(c^h, \mathbf{T}^h, \Delta \xi_j^e) \end{bmatrix} \quad \text{in } \Omega \quad (5.36)$$

where c^h and \mathbf{T}^h belong to suitable admissible spaces V_c^h and V_T^h , respectively. K_{conv}^e , $K_{diff}^e(\xi^e)$ and $K_{stab}^e(\mathbf{u}, \xi^e)$ are the element stiffness matrices of the convection, diffusion and

stabilizer terms of the hydrogen gas transport, and $K_{\text{conv},T}^e$, K_T^e and $K_{\text{stab},T}^e$ are the element stiffness matrices of the convection, diffusion and stabilizer terms of the heat transfer, respectively. H^e and Q^e are the element hydrogen consumption and heat generation terms correspond to EQ. 5.14-5.16.

The finite element equation for the thermal stress problem is written as

$$\sum_e K_S^e(\xi^e) \mathbf{x}^h = \sum_e F_{TE}^e(\xi^e, T, T_0) \quad \text{in } \Omega \quad (5.37)$$

where \mathbf{x}^h is the nodal displacement vector which belongs to suitable admissible spaces V_X^h ;

K_S^e is the structural stiffness matrix, and F_{TE}^e is the thermal expansion load vector.

5.4 Objective functions

The most commonly used objective function for thermal stress problems is the thermal compliance investigated in [41]-[44]. The thermal compliance can be expressed as

$$C_T = \mathbf{x}^h T \sum_e K_S^e(\xi^e) \mathbf{x}^h \quad (5.38)$$

However, Pederson questioned this objective function in [43] [44] for the reason that it may not consistent with the purpose of improving structural strength. For the problem of the anode support design, due to the specific failure principle of the ceramic material, the expression of the probability of failure derived by Weibull in EQ. 5.29 is a better selection for the strength design.

In this chapter, both the thermal compliance and the probability of failure are used as objective functions, and the results are compared in section 5.8.

5.5 Constraints

As the thickness of the anode support increases, the stiffness of the electrode is improved. However, the current generation is reduced at the same time, because the anode support impedes

the hydrogen gas transport to the active layer of the electrode. Also, for a given applied stress, the probability of failure increases with the increase of the volume (amount of material). This is known as the ‘volume effect’ and is consistent with a larger volume containing a physically larger flaw which results in a larger stress concentration [29].

In optimization to prevent thermo-mechanical failure, the stiffness of the electrode and the current generation should be constrained. The stiffness can be measured by the static compliance, which is defined as

$$C_S = \mathbf{x}_S^h \sum_e K_S^e(\xi^e) \mathbf{x}_S^h \quad (5.39)$$

where \mathbf{x}_S^h is the deformation of the electrode under a uniformly distributed stress applied on Γ_{top} (Fig 5.1(a)), and it can be solved by

$$\sum_e K_S^e(\xi^e) \mathbf{x}_S^h = \mathbf{F}_S \quad (5.40)$$

where \mathbf{F}_S is the force vector that represents the uniformly distributed stress.

The total current generation can be expressed as

$$I = \sum_e I_e \quad (5.41)$$

where I_e represents the summation of the current generation in EQ. 5.13.

Besides the static compliance and the current generation, another constraint of the total fuel flow rate is necessary to ensure the generation of a flow path. The fuel flow rate can be written as

$$Q_F = - \int_{\Gamma_{in}} \mathbf{u} \cdot \mathbf{n}_{in} dA \quad (5.42)$$

where \mathbf{n}_{in} is the outer unit normal vector on Γ_{in} .

The flow rate constrain is active only at the beginning of the design, and it becomes inactive as the iterations progresses.

5.6 Optimization problems

The design domain for all the design problems is demonstrated as shown in Fig. 5.2(b). The first

optimization problem uses the thermal compliance as the objective function. The problem is:

Find $\xi \in \Theta$ that

Minimize

$$C_T = \mathbf{x}^h T \sum_e K_S^e(\xi^e) \mathbf{x}^h \quad (5.38)$$

Subject to

$$C_S \leq C_S^{\max} \quad (5.43)$$

$$I \geq I_{\min} \quad (5.44)$$

$$Q_F \geq Q_F^{\min} \quad (5.45)$$

$$0 \leq \xi^e \leq 1, \quad e = 1, 2, 3, \dots, N \quad (5.46)$$

and (discretized) state equations, EQ. 5.35-5.37, discussed in section 5.3. In this problem C_S^{\max} ,

I_{\min} and Q_F^{\min} are prescribed upper bound on the static compliance, lower bounds on the current generation and fuel flow rate, respectively. The set Θ is used simply to define regions Ω_0 where the anode material is prescribed.

Specifically,

$$\Theta = \{\xi \in [0, 1]^N : \xi^e = 0 \text{ if } e \in \Omega_0\} \quad (5.47)$$

In EQ. 5.47 Ω_0 is subset of Ω where ξ is prescribed to have value 0 (anode support).

The second problem uses the probability of failure as the objective function. The problem is:

Find $\xi \in \Theta$ that

Minimize

$$P_f = 1 - \prod_{i=1}^3 \exp(- \sum_e (\frac{\sigma_i}{\sigma_0})^m v_e) \quad (5.48)$$

Subject to

$$C_S \leq C_S^{\max} \quad (5.43)$$

$$I \geq I_{\min} \quad (5.44)$$

$$Q_F \geq Q_F^{\min} \quad (5.45)$$

$$0 \leq \xi^e \leq 1, \quad e = 1, 2, 3, \dots, N \quad (5.46)$$

and (discretized) state equations, EQ. 5.35-5.37, discussed in section 5.3. EQ. 5.48 is the discretized form of EQ. 5.29.

5.7 Sensitivity analysis

The sensitivity of the objective functions or the constraints in section 4.6 can be derived in the same manner. The sensitivity of the probability of failure is taken as the example

$$\frac{\partial P_f}{\partial \xi^e} = \frac{\partial P_f}{\partial \sigma_i} \frac{\partial \sigma_i}{\partial \xi^e} + \frac{\partial P_f}{\partial \sigma_0} \frac{\partial \sigma_0}{\partial \xi^e} \quad (5.49)$$

Only the term $\partial \sigma_i / \partial \xi^e$ is unknown in EQ. 5.49.

The principal stresses are the eigenvalues of the stress tensor $\boldsymbol{\sigma}$, which is defined in EQ. 5.24.

$$\boldsymbol{\sigma} = \mathbf{D}(\xi)(\varepsilon_e + \varepsilon_t) = \mathbf{D}(\xi)(\mathbf{B}\mathbf{x}(\xi) + \alpha_t(\xi)(T(\xi) - T_{\text{ref}})[1 \ 1 \ 1 \ 0 \ 0 \ 0]^T) \quad (5.24)$$

Taking derivative to EQ. 5.24, gives

$$\begin{aligned} \frac{\partial \boldsymbol{\sigma}}{\partial \xi} &= \frac{\partial \mathbf{D}(\xi)}{\partial \xi} \mathbf{B}\mathbf{x}(\xi) + \mathbf{D}(\xi)\mathbf{B} \frac{\partial \mathbf{x}(\xi)}{\partial \xi} + \frac{\partial \mathbf{D}(\xi)\alpha_t(\xi)}{\partial \xi} \\ &(\mathbf{T} - T_{\text{ref}}) [1 \ 1 \ 1 \ 0 \ 0 \ 0]^T + \mathbf{D}(\xi)\alpha_t(\xi)\alpha_t(\xi) \\ &\frac{\partial T(\xi)}{\partial \xi} [1 \ 1 \ 1 \ 0 \ 0 \ 0]^T \end{aligned} \quad (5.50)$$

The principal stresses are the solution to the eigenvalue problem

$$(\boldsymbol{\sigma} - \sigma_i \mathbf{I})\mathbf{v}_i = 0 \quad (5.51)$$

where \mathbf{v}_i is the corresponding eigenvector. The sensitivity of σ_i can be derived from EQ. 5.51

$$\frac{\partial \sigma_i}{\partial \xi} = \frac{\mathbf{v}_i^T \frac{\partial \boldsymbol{\sigma}}{\partial \xi} \mathbf{v}_i}{\mathbf{v}_i^T \mathbf{v}_i} \quad (5.52)$$

To eliminate $\partial \mathbf{x}(\xi) / \partial \xi$ and $\partial T(\xi) / \partial \xi$ terms, one can use adjoint method. Taking the derivative

of EQ. 5.35-5.37, gives

$$\begin{pmatrix} \frac{\partial \mathbf{u}}{\partial \xi} \\ \frac{\partial \mathbf{p}}{\partial \xi} \end{pmatrix} = - \begin{bmatrix} K_{NS}(\mathbf{u}) + K_D(\mathbf{u}, \boldsymbol{\alpha}^e(\xi)) + \frac{\partial K_D}{\partial \mathbf{u}} \mathbf{u} + \frac{\partial G_{NS}}{\partial \mathbf{u}} (\mathbf{p} + \Delta \mathbf{p}) & G_{NS}(\mathbf{u}) \\ L_{NS}(\mathbf{u}) + \frac{\partial L_{NS}}{\partial \mathbf{u}} \mathbf{u} + \frac{\partial M_{NS}}{\partial \mathbf{u}} (\mathbf{p} + \Delta \mathbf{p}) & M_{NS}(\mathbf{u}) \end{bmatrix}^{-1} \begin{pmatrix} \frac{\partial K_D(\mathbf{u}, \boldsymbol{\alpha}^e(\xi^e)) \mathbf{u}}{\partial \xi} \\ 0 \end{pmatrix} \quad (5.53)$$

$$\begin{pmatrix} \frac{\partial \mathbf{c}}{\partial \xi} \\ \frac{\partial \mathbf{T}}{\partial \xi} \end{pmatrix} = \begin{bmatrix} K_{conv} + K_{diff} + K_{stab} - \frac{\partial H}{\partial \mathbf{c}} & -\frac{\partial H}{\partial \mathbf{T}} \\ -\frac{\partial Q}{\partial \mathbf{c}} & K_{conv, T} + K_T + K_{stab, T} - \frac{\partial Q}{\partial \mathbf{T}} \end{bmatrix}^{-1} \begin{pmatrix} \frac{\partial H}{\partial \xi} \\ \frac{\partial Q}{\partial \xi} \end{pmatrix} - \begin{bmatrix} \frac{\partial (K_{diff}(\xi) + K_{stab}(\mathbf{u}, \xi))}{\partial \xi} & 0 \\ 0 & \frac{\partial (K_T(\xi) + K_{stab, T}(\mathbf{u}, \xi))}{\partial \xi} \end{bmatrix} \begin{pmatrix} \mathbf{c} \\ \mathbf{T} \end{pmatrix} - \begin{pmatrix} \frac{\partial (K_{conv}(\mathbf{u}) + K_{stab}(\mathbf{u}, \xi))}{\partial \mathbf{u}} \mathbf{c} \\ \frac{\partial (K_{conv, T}(\mathbf{u}) + K_{stab, T}(\mathbf{u}, \xi))}{\partial \mathbf{u}} \mathbf{T} \end{pmatrix} \frac{\partial \mathbf{u}}{\partial \xi} \quad (5.54)$$

$$\frac{\partial \mathbf{x}(\xi)}{\partial \xi} = K_S^{-1} \left(\frac{\partial F_{TE}}{\partial \xi} - \frac{\partial K_S}{\partial \xi} \mathbf{x}(\xi) + \frac{\partial F_{TE}}{\partial \mathbf{T}} \frac{\partial \mathbf{T}(\xi)}{\partial \xi} \right) \quad (5.55)$$

By combining EQ. 5.49-5.55, the three adjoint problems can be set up and the sensitivity of P_f can be obtained by solving the adjoint problems in a similar manner to the sensitivity analysis in Chapter 2 and Chapter 4.

5.8 Examples

The cross section of the anode support in a fuel supply channel of SOFC is designed for three different objective functions. In these examples the analysis domain Ω is a rectangular domain of the size 20mm(length) \times 2mm(width) \times 2mm(height), and it is discretized by $40 \times 20 \times 20$ elements. The design domain is shown in Fig. 5.2, and its top layer is fixed to be the anode support. The material properties are consistent with the data from [23][64] for a Ni/YSZ anode and LSM cathode. The anode is assumed to be sintered at $T_0 = 1400^\circ\text{C}$, and the anode works in the inlet flow with $T = 1000^\circ\text{C}$.

The designs for minimum thermal compliance, minimum probability of failure and minimum amount of material are discussed in the following sections. A flat anode support design with a constant thickness of $600\mu\text{m}$ is used as the reference design, as illustrated in Fig. 5.5, where the black pixels represent the anode support and the white pixels represent the fuel flow path. The finite element analysis is solved by frontal method [70], and all optimization problems are solved using the method of moving asymptotes of Svanberg [50]. Results reported are after post-processing, applying a threshold at $\xi=0.5$ to remove the intermediate density elements left in the optimal solutions.



Figure 5.5 The reference flat design with a constant thickness of $600\mu\text{m}$, the black pixels represent the anode support; the white pixels represent the fuel flow path

5.8.1 Minimum the thermal compliance

The thermal compliance shows the total strain energy in the anode support under thermal load.

The optimal cross section with the minimum thermal compliance problem is shown in Fig. 5.6, and the performance is shown in Table 5.1.



Figure 5.6 The optimal cross section in example 5.8.1 for the minimum probability problem

Table 5.1 The performance of the anode support design for the thermal compliance design

	Current generation (A)	Static compliance (Nm)	Probability of failure	Thermal Compliance (Nm)
Optimal Design	0.0901	4.70×10^{-9}	2.01×10^{-4}	0.2408
Reference Design	0.0901	4.70×10^{-9}	2.08×10^{-4}	0.2557

The current generation and the static compliance are constrained the same as the reference design, and the flow rate constraint is not active. As the work temperature is much lower than the sintering temperature ($T = 1000^\circ\text{C} < T_0 = 1400^\circ\text{C}$), a high tensile stress is generated in the anode, so the anode forms an arc-like shape to reduce the stress. The improvements for the thermal compliance and the probability of failure are 6% and 5% of the reference values, respectively, which are essentially not significant.

5.8.2 Minimum the probability of failure

Although minimizing the thermal compliance has a positive effect on reducing the probability of failure, the thermal compliance emphasizes more on the global distribution of the thermal stress. However, the high Weibull modulus in EQ. 5.29 works like a penalty, which make the damage depend “localized maximum” of the stresses. The optimal cross section with the minimum probability of failure problem is shown in Fig. 5.7, and the performance is shown in Table 5.2.

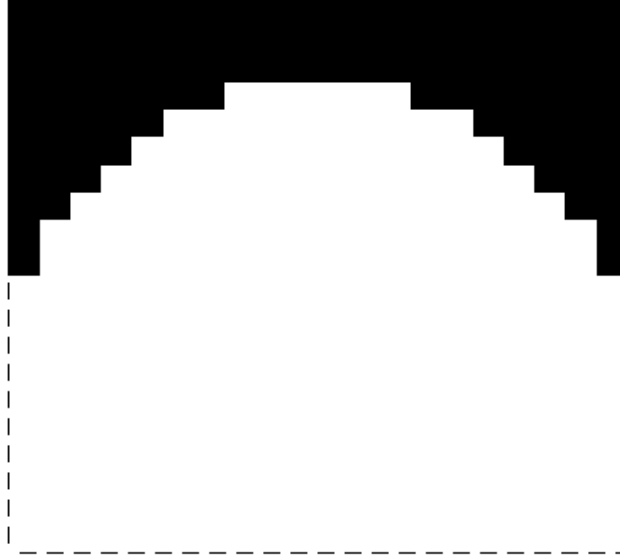


Figure 5.7 The optimal cross section in example 5.8.2 for the minimum probability problem

Table 5.2 The performance of the anode support design for the probability of failure design

	Current generation (A)	Static compliance (Nm)	Probability of failure
Optimal Design	0.0901	4.70×10^{-9}	1.89×10^{-4}
Reference Design	0.0901	4.70×10^{-9}	2.08×10^{-4}

The current generation and the static compliance are constrained the same as the reference design, and the flow rate constraint is not active. As discussed in section 5.8.1, the high tensile stress generated in the anode make the anode form an arc-like shape to reduce the stress. Different from the thermal compliance problem, the minimum probability of failure emphasize on releasing the largest stress which happens near the left and right boundaries of the anode, so the arc becomes more convex. The optimal design has an improvement of 10% the reference value in the probability of failure. One may also note that although topology optimization method permits the creation of holes in the structure, the thermal stress dominated problems tend not to generated holes to prevent stress concentration.

5.9 Conclusions

Since the sintering temperature of the anode is much higher than the work temperature, strong thermal stresses are generated inside the porous ceramic anode materials. The complications in the principle of mechanical failure in these materials result in a large divergence of failure stresses, so the concept of failure stress fails to measure the structural strength. Currently, the Weibull analysis based on the weakest link theory has been proved to be a good way to measure the structural strength of this type of material.

The expression of the probability of failure shows that the probability increased rapidly with the increase of thermal stresses. Besides the expression of the probability of failure, the thermal compliance can also be treated as a measure of the thermal stress. Therefore, the thermal compliance and the probability of failure were selected as the objective functions.

The material model has a significant influence on the topology optimization for thermal stress problem. A new material model was set up specifically for the probability of failure. This material model was based on the previous experimental work of the dependency of the material properties on the porosity. This material model helped the design to converge to binary by making the intermediate designs more vulnerable than the binary design.

The optimal designs for minimizing the thermal compliance and the probability of failure show arc-like designs, which enable the structure to bend under thermal loads to reduce thermal stresses. The two designs both rejected the holes to prevent the stress concentration. Although the improvement from the direct design of the probability of failure is larger than the improvement from the thermal compliance design, the improvement is not remarkable under the constraints of the static compliance and current generation. The assumption of the planar active electrode layer at the top of the design also restricts the geometry of the design from being more

curved to reduce the thermal stresses. If the active electrode layer is permitted to be curved, a larger improvement can be expected.

The SOFC modeled in this chapter works at a high temperature that is lower than the sintering temperature. The trend of SOFC development is to design SOFCs that work at a much lower temperature, and this makes the probability of failure more significant than the case in this chapter.

Chapter 6 Conclusions

A topology optimization model simplifying the 3D microstructure into a 2D conduction problem with convection boundary condition was developed in chapter 2 to improve the current generation, and the formulation can result in a clear binary design with no intermediate (gray) region. The 2D model shows the effect of the surface resistance and the bulk resistance, but the assumption of 2D geometry makes some designs which can exist in 3D case inadmissible, such as the designs with disjoint parts or enclosed gas regions. Some techniques were used to avoid the inadmissible designs. The designs with different material properties and geometric factors were presented. The effect of surface resistance, perimeter of the geometry and the amount of material in the scaffold was discussed, and a maximum improvement of 50% was found. The 2D design shows that for the current MIEC material with relatively high surface resistance, the perimeter of the scaffold dominates the design and the scaffold tends to have long and thin features; for better MIEC materials with low surface resistance, the bulk resistance of the scaffold becomes significant, and the amount of material has a larger influence on the design. However, the 2D design cannot be used directly to guide the 3D microstructure design.

A similar 3D finite element formulation was set up in preparation for the 3D microstructure design optimization. A gas diffusion model was added to the simplified model to show the effect of the change in oxygen gas concentration. A detailed mesh for the cathode microstructure was reconstructed from the experimental data of 3D focused ion beam-scanning electron microscopy.

The simulation results have a good consistency with the experimentally measured data at the low temperature region, but there is a larger difference at the high temperature region due to some unknown physical reasons due to the weakening of oxygen gas diffusion in nano-dimensional pores. This simulation model served as a solid base for the 3D microstructure design for the low temperature SOFC cathode.

Based on the 3D finite element model, a 3D topology optimization formulation was set up to overcome the problems of inadmissible designs and also to provide a direct for the 3D microstructure design. Compared with the 2D model, the inadmissible designs were no longer dealt with specifically because the remove of the 2D assumption permitted these design to exist in the 3D model. In addition, to prevent the local minimums that can lock the design from growing, the material model for the surface resistance was modified to depend both of the first and second spatial derivatives of the design variables. Improvements of up to 35% were observed. Consistent with the 2D designs, the designs at lower temperatures (worse material performances) spans the whole design domain and has thinner features to enlarge the surface area and tortuosity of the scaffold; at higher temperatures (better material performance) the scaffold becomes shorter and thicker with smaller surface area and tortuosity to reduce the bulk resistance.

In the second part of this dissertation, a coupled design model including the fuel flow, heat transfer, electrochemical reaction and thermo-mechanical deformation was established to design the geometry of the anode support in SOFC stacks to improve the thermal strength. For the porous ceramic anode material, the concept of failure stress failed and the probability of failure evaluated by Weibull analysis based on the weakest link theory was used to measure the strength of the anode support. A specific material model was developed based on the experimental data of

the material properties of the porous materials, and this material model helped the design to converge to binary (black-white).

Increasing the thermal stress can enhance the probability of failure, so the thermal compliance, which represents the strain energy under the thermal loads, was used as the first objective function. The probability of failure itself was also used as the objective function in the second example.

The direct design and the thermal compliance design can make the probability of failure reduce 10% and 5% of the reference values, respectively. The arc-like shapes of the designs in the first two examples reducing the probability of failure by making the structure bend under thermal loads to reduce thermal stresses. The two designs both rejected the holes to prevent the stress concentration. The improvements from the designs are not significant, and this leads to a thought that some of the design assumptions should be released.

In future work removing the assumption of the planar active electrode layer at the top of the design should be considered, the design is expected to have a larger bending deformation and reduce the probability of failure by releasing more thermal stresses. However, making a curved active electrode layer may require further investigation on new manufacturing techniques. As the trend of SOFC development is to design SOFCs that operate at a much lower temperature, the probability of failure can be more significant than in current SOFC, and this work provided a methodology that can be use in the thermal strength design.

BIBLIOGRAPHY

BIBLIOGRAPHY

- [1] Adler SB (2004) Factors governing oxygen reduction in solid oxide fuel cell cathodes. *Chem Rev* 104, pp4791-4843
- [2] O'Hayre RP, Cha SW, Colella WG, Prinz FB (2009) *Fuel cell fundamentals*. Wiley, New York, pp 270-272
- [3] Li XG (2006) *Principles of fuel cells*, Taylor Francis, New York, pp 494-503
- [4] Jiang SP, Leng YJ, Chan SH and Khor KA (2003) Development of (La,Sr)MnO₃-based cathodes for intermediate temperature solid oxide fuel cells, *Electrochem. Solid State Lett.*, 6 (4), pp A67-A70.
- [5] Jiang SP and Wang W (2005) Novel structured mixed ionic and electronic conducting cathodes of solid oxide fuel cells, *Solid Oxide Fuel Cells*, 176 (15-16), pp 1351-1357.
- [6] Shah M, Barnett SA (2008) Solid oxide fuel cell cathodes by infiltration of La_{0.6}Sr_{0.4}Co_{0.2}Fe_{0.8}O_{3-x} into Gd-doped ceria. *Solid State Ionics* 179, pp2059-2064
- [7] Nicholas JD, Barnett SA (2010) Measurements and modeling of Sm_{0.5}Sr_{0.5}CoO_{3-x}—Ce_{0.9}Gd_{0.1}O_{1.95} SOFC cathodes produced using infiltrate solution additives. *J Electrochem Soc* 157, pp B536
- [8] Shah M, Nicholas JD, Barnett SA (2009) Prediction of infiltrated solid oxide fuel cell cathode polarization resistance using simple models. *Electrochem Commun* 11, pp2-5
- [9] Chan SH, Khor K, Xia ZT (2001) A complete polarization model of a solid oxide fuel cell its sensitivity to the change of cell component thickness. *J Power Sources* 93, pp130-140
- [10] Deseure J, Bultel Y, Dessemond L, Siebert E (2005) Theoretical optimization of a SOFC composite cathode. *Electrochim Acta* 50(10), pp2037-2046
- [11] Haanappel VAC, Mertens J, Rutenbeck D, Tropaetz C, Herzhof W, Sebold D, Tietz F (2005) Optimisation of processing microstructural parameters of LSM cathodes to improve the electrochemical performance of anode-supported SOFCs. *J Power Sources* 141, pp216-226
- [12] Kenney B, Karan K (2007) Engineering of microstructure design of a planar porous composite SOFC cathode: a numerical analysis. *Solid State Ionics* 178, pp297-306
- [13] Tanner CW, Fung KZ, Virkar AV (1997) The effect of porous composite electrode structure on solid oxide fuel cell performance: theoretical analysis. *J Electrochem Soc* 144(1), pp 21-30

- [14] Wang L, Nicholas JD (2011) Simple Infiltrated Microstructure Polarization Loss Estimation (SIMPLE) model predictions of today tomorrow's nano-composite SOFC cathodes. In: Singhal S, Eguchi K (eds) Twelfth international symposium on solid oxide fuel cells, pp 2321-2329 (ECS Transactions, The Electrochemical Society, Montreal, Canada, 2011)
- [15] Farhad S, Hamdullahpur F (2012) Optimization of the microstructure of porous composite cathodes in solid oxide fuel cells. *AICHE J* 58(4), pp1248-1261
- [16] Iwai H, Kuroyanagi A, Saito M, Konno A, Yoshida H, Yamada T, Nishiwaki S (2011) Power generation enhancement of solid oxide fuel cell by cathode-electrolyte interface modification in mesoscale assisted by level set-based optimization calculation. *J Power Sources* 196, pp3485-3495
- [17] Song X, Diaz AR, Benard A (2012) Topology optimization of a composite cathode in a Solid Oxide Fuel Cell, ICTAM 2012, Aug. 19-24, Beijing, China
- [18] Song X, Diaz AR, Benard A (2013) A 3D topology optimization model of the cathode air supply channel in planar solid oxide fuel cell, 10th World Congress on Structural and Multidisciplinary Optimization, May 19 -24, Orlando, Florida, USA
- [19] Song X, Diaz AR, Benard A, Nicholas JD (2012) A 2D model for shape optimization of solid oxide fuel cell cathodes, *Struct Multidisc Optim* 44, pp19-24
- [20] Stolpe M, Svanberg K (2001) An alternative interpolation scheme for minimum compliance topology optimization. *Struct Multidisc Optim* 22, pp 116-124
- [21] Kakaç A, Pramuanjaroenkiy A, Zhou X (2007) A review of numerical modeling of solid oxide fuel cell. *International Journal of Hydrogen Energy* 32, pp761:786
- [22] Weibull W (1939) A statistical theory of the strength of materials, *Proc. Roy. Swed. Inst. Eng. Res.* 151, pp 1-45
- [23] Atkinson A, Selçuk A (2000) Mechanical behavior of ceramic oxygen ion-conducting membranes. *Solid State Ionics* 134, pp59-66
- [24] Cheng M, Cui D (2009) Thermal stress modeling of anode supported micro-tubular solid oxide fuel cell. *Journal of Power Sources* 192, pp 400-407
- [25] Peksen M (2011) A coupled 3D thermofluid-thermomechanical analysis of a a planar type production scale SOFC stack. *International Journal of Hydrogen Energy* 36, pp 914-928
- [26] Chiang L, Liu H, Shiu Y, Lee C, Lee R (2010) Thermal stress and thermo-electrochemical analysis of a planar anode-supported solid oxide fuel cell: Effects of anode porosity. *Journal of Power Sources* 195, pp 1895-1904

- [27] Lin C, Chena T, Chyoub Y, Chiang L (2007) Thermal stress analysis of a planar SOFC stack. *Journal of Power Sources* 164, pp 238-251
- [28] Nakajo A, Stiller C, Härkegård G, Bolland O (2006) Modeling of thermal stresses and probability of survival of tubular SOFC. *Journal of Power Sources* 158, pp 287-294
- [29] Clague R, Marquis A, Brandon N (2013) Time independent and time dependent probability of failure of solid oxide fuel cells by stress analysis and Weibull method. *Journal of Power Sources* 221, pp 290-299
- [30] Frandsen H, Ramos T, Faes A, Pihlatie M, Brodersen K (2012) Optimization of the strength of SOFC anode supports. *Journal of the European Ceramic Society* 32, pp 1041-1052
- [31] Bendsøe M. P. and Kikuchi N. Generating optimal topologies in structural design using a homogenization method. *Computer Methods In Applied Mechanics And Engineering*, Vol. 71, pp. 197-224, 1988.
- [32] Sigmund O. Materials with prescribed constitutive parameters: an inverse homogenization problem. *International Journal of Solids and Structures*, Vol. 31 No. 17, pp. 2313-2339, 1994
- [33] Bendsøe M. P. and Sigmund O. *Topology optimization : Theory, Methods, and Applications*. Springer: Berlin, Heidelberg, 2003.
- [34] Yoon GH, Kim YY (2005) The element connectivity parameterization formulation for the topology design optimization of multiphysics system. *Int J Numer Methods Eng* 64, pp 1649-1677
- [35] Bruns TE (2007) Topology optimization of convection-dominated steady-state heat transfer problems. *Int J Heat Mass Transfer* 50, pp 2859-2873
- [36] Iga A, Nishiwaki S, Izui K, Yoshimura M (2009) Topology optimization for thermal conductors considering design-dependent effects, including heat conduction convection. *Int J Heat Mass Transfer* 52, pp 2721-2732
- [37] H. Rodrigues and H. Fernandes, (1995) A material based model for topology optimization of thermoelastic structures, *International Journal for Numerical Methods in Engineering*, 38, pp 1951-1965.
- [38] Li Q, Steven GP and Xie YM (1999) Displacement minimization of thermoelastic structures by evolutionary thickness designs. *Computer Method in Applied Mechanics and Engineering*, 179, pp 361-378.
- [39] Sigmund O and Torquato S (1997) Design of materials with extreme thermal expansion using a three-phase topology optimization method, *Journal of the Mechanics and Physics of Solids*, 45, pp 1037-1067.

- [40] Sigmund O (2001) Design of multiphysics actuators using topology optimization - Part I: One-material structures, *Computer Methods in Applied Mechanics and Engineering*, 190, pp 6577-6604.
- [41] Cho S, Choi J (2005) Efficient topology optimization of thermo-elasticity problems using coupled field adjoint sensitivity analysis method. *Finite Element Anal Des* 41, pp 1481-1495
- [42] Gao T and Zhang W (2010) Topology optimization involving thermo-elastic stress loads, *Structural and Multidisciplinary Optimization*, 42, pp 725-738.
- [43] Pedersen P and Pedersen NL (2010) Strength optimized designs of thermoelastic structures, *Structural and Multidisciplinary Optimization*, 42, pp 681-691.
- [44] Pedersen P and Pedersen NL (2012) Interpolation/penalization applied for strength design of 3D thermoelastic structures, *Structural and Multidisciplinary Optimization*, 45, pp 773-786.
- [45] Nicholas JD, Barnett SA (2009) Finite-element modeling of idealized infiltrated composite solid oxide fuel cell cathodes. *J Electrochem Soc* 156(4), pp 458–464
- [46] Glowinski R, Pan TW, Wells RO, Zhou XD (1996) Wavelet finite element solutions for the Neumann problem using fictitious domains. *J Comput Phys* 126(1), pp 40–51
- [47] Wells RO, Zhou XD (1992) Wavelet solutions for the Dirichlet problem. Technical report 92 02, Rice University, Computational Mathematics Lab, vol 126 no 1, pp 40–51
- [48] Sigmund O, Petersson J (1998) Numerical instabilities in topology optimization: a survey on procedures dealing with checkboards, mesh dependencies local minima. *Struct Optim* 16, pp 68–75
- [49] Guest JK (2009) Topology optimization with multiple phase projection. *Comput Methods Appl Mech Eng* 199, pp123–125
- [50] Svanberg K (1987) The method of moving asymptotes—a new method for structural optimization. *Int J Numer Methods Eng* 24(2), pp 359–373
- [51] Yakabe H, Ogiwara T, Hishinuma M, Yasuda I (2001) 3-D model calculation for planar SOFC. *Journal of Power Sources* 102, pp144-154
- [52] Wilson JR, Kobsiriphat W, Mendoza R, Chen H, Hiller JM, Miller DJ, Thornton K, Voorhees PW, Adler SB, Barnett SA (2006) Three-dimensional reconstruction of a solid-oxide fuel-cell anode, *Nature Materials*, 5, pp 541-544.
- [53] Wilson JR, Duong AT, Gameiro M, Chen H, Thornton K, Mumm DR, Barnett SA (2009) Quantitative three-dimensional microstructure of a solid oxide fuel cell cathode, *Electrochemistry Communications*, 11, pp 1052-1056.

- [54] Nicholas JD (2013) Personal notes, Michigan State University
- [55] Nicholas JD, Wang L, Call AV and Barnett SA (2012) Use of the Simple Infiltrated Microstructure Polarization Loss Estimation (SIMPLE) model to describe the performance of nano-composite solid oxide fuel cell cathodes, *Phys. Chem. Chem. Phys.*, 14(44) pp 15379.
- [56] Xiong H, Lai BK, Johnson AC and Ramanathan S (2009) Low temperature electrochemical characterization of dense ultra-thin $\text{La}_{0.6}\text{Sr}_{0.4}\text{Co}_{0.8}\text{Fe}_{0.2}\text{O}_3$ cathodes synthesized by RF-sputtering on nano-porous alumina supported yttria-doped zirconia membranes, *Journal of Power Sources*, 193, pp 589
- [57] Lowrie FL, Rawling RD, (2000) Room and high temperature failure mechanisms in solid oxide fuel cell electrolyte, *J. Eur. Soc* (20), pp 751-760
- [58] Radovic M, Lara-Curzio E, (2004) Mechanical properties of tape cast nickel-based anode materials for solid oxide fuel cell before and after reduction in hydrogen, *Acta Mater.* 52, pp 5747-5756
- [59] Borrvall T, Peterson J (2003) Topology optimization of fluids in Stokes flow. *Int. J Numerical methods in Fluids* 41(1), pp 77-108
- [60] Andreassi L, Rubeo G, Ubertini S, Lunghi P, Bove R (2007) Experimental and numerical analysis of a radial flow solid oxide fuel cell. *International Journal of Hydrogen Energy* 32, pp 4559-4574
- [61] Chaisantikulwat A, Diaz-Goano C, Meadows E (2008) Dynamic modeling and control of planar anode-supported solid oxide fuel cell. *Computers and Chemical Engineering* 32, pp 2365-2381
- [62] Yakabe H, Ogiwara T, Hishinuma M, Yasuda I (2001) 3-D model calculation for planar SOFC. *Journal of Power Sources* 102, pp 144-154
- [63] Akhtar N, Decent S, Loghin D, Kendall K (2009) A three-dimensional numerical model of a single-chamber solid oxide fuel cell. *International Journal of Hydrogen Energy*, 34, pp 8645-8663
- [64] Costamagna P, Honegger K (1998) Modeling of Solid Oxide Heat Exchanger integrated stacks and simulation at high fuel utilization. *J. Electrochem. Soc.* 145(11), pp 3995-4007
- [65] Andreasen C, Gersborg A, Sigmund O (2009) Topology optimization of microfluidic mixers. *Int. J. Numer. Mesh. Fluids* 61, pp 498-513
- [66] Pedersen NL (2002) Topology optimization of laminated plates with prestress. *Comput Struct* 80(7-8), pp 559-570

- [67] Radovic M, Lara-Curzio E, Armstrong B and Walls C (2004) Elastic Properties, Biaxial Strength and Fracture Toughness of Nickel-Based Anode Materials for Solid Oxide Fuel Cells. *Developments in Solid Oxide Fuel Cells and Lithium Iron Batteries. Proceedings of the 106th Annual Meeting of The American Ceramic Society, Indianapolis, Indiana, USA, Ceramic Transactions. Volume 161. Ceramic Transactions Series*
- [68] Tezduyar TE, Mittal S, Ray SE, Shih R (1992) Incompressible flow computations with stabilized bilinear and linear equal-order-interpolation velocity-pressure elements, *Comp. Meth. Appl. Mech. Engng.* 95, pp 221-242
- [69] Brooks AN, Hughes TJR (1982) Streamline upwind/Petrov-Galerkin formulations for convection dominated flows with particular emphasis on the incompressible Navier-Stokes equations. *Comp. Meth. Appl. Mech. Engng.* 32(1-3), pp199-259
- [70] Scott JA, (2006) A frontal solver for the 21st Century, *Communications in Numerical Methods in Engineering*, 22, pp 1015-1029